# LUBRICANT FLOW VARIATION IN A TILTING PAD JOURNAL BEARING: QUANTIFICATION OF THE EFFECT ON OPERATION INCLUDING EXAMINATION OF THE RESPONSE AT EXTREME LOW FLOWS

A Thesis

by

**Jonathan J. Toner**

Submitted to the Office of Graduate and Professional Studies of
Texas A&M University
in partial fulfilment of the requirements for the degree of

MASTER OF SCIENCE

| | |
|---|---|
| Chair of Committee: | Luis San Andrés |
| Committee Members: | Adolfo Delgado |
| | Stefan Hurlebaus |
| Head of Department: | Andreas A. Polycarpou |

May 2021

Major Subject: Mechanical Engineering

# ABSTRACT

This work examines the change in performance of a tilt pad journal bearing due to variation in lubricant flow ranging from 150% to 25% (and below) of a theoretical value. The test bearing is a four-pad, 101.6mm (4 inch) diameter, center pivot TPJB, with a single orifice feed arranged in a flooded bearing housing. The results quantify the effects on pad metal temperatures, power loss, eccentricity, and the magnitude of the estimated dynamic coefficients (stiffness, damping and virtual mass) resulting from the variation in flow rate. The tests include two rotor surface speeds, 32 m/s and 64 m/s (105 and 210 ft/s), and three specific loads of 345 kPa to 2068 kPa (50 to 300 psi).

Experimentally measured bearing eccentricity decreases commensurate with an increase in shaft surface speed and increases with an increase in applied load (as expected). Eccentricity generally increases, modestly, with reducing flow. For flows reducing below 50% of the nominal flow, eccentricity increases 2 to 11 μm for operation at 6 krpm and 11 to 15 μm.

Pad metal temperature rise over the inlet oil temperature ($T_{in}$=60°C) for the loaded pads increases for both increasing applied load and shaft speed. Pad metal temperature rise also increases nearly proportionally to decreases in flowrate for operation with flows between 150% and 50% of the nominal flowrate. However, for operation below 50% of the nominal flow, pad metal temperatures increase dramatically with further reducing flowrate, exceeding 64°C and 61°C for operation at 6 krpm and 12 krpm respectively. Thermocouples placed in the bearing housing oil supply annulus indicate that an asymmetrical temperature distribution develops within the annulus. The emergence of the uneven temperature distribution correlates with the dramatic increase in pad metal temperature rise.

Power loss decreases between 12% and 19% for a 50% reduction in nominal flowrate for operation at 6 krpm and applied specific loads between 345 kPa and 2068 kPa. Power savings of between 13% and 19% are realized for the same 50% reduction in flowrate from the 100% nominal flow for operation at 12 krpm. Power consumption for operation at 12 krpm is 3-4X the power consumption at 6 krpm. Power consumption increases roughly proportionally to load at all flowrates and for both operating shaft speeds.

Broadband subsynchronous vibration emerges at very low flows and, most prevalently, at lightly loaded operating conditions. The amplitude of the vibration, when it did emerge, is low relative to the synchronous vibration amplitude and in no cases resulted in unstable bearing vibration.

The direct stiffnesses increase in magnitude with increasing applied load for operation at both shaft speeds. However, the direct stiffnesses are mostly invariant with respect to increasing shaft surface speed. The direct stiffnesses demonstrate orthotropy with $K_{yy} > K_{xx}$ by up to 12% for operation at 6 krpm and up to 30% for operation at 12 krpm. Stiffness increases only modestly for operation with flowrates less than 25% of the nominal.

Direct damping decreases continuously, from 14% to 28%, with decreasing flowrate for operation at 6 krpm. The damping remains nearly constant between 150% and 50% of the nominal flow for operation at 12 krpm, then demonstrates a dramatic decline between 16% and 30% for flows below 50% of the nominal value. Damping for operation at 6 krpm exceeds that for operation at 12 krpm by up to 70% depending on applied load and flowrate.

The results are compared to model predictions for a direct lubricated, evacuated setup. The predictions for eccentricity, stiffness, and damping compare well with the experimental results for high flowrates (~50% to 100% and above of the nominal flow) with discrepancies between measured and predicted values increasing for reducing flowrate. The model generally underpredicts maximum pad temperature for flowrates greater than 100% of the nominal flow as well as bearing power consumption for all flowrates. The underprediction of pad temperature and power loss (as well as the differences in stiffness, damping, and eccentricity at low flows) likely stem from the difference in performance of an evacuated setup bearing compared to the experimental flooded arrangement over the range of flowrates observed.

Generally, the experimental results demonstrate the bearing's ability to tolerate significant reductions in lubricant flowrate (50% or more) without suffering a catastrophic reduction of stiffness or damping and/or suffering from mechanical damage related to exceedance of allowable pad metal temperature limits. The comparison to the model results highlights the operating resiliency of this flooded bearing at exceedingly low flowrates, likely resulting from the retention of oil within the cavity afforded by the flooded arrangement end seals.

# ACKNOWLEDGMENTS

I would like to acknowledge and thank Dr. Luis San Andrés for extending the opportunity to work and learn at the Texas A&M University Turbomachinery Laboratory. I have benefitted greatly from his vast expertise in the field and his guidance during my time in the program. Thanks to the Texas A&M Turbomachinery Consortium for the funding necessary to carry out this work.

Thank you to Dr. Adolfo Delgado and Dr. Stephan Hurlebaus for serving as committee members.

Thank you to Dr. Bonjin Koo for the extensive consultation regarding the bearing performance modeling effort included within this work.

Thank you to Dr. Hunter Cloud, Dr. Minhui He, Dr. John Kocur, and James Byrne for your invaluable advice and encouragement regarding pursuit of the degree culminating in this thesis.

Thank you to my colleagues at the Turbo Lab: Hardik Jani, Hussain Kaizar, Dr. Tingcheng Wu, Dr. Xueliang Lu, Zheng Bian, Bryan Rodríguez, Rachel Bolen, Wonbae Jung, Dr. Rasool Koosha, Jonathan Thiele, Dr. Jing Yang, Scott Tran, Dr. Bonjin Koo, Jose Barajas, Andy Alacantar, and Carl Johnson. I have greatly valued the opportunity to work with and learn from each of you as well as for your camaraderie during our time together at Texas A&M University.

Last but not least, thank you to my children Riley, Reid, and Raegan for your patience, sacrifice and love while dad pursued his degree and completed this thesis. Most of all thanks to my amazing wife, Janine. Without your unconditional love and support this work simply would not have been possible.

# CONTRIBUTORS AND FUNDING SOURCES


## Contributors

This work was supported by a thesis committee consisting of Professor Luis San Andrés [chair], Professor Adolfo Delgado of the Department of Mechanical Engineering, and Professor Stefan Hurlebaus of the Departement of Civil Engineering.

## Funding Sources

This work was supported by funding from the Texas A&M Turbomachinery Consortium.

# TABLE OF CONTENTS

Page

# LIST OF FIGURES

Page

# LIST OF TABLES

Page

# NOMENCLATURE

| | |
|---|---|
| $A_i$ | Bearing acceleration, frequency domain, *i*-direction [m/s$^2$] |
| $C_{ij} = C_{xx}$, $C_{yy}$ | Direct damping coefficients [N·s/m] |
| $C_{ij} = C_{xy}$, $C_{yx}$ | Cross-coupled damping coefficients [N·s/m] |
| $C_{gr}$ | Groove mixing parameter |
| $C_p$ | (Lubricant) specific heat [J/kg·C] |
| $C_{pad}$ | Pad clearance [m] |
| $C_r$ | Bearing radial clearance [m] |
| $D$ | Bearing diameter [m] |
| $e$ | Bearing eccentricity [m] |
| $F_{dx}$ | Dynamic force, *X*-axis [N] |
| $F_{dy}$ | Dynamic force, *Y*-axis [N] |
| $F_s$ | Static force [N] |
| $f_x$ | Measured excitation force, *X*-axis [N] |
| $f_y$ | Measured excitation force, *Y*-axis [N] |
| $H_{ij}$ | Complex dynamic stiffness in the $i^{th}$ direction due to excitation along the $j^{th}$ direction, *i, j*, = *X, Y.* [N/m] |
| $K_{ij} = K_{xx}$, $K_{yy}$ | Bearing direct stiffness coefficients [N/m] |
| $K_{ij} = K_{xy}$, $K_{yx}$ | Bearing cross-coupled stiffness coefficients [N/m] |
| $L$ | Bearing pad axial length [m] |
| $M$ | Virtual mass coefficient [kg] |
| $\dot{m}$ | Lubricant mass flowrate [kg/s] |
| $N_p$ | Number of pads |
| $OD$ | Outside diameter [m] |
| $P_{measured}$ | Measured bearing drag power [W] |

| | |
|---|---|
| $P_{est,thermal}$ | Bearing drag power estimated from oil inlet and outlet temperatures [W] |
| $Q$ | Lubricant volumetric flowrate [LPM] |
| $r$ | Mean pad preload |
| $R$ | Radius [m] |
| $R$ | Pearson product-moment correlation coefficient |
| $R^2$ | Coefficient of determination |
| $S$ | Shaft surface speed = to RΩ [m/s] |
| $S_{err}$ | Standard deviation of the residuals |
| $T_{net}$ | Net bearing drive torque [N·m] |
| $W$ | Applied load [N] |
| $\delta$ | Uncertainty |
| $\Delta x$ | Bearing dynamic displacement, *X*-axis [m] |
| $\Delta y$ | Bearing dynamic displacement, *Y*-axis [m] |
| $\kappa$ | Coefficient specifying the fraction of mechanical energy carried by the lubricant |
| $\lambda$ | Hot oil carry over factor, describing the volume fraction of lubricant flow transferred between upstream and downstream bearing pads |
| $\rho$ | (Lubricant) density [kg/m$^3$] |
| $\Omega$ | Shaft rotational speed [rad/s] |
| $\omega$ | Excitation frequency [rad/s or Hz] |

**Abbreviations**

| | |
|---|---|
| DFT | Discrete Fourier transform |
| LBP | Load between pad |
| LEG | Leading edge groove |
| LOP | Load on pad |
| LPM | Liters per minute |
| SSV | Subsynchronous shaft vibration |
| TPJB | Tilting pad journal bearing |

# INTRODUCTION[1]

Tilting pad journal bearings (TPJBs) find wide application in high performance turbomachinery. Machine designers rely on these mechanical components for rotor position control and static load support as well as for their favorable contribution to rotor-bearing system dynamics, as detailed in Refs. Lund (1964) [1], Lund and Orcutt (1967) [2], Nicholas, Gunter, and Barret (1978) [3], and Nicholas (1994) [4] among many others. However, as with any other critical machine component, there is an industry desire to push the performance limit of TPJBs to achieve higher machine efficiency while maintaining adequate reliability.

Through the development of a hydrodynamic film, TPJBs produce stiffness and damping force coefficients necessary for the support and stable operation of a rotor-bearing system. However, tilting pad journal bearings also produce parasitic drag power losses resulting from lubricant shear. The sheared lubricant generates heat and, when enough of this heat is not removed, can raise pad temperatures above an allowable material operating limit. Many lubricated bearings pad surfaces are covered with a Babbitt layer. Exceeding the pad surface temperature limit (~130°C) manifests as plastic deformation or (at higher temperatures) complete melting of the Babbitt layer and failure of the bearing as per Nicholas (1994) [4], Whalen, et al. (2012) [5], McCloskey (1995) [6].

Past research investigating TPJBs often studied their behavior while operating with a constant lubricant flowrate. A relatively smaller subset of research addresses the change in TPJB forced response due to a varying flowrate. This is understandable since lubricant flow in an operating machine is usually constant, commonly controlled by a metering orifice arrangement in a system with a constant supply pressure control. However, TPJB required lubricant supply flowrate is rotor surface speed dependent. A constant flow rate for a variable speed machine can result in either over-flooding of the bearing at low shaft speed or pad oil starvation at high shaft speed. Over flooding at low speeds manifests as wasted lubricant and can, as the test data in Dixon and Simmons (1994) [7], DeCamillo and Brockwell (2001) [8], and Dmochowski Blair (2006) [9] show, produce parasitic power loss over that associated with the minimum flow required to

[1]Parts of this section reprinted/adapted with permission from Ref [27]

sufficiently cool the pads. Conversely, an under supply of lubricant at a given rotor surface speed can result in pad oil starvation, changes in the dynamic stiffness and damping force coefficients, excessive pad metal temperatures, and/or the emergence of subsynchronous shaft vibration, see Tanaka (2000) [10], DeCamillo, Cloud, He, and Byrne (2008) [11], Nichols (2017) [12], and Kawashita, et al. (2018) [13].

The present work aims to quantify the effect of varying lubricant flowrate on a test TPJB load, pad temperatures, drag power loss, exit oil temperature and dynamic force coefficients vs. load and shaft angular speed. The study compares the experimental results to predictions generated using a TPJB model accounting for the effects of flow starvation as presented in San Andrés, et al. (2017) [14]. The research characterizes a 101 mm diameter ($D$), 0.6 length/diameter ($L/D$), four pad bearing configured with a single orifice oil feed between each pad and set in a flooded housing. The test battery includes operation at two angular shaft speeds = 6000 rpm and 12,000 rpm (32 m/s and 64 m/s shaft surface speed), three specific loads $W/(LD)$) = 345 kPa, 1034 kPa, and 2068 kPa, and for oil flowrates between 25% and 150% of the theoretical design supply flow.

Additionally, the study presents the results of a *low flow limit test* for each operating condition. The *low flow limit* is the lowest flow that the bearing can sustain during operation at each shaft speed/load combination before either (1) a pad temperature limit of 121°C (250°F) is reached, or (2) the bearing demonstrates the emergence of subsynchronous vibration or worse, subsynchronous whirl. Nicholas (1994) [4] notes softening of the Babbitt between 121°C and 135°C and recommends limiting pad temperature during operation to 121°C. This study follows this pad temperature operating limit to minimize the risk of pad surface damage while allowing for a useful range of flowrate variation during testing.

# LITERATURE REVIEW[2]

Past research concerning lubricant flow variation typically seeks to characterize the effect on power loss, pad metal temperatures, and the related effect on the dynamic force coefficients associated with the change in flowrate. Additionally, as film starvation has been associated with the emergence of subsynchronous vibration (SSV), past research efforts involving low flow TPJB operation also focus on the change in vibration response as the supplied flowrate is drastically reduced.

### *TPJB Flowrate Variation—Static and Dynamic Parameters*

Heshmat and Pinkus in (1985) [15] study the effect of film starvation on the operating eccentricity and attitude angle, minimum film thickness, film length, bearing surface temperature, and power loss on a 138 mm, 0.92 (L/D), plain journal bearing arranged without end seals. The experimental setup includes pressure transducers arranged along the bearing circumference capable of measuring the extents of the hydrodynamic film pressure allowing empirical definition of the film length. Additionally, a transparent bearing shell allows the researchers to observe the behavior of the film as flow rate is varied. Through these measurements and observations, the researchers directly correlate the change in length of the film along the bearing arc to the change in supplied flow, showing a retreat of the film as the flow is reduced. As the flow reduces, an eccentricity increase coupled with a decrease in attitude angle manifests as the film reduces in length and becomes more highly stressed. Power loss decreases by as much as 80% for an 88% reduction in flow from the fully flooded condition. However, bearing surface temperature reach 106°C for the same minimum flow conditions when operating at the highest rotor speed observed.

In 1994, Simmons and Dixon [7] evaluate the effect of a change in oil flowrate as well as bearing clearance, pad preload, and the orientation of the applied load on the performance of a 200 mm diameter, 0.4 *L/D*, rocker back tilt pad journal bearing arranged with flooded end seals. The study evaluates performance for rotor surface speeds of 31 m/s to 105 m/s and specific loads *W/(LD)* between 0 and 4.14 MPa. The authors determine the required oil flowrate by gradually

[2] Parts of this section reprinted/adapted with permission from Ref [27]

reducing flow for a particular load and shaft speed combination until the temperature rise between the oil supply and the oil drain reaches 17°C. This temperature rise corresponds to an oil drain temperature of 60°C. Generally, the authors find that the flowrate required to operate with this supply/drain temperature difference varies greatly with speed but has little dependency on the bearing load orientation, preload, or clearance. Maximum pad temperatures increase strongly with increasing rotor surface speed, but only show a weak dependence on specific load. Similarly, power loss has little dependency on increasing specific load but does increase dramatically with surface speed from 3 kW at 31 m/s to 81 kW at 105 m/s. The authors use the mass flow and temperature rise of the lubricant as it passes through the bearing to determine power loss.

Ref. [7] also reports the effect specifically resulting from flowrate variation by comparing the observed (baseline) bearing response while operating with a 60°C drain temperature to that observed when the supply flowrate is further reduced until the drain temperature increases to 75°C. For 52 m/s and 105 m/s rotor surface speeds, the flowrate required to maintain a 75°C drain temperature is 50% less than that for a 60°C drain. The power loss reduces by 20% for this same 50% flowrate reduction, showing that under these test conditions, the parasitic losses in the bearing can be reduced by reducing the supply flowrate.

In 2001, DeCamillo and Brockwell [8] present the results of a study on the effect of oil flowrate variation on a 152 mm diameter, 5-pad, TPJB with both close clearance and high clearance end seals and arranged in both a center pivot and offset pivot configuration. The authors find that for a shaft operation below 6000 rpm, a 50% drop in oil flowrate has negligible effect on the pad metal temperature. However, for both pivot configurations, the bearings demonstrate higher pad metal temperatures when operating with reduced flowrate for rotor speeds exceeding 6000 rpm. This indicates that at least for the higher rotor speed test conditions (i.e. > 6000 rpm), reducing the oil flowrate can have an adverse effect on the pad metal temperature. The authors also note a 10-20% decrease in power loss for the same 50% reduction in oil flowrate for the offset pivot bearing when operating with a rotor speed above 6000 rpm.

He, et al. (2005) [16] present a thermohydrodynamic computational model predicting the response of a tilting pad journal bearing with leading edge groove lubrication (LEG) to flow rate variation. The model iteratively solves for the film length developed on each pad through an algorithm considering total supply flow, pad geometry, lubricant properties, thermal properties of

the pad and oil, rotor surface speed, and applied load. The model predicts film starvation that progresses first across the unloaded top pads (for a downward loaded condition), then to the side pads, culminating with starvation of the loaded pads as the flowrate descends from a fully flooded condition to a severely starved condition.

The authors in Ref. [16] compare model predictions to published data for a five-pad, 98 mm diameter, 0.387 L/D, 60% offset tilting pad journal bearing arranged with LEG lubrication in an evacuated housing. Generally, the predictions for power loss and pad metal temperatures agree well with the published results, especially for the flooded condition. As the flow rate decreases from the fully flooded condition, the discrepancies between the model predictions and the published test data tend to increase. The authors point out that the complex cavitated and turbulent flows in the starved films can introduce significant uncertainties in determining the resulting film heat dissipation and pressure development, and in turn affect the fidelity of the prediction. Similarly, the basic model assumptions ignoring elastic deformation of the pads and considering the developed films to be isoviscous across the entire pad arc also possibly reduce the accuracy of the prediction. However, regardless of the accuracy of the magnitude of the predictions, the published trends for pad temperature and power loss vs. flow rate are in good agreement with the predicted trends.

The work in He, et al. (2005) [16] also adds value by clearly illustrating how the increased lubricant demands required to sustain a full-length film result in film starvation progressing first in the unloaded pads and then to the loaded pads as the supplied flow reduces from a fully flooded condition. The larger oil demand of an unloaded pad stems from its larger relative clearance between the pad surface and the rotor surface as compared to a loaded pad. Accounting for the progression of film length reduction (i.e. starvation) allows the algorithm to predict for the change in performance parameters such as pad temperature, eccentricity, film stiffness, etc. of the bearing relative as the supplied flow changes. Figure 1, adapted from He, et al. (2005) [16], depicts the starved vs. fully developed films in the subject five-pad bearing as flow rate decreases from 100% to 30% of the fully flooded condition.

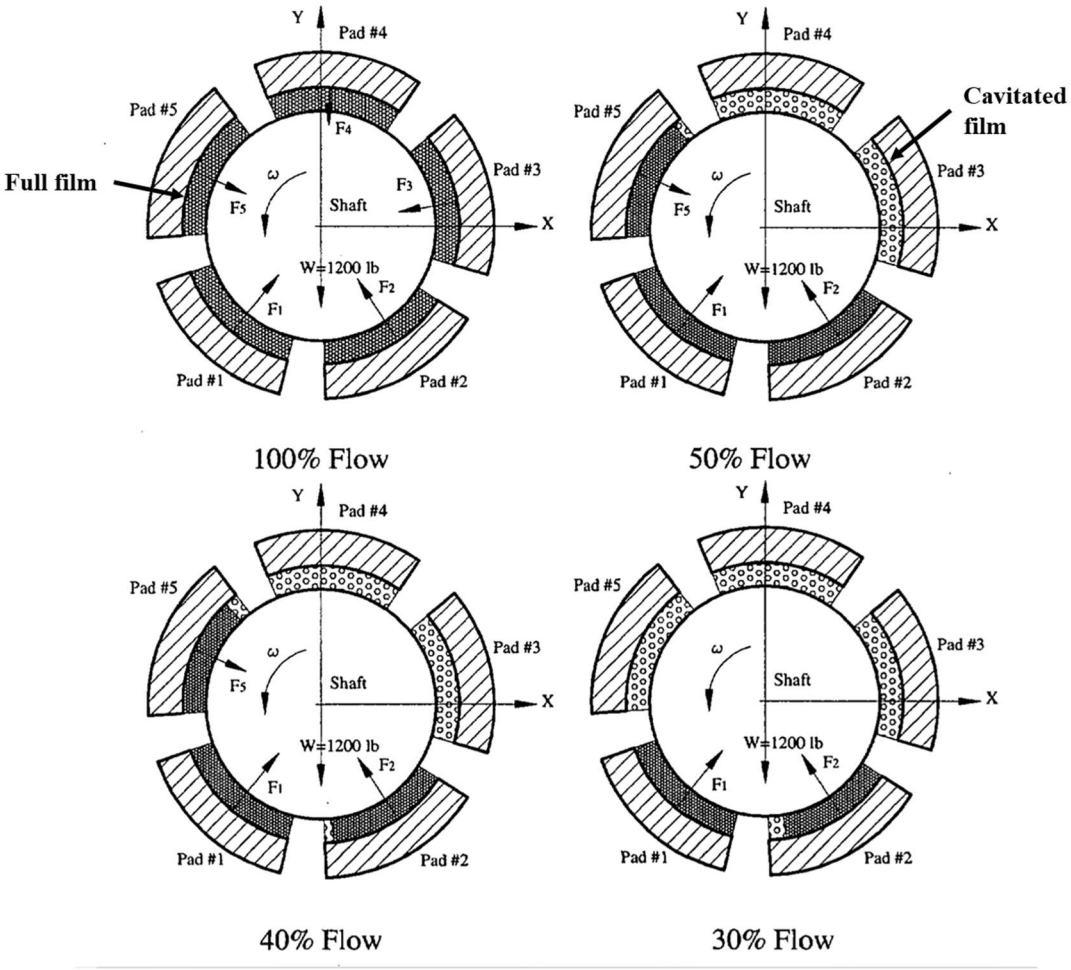


**Figure 1: Film starvation progression for a five-pad TPJB with leading edge groove supply (LEG) as the flow decreases from 100% to 30% of a fully flooded condition when operating with 5338 N applied load and at 16,500 rpm. Adapted from He, et al. (2005) [16].**

In 2006, Dmochowski and Blair [9] evaluate the effect of reducing the oil flowrate for a 98.6 mm, 5-pad, load between pad (LBP) TPJB in both flooded and evacuated configurations for operation with rotor surface speeds between 15 m/s and 76 m/s. The authors find that reducing the flow up to 37% less than the nominal had a minimal effect on pad metal temperatures. The flow reduction did, however, result in a modest power savings that increased as the rotor surface speed increased, reaching a maximum of 12% at 76 m/s. Figure 2 shows the estimated power loss as a function of rotor speed for both flooded and evacuated bearing configurations.

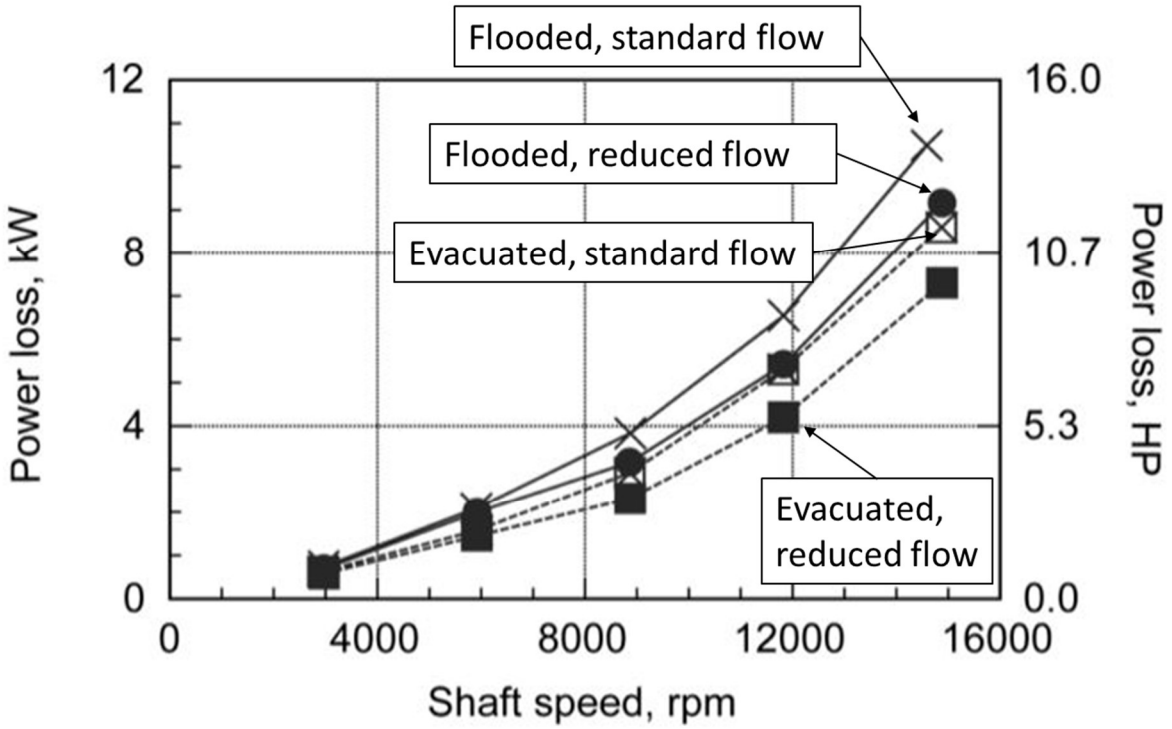


**Figure 2: Power loss estimated from exit oil temperature rise and lubricant mass flow rate vs. shaft speed with an applied load of 6.05 kN for both flooded ends and evacuated ends bearing configurations and for both a standard flow (100% nominal) and a reduced flow (63% to 71% of the nominal flow). Adapted from Dmochowski and Blair (2006) [9].**

The authors state that the reduction in power loss at reduced flow is likely due to a reduction in churning losses within the bearing cavity, citing the mechanism described in an earlier analysis by Booser and Messina (1990) [17]. Direct stiffness and damping force coefficients change little with the flowrate reduction for the flooded configuration. However, the authors report a 30% decrease in stiffness and damping coefficients in the direction orthogonal to the applied static load for the same flowrate reduction in the evacuated bearing. This reduction in the magnitude of the dynamic force coefficients suggests that the reduced flowrate is affecting the film development and performance orthogonal to the load, at least in the evacuated configuration.

In 2017 Nichols [12] quantifies the effects of lubricant flowrate variation on the performance of a 70 mm diameter 5-pad TPJB in a flooded arrangement. Nichols finds a modest increase of 3°C to 4°C when comparing pad metal temperature for operation with a maximum supplied flow of 4.54 LPM to operation with a reduced flow of 3.03 LPM for rotor speeds exceeding 6000 rpm.

Pad metal temperature difference is 1°C or less for operation at rotor speeds below 6000 rpm. The same flowrate reduction resulted in as much as a 20% decrease in power consumption for rotor speeds exceeding 6000 rpm, echoing the trends of previous experimental studies such as Dixon and Simmons (1994) [7], DeCamillo and Brockwell (2001) [8], and Dmochowski and Blair (2006) [9]. Additionally, Nichols reports the reduction in the rotordynamic stability of his fixed bearing/floating rotor test rig as the supply flowrate decreases, evidencing first the emergence of SSV, and then the increase in SSV severity as the flowrate is further reduced. Nichols attributes the decay in system stability and change in vibration signature with flow reduction to the onset of film starvation and the associated reduction in direct damping coefficient.

Abdollahi [18] in 2019 presents a thermo-elasto-hydrodynamic (TEHD) model predicting TPJB performance accounting for pivot and pad deformation under varying load and surface speed for a given (known) lubricant flowrate. The model introduces "groove demand" as a method to portion the given (total) supplied lubricant flowrate to each of the pads' feed grooves based on actual operating eccentricity, upstream pad trailing edge flow, and the quantity of oil required to fill the downstream pad leading edge. An empirically derived groove mixing parameter "$C_{gr}$" determines the efficiency with which the hot oil leaving the upstream pad mixes with cold, fresh oil present in the pad feed groove before entering the downstream pad clearance gap. Modification of $C_{gr}$ accounts for the effects of bearing end seal configuration such as improved hot oil removal from evacuated ends or the associated churning of and retention of hot oil within the groove in a flooded arrangement. Abdollahi's model provides the means to understand relative pad oil flow magnitudes based on operating condition and physical bearing arrangement for the purpose of improving the predicted and circumferentially asymmetric leading-edge lubricant conditions present in an operating TPJB.

San Andrés, et al. [19] in 2020 investigate the effect of flowrate variations, ±50% from a nominal value, on a 101 mm diameter 5-pad TPJB arranged with load between pads and in a flooded housing. The test conditions include rotor surface speeds of 32 to 85 m/s and specific loads of 0.17 to 2.1 MPa, respectively. The selected bearing supplied 'nominal' flowrates depend on rotor surface speed and are therefore not constant throughout all of the test conditions. The authors show that at a relatively high surface speed and moderate specific load (74 m/s and 1.0 MPa), a 15% power savings can be realized for a 50% reduction in supplied flowrate with only a

6°C increase in pad metal temperature and with a modest increase in direct stiffness and a decrease in direct damping. A torque meter integral to the test rig's coupling permits direct measurement of the torque (and power) absorbed by the test bearing. The setup eliminates inaccuracies encountered when estimating power loss via supplied lubricant mass flow and temperature difference between supply and discharge condition. Generally, the results at other rotor speeds and applied loads are similar— a modest reduction in power consumption coupled with minor changes in pad metal temperature when the flowrate is reduced for all but the most severe operating conditions. Analogously, the changes in the magnitude of the stiffness and damping coefficients are only modest over the ranges of flowrates observed. These findings are consistent in trend with other research involving flowrate variation, at least for flooded TPJB arrangements such as in Dmochowski and Blair (2006) [9]. This suggests that natural oil retention within the flooded housing wards off the advance of pad film starvation, thus not affecting the magnitude of the dynamic force coefficients and with only relatively minor increases in pad metal temperature.

In 2020, Zemella, et al. [20] present the results of an experimental investigation of a 100 mm dimeter, 90 mm axial length, five-pad, TPJB arranged with flooded end seals, and operating to surface speeds between 25 m/s and 120 m/s, specific loads of 0 MPa to 3.0 MPa and supplied flowrates of 45 LPM to 120 LPM. The work focuses on comparison of the experimentally identified dynamic force coefficients determined utilizing both a K-C-M model or a simplified K-C model as well as comparison of those identified coefficients to predictions delivered by a theoretical TEHL model. However, as part of the experimental and theoretical model evaluation, the authors provide a valuable example of the behavior of a flooded TPJB bearing arrangement to flow rate variation over a wide range of speeds and applied loads. The authors find that the direct stiffnesses vary modestly with flowrate over the range of surface speeds observed. The experimentally identified damping tends to decrease significantly at higher speeds (>60 m/s) but only for the lowest flowrates observed (45 LPM to 65 LPM). The authors assert the decrease in estimated damping when reducing flowrate follows only in operating conditions producing a sufficient level of film starvation. When operating with sufficient lubricant flow, even at high surface speeds, the estimated damping coefficient remains mostly invariant.

***Subsynchronous Shaft Vibration (SSV)***

Subsynchronous vibration associated with low flow TPJB operation is also of interest to the turbomachinery community. SSV, in varying severities, can be responsible for a number of problems: operating vibrations alarms, wear or fretting of pivots and pad surfaces, or a general indication that the system's rotordynamic stability has decayed to an unacceptable level. Research into this facet of low flow operation seeks to quantify and classify the effects of SSV as well as to predict its onset.

Tanaka in 2000 [10] investigates of the effects of lubricant starvation on the performance of a 45 mm diameter plain journal bearing without end seals. The work examines, experimentally and theoretically, the changes in the development of the hydrodynamic film under starved flow conditions for various combinations of rotor speed, applied bearing load, and oil supply flowrate. The test rig setup utilizes a bearing shell constructed from a transparent material permitting the direct observation of the film "coverage" during journal operation. Tanaka finds that an increase in rotor speed or a decrease in flowrate leads to a more starved condition (as expected). The film starvation is evidenced by areas of journal clearance devoid of oil. The denuded journal clearance begins at the oil feed groove and stretches downstream, with the length of the uncovered area(s) increasing as the starved condition becomes more severe. Tanaka provides diagrams of the experimental observations in Figure 3.

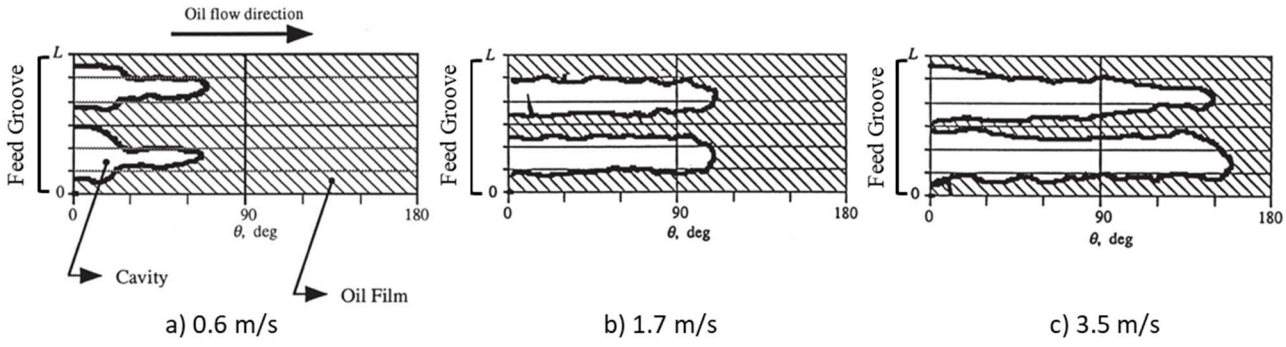


**Figure 3: Graphical representation of film starvation as the area devoid of lubricant grows for a plain journal bearing with load equal to 36 kPa W/(LD), flowrate equal to 30 mL/min, and rotor surface speed equal to a) 0.6 m/s , b) 1.7 m/s, and c) 3.5 m/s. Adapted from Tanaka (2000) [10].**

Tanaka's use of a transparent bearing shell is similar to the earlier work by Heshmat and Pinkus (1985) [15], that also allowed the researchers to visually observe the manifestation of film starvation in a plain journal bearing through a transparent bearing housing. Similarly, Pinkus and Heshmat describe and diagram the appearance of the film development they observed under starved conditions. The researchers note an oil cavitated zone beginning at the oil feed groove and then stretching downstream to a fully developed film zone as well as oil streamlets stretching between the end of the full film zone and the upstream side of the oil feed groove. The researchers note that the streamlet formations periodically "pulse" through the cavitated zone, eventually joining the region of full film. The streamlet pulsing correlates with journal vibration, however not necessarily subsynchronous in vibration signature.

Both of these works study the manifestation of film starvation in plain journal bearings and do not document the emergence of SSV. However, these works are still valuable to understanding the origin of SSV in fluid film bearings in later research efforts in general as they give insight into the manifestation of the physical mechanism of film starvation. They provide a unique visual representation of the progression of film starvation that can be used to interpret, visualize, and rationalize later research efforts, especially the mechanisms that contribute to the emergence of SSV in tilting pad journal bearings.

In 2008, DeCamillo, et al. [11] detail a comprehensive effort to characterize the parameters resulting in the emergence of SSV "hash" in a 127 mm, five-pad TPJB. The authors specify SSV hash as broad band subsynchronous vibration lacking discrete frequency peaks. The test bearing(s), arranged with or without end seals, with center and offset pivots, and in LBP or LOP configurations, permit a parametric study over a wide range of surface speeds, applied radial loads, and oil flowrates. The authors find that the factors conducive to the emergence of SSV hash could not be isolated to a single set of parameters. For example, SSV did not only occur at low load and low shaft speed, could emerge for both evacuated and conventional (flooded) arrangements, and could not always be eliminated by simply increasing the oil flowrate to the test bearing. The battery of tests performed in conjunction with the authors' theoretical investigation suggest that the manifestation of SSV hash is due to the vibration of individual pads occurring under starved or partially starved flow conditions, especially when the bearing cavity is not completely flooded. The mitigation of SSV hash by either completely flooding the cavity or installing pads with a

patented channel that directs pad side leakage to the downstream pad (attenuating starvation) confirms these assertions.

In 2017, San Andrés, Koo, and Hemmi [14] present an analytical model predicting the onset of SSV as a function of the flowrate delivered to a TPJB. The model provides a means to quantify the effect of pad film starvation due to low flow in terms of the change in the magnitude of the full set of dynamic force coefficients. The predicted decay in direct damping and the increase in direct stiffness, both associated with a decrease in the pad's effective film length as starvation increases in severity, match observed behavior for a four-pad LBP and five-pad LOP bearings taken from accounts of actual operating machines. Additionally, the model predicts the emergence of unstable pad rotational modes of the mostly unloaded side pads as the lubricant flowrate reduces and the starvation condition becomes more severe. These results link, analytically, the emergence of the unstable side pad modes to the lateral excitation of the rotor and the onset of SSV as a function of reducing flowrate, thus confirming the findings of empirical efforts measuring the side pad oscillation directly such as in the work presented by DeCamillo, et al. (2008) [11].

In 2018 Kawashita, et al. [13] further quantify the conditions causing the onset of SSV and the related effects of starvation in a TPJB. The experimental effort subjects a two-pad, 200 mm diameter TPJB with direct lubricated pads with and without end seals (i.e. flooded and evacuated) to flowrate variations. Pressure transducers located in the test rig rotor provide a means to directly observe the developed pressure field as the transducers pass the bearing pads while the rotor spins during operation. The rotating transducers allow mapping of the film extents by comparing the pressure measurements to the known angular positions of the leading and trailing edges of the bearing pads. The pressure maps show that as flowrate reduces, the film retreats from the leading edge of the pad as starvation progresses. The length of pad devoid of lubricant increases as a function of flowrate reduction. Coincident to the increase in the starved pad arc length is the decrease in the estimated direct damping and increase in direct stiffness of the test rig rotor-bearing system, culminating in the emergence of SSV at the lowest flowrates. These findings help to experimentally quantify the behavior of the film during starvation and confirm findings such as presented by Tanaka (2000) [10] and DeCamillo, et al. (2008) [11].

# RESEARCH OBJECTIVES/TASKS

The present research effort quantifies the effect of flowrate variations on the load performance of a four-pad flooded TPJB. The investigation encompasses measurements of its static and dynamic load performance over a range of rotor surface speeds, applied specific loads *W/(LD)*, and range of flowrates as listed in Table 1.

The research effort completed the following specific tasks:

- Experimentally measure the response of the test bearing as per power consumption, journal eccentricity, and pad metal temperatures over a range of rotor surface speeds, applied specific loads *W/(LD)*, and oil supply flowrates as defined in Table 1. To avoid damage to the test apparatus, the flowrate reduction and test observation ceases for rotor surface speed and applied load combinations before pad metal temperatures exceed 121°C (250°F) or reach excessive magnitudes of SSV.
- Record the change in vibration response resulting from flowrate variation.
- Estimate the change in stiffness, damping, and virtual mass coefficients for the operating conditions outlined in Table 1. The dynamic force coefficients are estimated utilizing the measured dynamic response (bearing housing displacement and acceleration) to a known dynamic force input (forced excitation) with the analysis performed in the frequency domain as per the technique adapted from Childs and Hale (1994) [21], Rodriguez (2004) [22] and San Andrés (2009) [23].
- Compare the experimentally measured results to predictions delivered by the model described in San Andrés, et al. (2017) [14].
- Draw corollaries and conclusions based on the observed experimental response.

**Table 1: Operating Conditions for Bearing Testing**

| Rotor Angular Speed (Rotor Surface Speed) | Oil Flowrate, Percent Theoretical (volumetric flowrate) | Specific Static Load (LBP) |
|---|---|---|
| 6000 RPM (32 m/s) | 150% (21.6 LPM) | 345 kPa→1034 kpa→2068 kPa ↓ |
| | 100% (14.4 LPM) | |
| | 50% (7.2 LPM) | |
| | 25% (3.6 LPM) | |
| 12,000 RPM (64 m/s) | 150% (43.2 LPM) | 345 kPa→1034 kpa→2068 kPa ↓ |
| | 100% (28.8 LPM) | |
| | 50% (14.4 LPM) | |
| | 25% (7.2 LPM) | |

Notes:

1) Dynamic excitation response is recorded after every static test point

2) The "hot" bearing clearance is measured after recording the dynamic response for each 2.068 MPa static load operating point.

3) Table gives the "planned" test conditions. Testing will also encompass the lowest flowrates achievable at each surface speed/specific load combination as limited by pad metal temperature or SSV response.

# TEST RIG AND TEST BEARING DESCRIPTION[3]

## *Test Rig*

The test rig is of the floating bearing type, similar to that described in San Andrés, et al. (2020) [19]. This design features a test bearing that moves radially relative to a rigid rotor and in response to changing load conditions. A primary advantage of the floating bearing is the ability to directly load (statically and dynamically) the test bearing and to measure the bearing displacement response relative to the rotor motion. The main test section, shown in Figure 4, consists of a solid rotor rigidly supported on rolling element bearings housed in two rigid rig pedestals. An air turbine drives the test rotor through a coupling equipped with an integral strain gauge type torque meter.

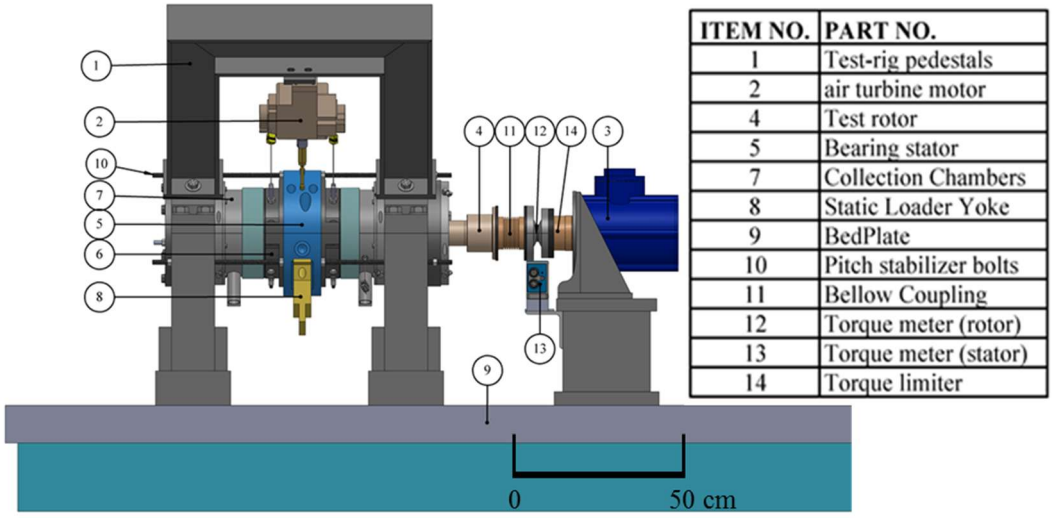


| ITEM NO. | PART NO. |
|---|---|
| 1 | Test-rig pedestals |
| 2 | air turbine motor |
| 4 | Test rotor |
| 5 | Bearing stator |
| 7 | Collection Chambers |
| 8 | Static Loader Yoke |
| 9 | BedPlate |
| 10 | Pitch stabilizer bolts |
| 11 | Bellow Coupling |
| 12 | Torque meter (rotor) |
| 13 | Torque meter (stator) |
| 14 | Torque limiter |

**Figure 4: Side view of test rig for lubricated hydrodynamic fluid film bearings and annular pressure seals. Reprinted/adapted from Ref [27].**

An air cylinder, connected through a yolk, pulley and cable assembly applies a static load to the test bearing stator along the *Y*-axis. A pair of electro-hydraulic shaker heads apply dynamic loads to the test bearing. The shaker heads connect to the test bearing stator through slender rods

[3] Parts of this section reprinted/adapted with permission from Ref [27]

(named stingers) oriented along both the $X$ and $Y$ axes. Figure 5 shows an isometric and front view of the bearing stator with its static ($F_s$) and dynamic ($F_{dy}$ and $F_{dx}$) load connections.

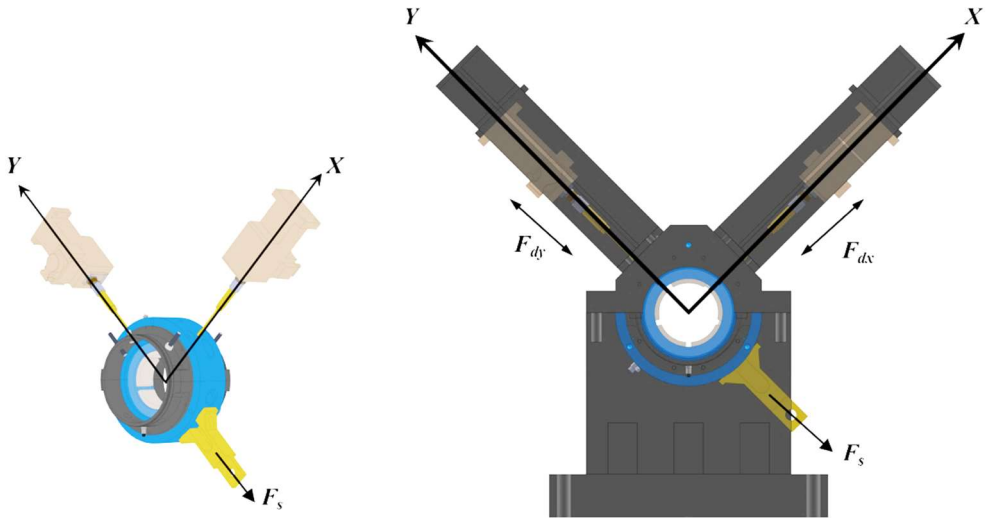


**Figure 5: (Left) Isometric and (right) front views test rig with load arrangement. Reprinted/adapted from Ref [27].**

Two pairs of Eddy current type proximity sensors oriented along the $X$ and $Y$ axes measure the displacement of the test bearing relative to the rotor. A pair of piezo-electric accelerometers attached directly to the outside of the bearing housing record its absolute acceleration along the $X$ and $Y$ axes. Two load cells attached to the tip of each of the two shaker heads measure the applied dynamic loads. A third load cell connected to a pneumatic cylinder records the applied static load. The recorded displacement, acceleration, and force data correspond to specific operating conditions of rotor speed and oil supply conditions.

An external oil system supplies ISO VG46 lubricant to the test bearing through a flexible hose and at a constant supply temperature of 60°C +/- 0.5°C. The lubricant delivery system includes the pumps, filters, heaters, coolers, and control valves needed to provide a clean supply of oil at the required flowrate and temperature condition. Note that a turbine type flow meter measures the lubricant volumetric flowrate supplied into the test bearing.

***Test Bearing:***

The test bearing is a four-pad TPJB, 101 mm nominal diameter, arranged in a load between pad (LBP) configuration in a flooded housing. The bearing is similar in geometry and configuration to the one described by Coghlan [24]. Figure 6 depicts the bearing, with and without

end seals, and the bearing stator. Table 2 lists the pertinent bearing geometry and materials of construction.

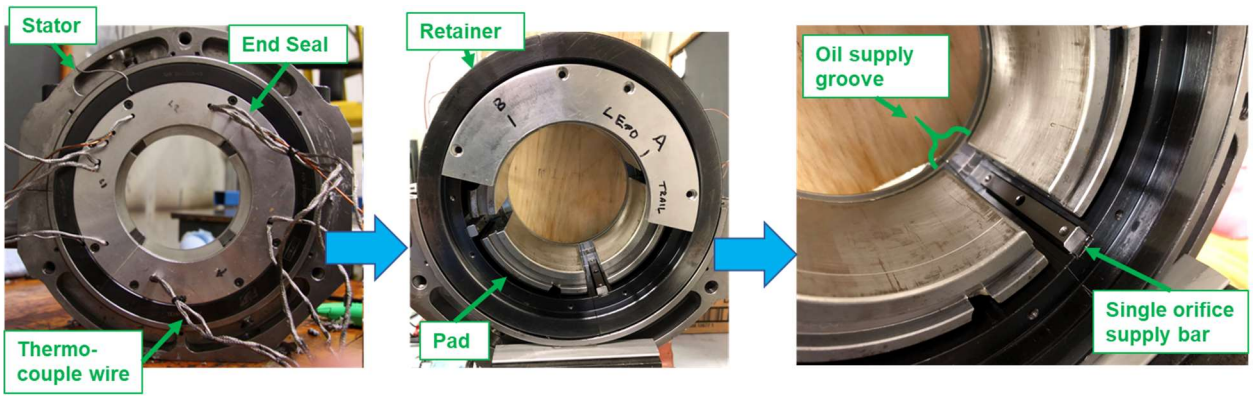


**Figure 6: Photographs showing the assembled bearing in the test stator (left), the bearing with the lower half end seal removed revealing the pads and supply groove (middle), and a close up view of the supply groove with the single orifice supply bar (right). Wires denote thermocouples. Reprinted/adapted from Ref [27].**

**Table 2: Test bearing geometry and materials of construction. Reprinted/adapted from Ref [27].**

| | |
|---|---|
| Diameter, $D$ | 101.77 mm |
| Length, $L$ | 61 mm |
| Number of Pads | 4 |
| Pivot Type | Spherical |
| Pivot Offset | 0.50 |
| Pad Arc Length | 72° |
| Bearing Measured Radial Clearance: Cold @25°C (for "hot" clearances see Table 4) | $C_r$ = 115 µm |
| Dimensional Preload ($r = C_{pad} - C_r$)[1] | $r$ = 0.30 |
| Pad Material | AISI 1018 Steel |
| Pad Surface Material | Babbitt |
| Lubrication Condition | Single orifice between Pads |
| Single Orifice Size | 4.4 mm diameter |
| Housing Type | Flooded with end seals |
| End Seal Radial Clearance | 165 µm |
| Pad Material | AISI 1018 Steel |
| Pad Mass (average)[2] | 0.635 kg |
| Pad Mass Moment of Inertia[2] | $4.59 \times 10^{-4}$ kg·m$^2$ |
| Pad Thickness[2] | 19 mm |
| [1] Taken from bearing manufacturer's specifications<br>[2] Adapted from Coghlan [24] | |

Figure 7 provides a graphical representation of the thermocouple locations as well as a photograph of the outside diameter of the bearing shell showing the disposition of thermocouples in the central annulus distributing oil into each pad through feed holes. Each loaded pad contains thermocouples embedded 7 mm below the Babbitt surface at the leading edge, trailing edge, and

at the 75% pad arc position of the pad for measurement of pad metal temperature. The two unloaded pads have embedded thermocouples at the 75% pad arc position only. Thermocouples located in the oil supply groove immediately ahead and behind of each loaded pad at the approximate position of the pad surface measured the entering and exiting oil film temperature. Four thermocouples, one for each supply groove, are located in the oil supply annulus in the bearing stator. These thermocouples measure the oil temperature immediately before it passes through the supply orifice and flows into the bearing. Figure 8 shows an alternate schematic view of the thermocouple layout, presenting the pad surfaces and thermocouple orientation as though the bearing had been "unwrapped" from the rotor surface.

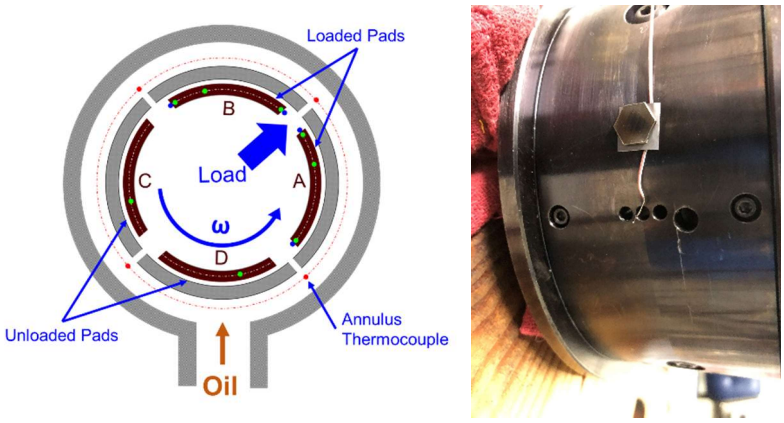


**Figure 7: (Left) Graphical representation of the bearing pads and locations of thermocouples in the central annulus; and (right) photograph displaying the location of a thermocouple wire and junctions on the outside of the oil supply annulus. Reprinted/adapted from Ref [27].**

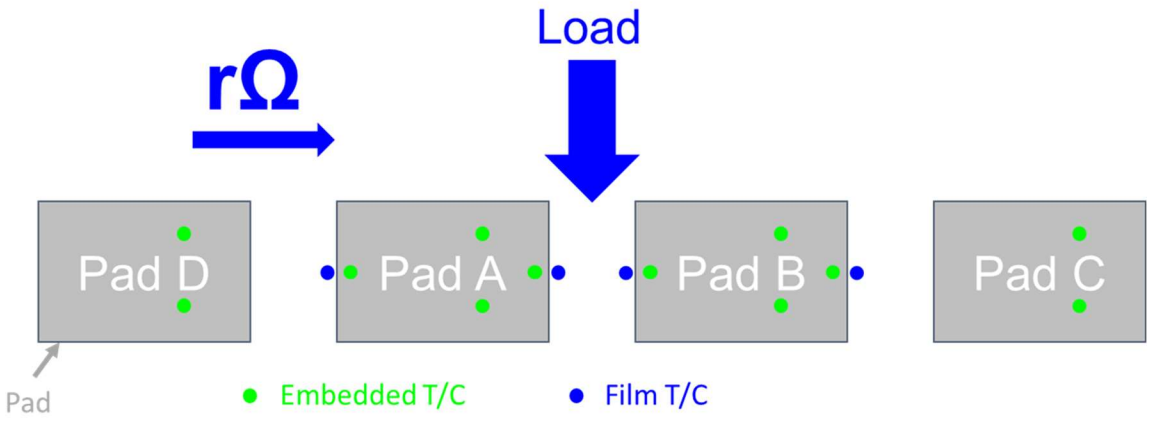


**Figure 8: Unwrapped view of thermocouple location, embedded in pads and facing oil film; referenced to load direction (Y axis) and direction of shaft speed rotation (Ω). Reprinted/adapted from Ref [27].**

A PC hosted system provides the interface for control of the test rig during operation. An elaborate data acquisition system records all parameters characterizing the bearing static and dynamic response to the imposed test condition. The system is not described in any further detail here.

# EXPERIMENTAL PROCEDURE[4]

The goal of the experimental work is the quantification of the response of a tilt pad journal bearing to variation in the lubricant flow rate. To this end, the experimental procedure measures the bearings static and dynamic response for lubricant flowrate ranging from 150% of a nominal condition to 25% (or less) while operating the bearing over a range of rotor speeds and under increasing static loads. Table 1 (presented earlier) details the test conditions as specified by controlled changes in rotor speed, static load, and lubricant flowrate.

At a particular test condition, modulation of the air flow into the drive turbine sets the rotor speed, the air pressure into the static load cylinder sets the static load, and the oil supply control valve position sets the oil flowrate. For each operating condition and before recording any test data, the pad metal temperatures must first become steady (in time) thus signifying the rig reached thermal equilibrium. The measured static data including pad metal temperatures, bearing eccentricity relative to the shaft, drag torque, and annulus oil supply temperature define the static response of the bearing.

Immediately after measuring the static load response and while still operating at a thermally steady condition, the hydraulic shakers apply dynamic loads to the bearing. The recorded dynamic data includes bearing housing displacements relative to the spinning rotor, bearing housing accelerations, and the input excitation dynamic forces.

### *Nominal Oil Flowrate*

The flow rate, $Q$, to fully lubricate the bearing is: (adapted from San Andrés (2020) [19])

$$Q = \frac{1}{2} N_p \, S \, L \, C_r \, (1 - \lambda) \qquad (1)$$

Where: $N_p$ = number of pads, $S = \Omega R$ or surface speed (m/s), $L$ = bearing axial length (m), $C_r$ = bearing radial clearance (m), and $\lambda$ = hot oil carry over factor (empirical, ranging from 0 to 1).

[4] Parts of this section reprinted/adapted with permission from Ref [27]

Figure 9 displays the calculated flow rate vs. rotor surface speed and noted as 100% (nominal). The figure includes other lines representing changes in flow, above and below the nominal condition.

Note that some fluid recirculates within the bearing, traveling from the trailing edge of an upstream pad onto the leading edge of a downstream pad. This recirculation (i.e. carry over) allows the total supply flow delivered to the bearing to be less than the sum of flows crossing the leading edges of all of the pads, filling the average leading-edge gap between the rotor and pad surfaces. The average gap between the shaft surface and pad surface is the radial bearing clearance, $C_r$. The initial (cold) clearance, $C_r$ = 115 μm ± 4.3 μm, is found per the procedure described later in this section.

To account for the recirculation in the bearing, Eqn. (1) includes a hot oil carry over factor "$\lambda$", representing the fraction of the "hot oil" flow exiting the trailing edge of an upstream pad that ultimately enters the leading edge of the downstream pad instead of immediately exiting the side of the bearing toward the sump. $\lambda$ ranges from 0 to 1, with a low value (<<1) indicating a small fraction of hot oil carried to the leading edge of the downstream pad, and vice versa.

Past research efforts accounting for recirculation within the bearing using a hot oil carry over factor typically find the proper value by adjusting $\lambda$until good agreement is achieved between predicted and experimentally determined pad temperatures for a given (known) total supply flowrate. The literature typically reports $\lambda$ between 0.4 and 1 dependent on factors such as shaft surface speed, lubrication method (flooded housing, evacuated housing, directed lube, conventional, etc.) and other factors; see for example, references Nichols (2017) [12], He, et al. (2005) [16], and Mitsui, et al. (1983) [25].

The present experiment utilizes $\lambda$ = 0.46 for determining the 100% nominal flowrate. Recall the purpose of the present experiment is the determination of the bearing response to flowrate variation, for both higher and lower flow rates than the nominal flowrate determined by Eqn (1). Note, however, that for lower than nominal flow testing, pad metal temperature limits and/or elevated vibration determine the lowest allowable flowrate independent of the calculated nominal flow. Conversely, the desired maximum flow rate ideally is large enough to fully bracket the bearings response to flow rate variation as indicated by a declining rate of change of pad metal

temperature, power loss, dynamic force coefficients, etc. for any further increase in flow rate. Since the exact maximum flow rate required to fully define the bearings response cannot be known a priori, a small value for $\lambda$ is chosen, resulting in a sufficiently large maximum flow rate required to fully examine the bearing's response. For comparative reference, per original equipment manufacturer (OEM) specifications for this bearing, the manufacturer recommends a supply flow of 40.1 LPM.

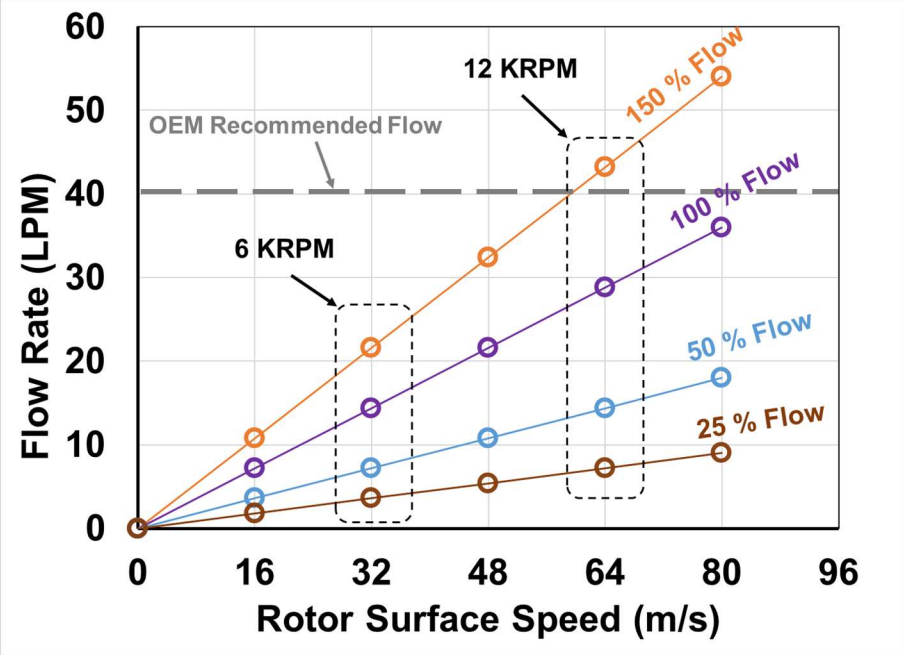


**Figure 9: Estimated lubricant flow rate vs. rotor surface speed for nominal condition (100%) and changes above and below for λ=0.46. Reprinted/adapted from Ref [27].**

### *Estimation of the Bearing Dynamic Force Coefficients*

Evaluating the bearing response to a dynamic load excitation permits identification of the bearing dynamic force coefficients. Generally, the identification procedure outlined below utilizes the known (measured) excitation force provided by the hydraulic shakers along with the resulting displacements and accelerations of the bearing housing relative to the rotor to estimate the bearings dynamic stiffness ($K$), damping ($C$), and virtual mass ($M$) coefficients. This procedure is adapted from Childs and Hale (1994) [21], Rodriguez (2004) [22], and San Andrés (2009) [23].

The bearing is represented as a two degree of freedom ($X$, $Y$) spring-mass-damper system as shown in Figure 10. The developed oil film contributes both direct and cross-coupled stiffness, damping, and mass coefficients.

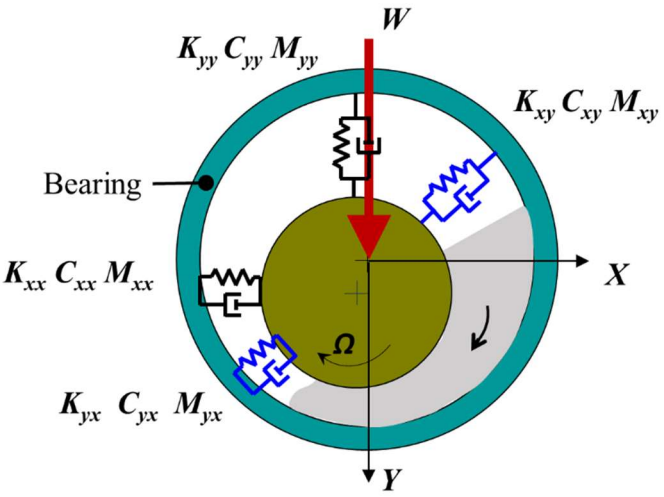


**Figure 10: Schematic representation of the bearing as a spring-mass-damper system. Reprinted/adapted from Ref [27].**

Here, the "direct" force coefficients ($K_{xx}$, $C_{xx}$, $M_{xx}$ or $K_{yy}$, $C_{yy}$, and $M_{yy}$) scale the resulting reaction forces ($X$ or $Y$) acting in the same direction as the bearing ($X$ or $Y$) displacements or their time derivatives. The "cross-coupled" dynamic force coefficients ($K_{xy}$, $C_{xy}$, $M_{xy}$ or $K_{yx}$, $C_{yx}$, and $M_{yx}$) scale the resulting reaction forces orthogonal to the bearing displacement.

The resultant fluid film bearing reaction force, made up of the components along the $X$ and $Y$ directions, is linearized using stiffness ($K$), damping ($C$), and mass ($M$) coefficients and is equal to

$$\begin{bmatrix} f_x - M_b\ddot{x} \\ f_y - M_b\ddot{y} \end{bmatrix} = -\begin{bmatrix} K_{xx} & K_{xy} \\ K_{yx} & K_{yy} \end{bmatrix}\begin{bmatrix} \Delta x \\ \Delta y \end{bmatrix} - \begin{bmatrix} C_{xx} & C_{xy} \\ C_{yx} & C_y \end{bmatrix}\begin{bmatrix} \Delta\dot{x} \\ \Delta\dot{y} \end{bmatrix} - \begin{bmatrix} M_{xx} & M_{xy} \\ M_{yx} & M_{yy} \end{bmatrix}\begin{bmatrix} \Delta\ddot{x} \\ \Delta\ddot{y} \end{bmatrix} \quad (2)$$

where $f_x$ and $f_y$ are the measured excitation forces in the $X$ and $Y$ directions, $M_b$ is the bearing assembly mass = 24 kg ± 0.2 kg[5], and Δx and Δy are the displacements of the bearing housing relative to the shaft.

[5] $M_b$ is the mass of the bearing, bearing housing, and half of the linkage assembly measured directly with a scale prior to assembly.

Transforming Eqn. (2) into the frequency domain by performing a Discrete Fourier Transform gives

$$\begin{bmatrix} F_x - M_b A_x \\ F_y - M_b A_y \end{bmatrix} = \begin{bmatrix} H_{xx} & H_{xy} \\ H_{yx} & H_{yy} \end{bmatrix} \begin{bmatrix} X \\ Y \end{bmatrix} \qquad (3)$$

where $F_i(\omega) = DFT(\, f_i(t))$, $A_x(\omega) = DFT(\ddot{x}(t))$, $A_y(\omega) = DFT(\ddot{y}(t))$, $X_i(\omega) = DFT(\Delta x(t))$, and $Y_i(\omega) = DFT(\Delta y(t))$, etc. Above $H$'s denote the complex dynamic stiffnesses

$$H_{ij} = \left(K_{ij} - \omega^2 M_{ij}\right) + i(\omega C) \qquad i = X,\ Y \qquad (4)$$

Solving for the four $H$'s requires of separate and independent load excitations to yield:

$$\begin{bmatrix} F_{x1} - M_b A_{x1} & F_{x2} - M_b A_{x2} \\ F_{y1} - M_b A_{y1} & F_{y2} - M_b A_{y2} \end{bmatrix} = \begin{bmatrix} H_{xx} & H_{xy} \\ H_{yx} & H_{yy} \end{bmatrix} \begin{bmatrix} X_1 & X_2 \\ Y_1 & Y_2 \end{bmatrix} \qquad (5)$$

where the independent load excitation vectors are $[F_{x1}\ F_{y1}]^{\mathrm{T}}$ and $[F_{x2}\ F_{y2}]^{\mathrm{T}}$. Once the $H$'s are determined from Eqn. (5) at discrete frequencies, then

$$Re\left(H_{ij}\right) \rightarrow \left(K_{ij} - \omega^2 M_{ij}\right), \qquad Ima(H_{ij}) \rightarrow i(\omega C) \qquad i, j = X,\ Y \qquad (6)$$

An estimate of static stiffness is found from the intercept of $Re(H)$ vs. $\omega^2$ and virtual mass from the slope. Similarly, the slope of $Ima(H)$ vs. $\omega$ delivers an estimation of damping coefficient, $C$. The estimations (parameters) are representative of the test data over a certain frequency range when showing a high correlation coefficient ($R^2 > 0.95$). Otherwise, the assumed physical model may be deemed incorrect (not the test data).

Note that the system description provided in equations (2) or (5) above represents the total system response. Specifically, the contribution to stiffness, mass, and damping provided by the bearing oil film *and* that of the test rig structure. To accurately characterize the bearing dynamic performance, the structural $K$, $C$, and $M$ must be separately determined and removed from the operating test results. A separate "dry" excitation performed with the bearing centered over the shaft (i.e. pads not in contact with the rotor surface) and without lubricating oil yields the structural or "dry" system parameters utilizing the identification process described above. The structural

baseline values can then be subtracted from the operating test data to characterize the fluid film performance. Table 3 provides the estimated structural baseline values.

The test apparatus direct and cross-coupled stiffness coefficients are low (< ~3%) compared to the bearing estimated stiffness. Similarly, the structural damping coefficients are less than 3% of the estimated bearing coefficients. The experimentally estimated $M_{xx}$ and $M_{yy}$ compare to the measured bearing housing/bearing assembly mass of 24 kg.

**Table 3: Estimates of support structure stiffness, damping and mass coefficients.**

| | | |
|---|---|---|
| $\boldsymbol{K_{xx}}$ = 0.9 ± 0.2 MN/m | $\boldsymbol{C_{xx}}$ = 0.6 ± 1 kN-s/m | $\boldsymbol{M_{xx}}$ = 22.8 ± 0.3 kg |
| $\boldsymbol{K_{xy}}$ = 0.1 ± 0.2 MN/m | $\boldsymbol{C_{xy}}$ = 0.5 ± 0.3 kN-s/m | $\boldsymbol{M_{xy}}$ = -0.2 ± 0.3 kg |
| $\boldsymbol{K_{yx}}$ = 0.1 ± 0.1 MN/m | $\boldsymbol{C_{yx}}$ = 0.7 ± 0.3 kN-s/m | $\boldsymbol{M_{yx}}$ = 0.4 ± 0.2 kg |
| $\boldsymbol{K_{yy}}$ = 1.4 ± 0.4 MN/m | $\boldsymbol{C_{yy}}$ = 1.0 ± 0.8 kN-s/m | $\boldsymbol{M_{yy}}$ = 25.6 ± 0.6 kg |

### *Cold and Hot Bearing Clearances and Bearing Static Eccentricity*

Bearing clearance and bearing center position measurements provide data used to determine the bearing operating eccentricity and parameters for input to the predictive bearing modeling program. The diametral bearing clearance is the difference between the rotor journal diameter and the pad inside diameter measured at each pivot. The 'bearing center' is the point equidistant from each pad surface. The operating position of the bearing compared to the bearing center determines the bearing eccentricity.

Note that the bearing center position and the bearing clearance both change with operating temperature due to the relative thermal expansion of the bearing shell, bearing housing, pads, pivots, rotor journal, displacement sensors, etc. Several (repeat) measurements of the bearing clearance and estimation of the center position, made throughout the duration of the testing, provide the data needed to determine the bearing eccentricity while accounting for thermal expansion of the assembly.

With the bearing installed in the rig and with a stationary rotor at ($\Omega$= 0), the hydraulic shakers slowly precess the bearing around the shaft. The eddy current sensors (ECS) map the circle traced by the bearing as it precesses. The diameter of the traced circle renders the diametral bearing clearance.

The precession of the bearing mapped by the ECS also provides the data needed to determine the bearing center. The extents of the precession provide the corner points (if possible) and sides to fit a square trace (for a four-pad bearing) to the precession data points. Figure 11 shows a schematic representation of the precession trace, best fit square, best fit center, and the derived bearing clearance circle based on an ECS precession map. A simple solver finds the geometric best-fit center of the square that minimizes the distances from the center to the square edge bisectors (i.e. the pad surfaces). The center of the fit square is defined as the center of the bearing. The bearing center for a particular operating condition subtracts from the measured displacement at each recorded operating condition to determine the relative bearing eccentricity.

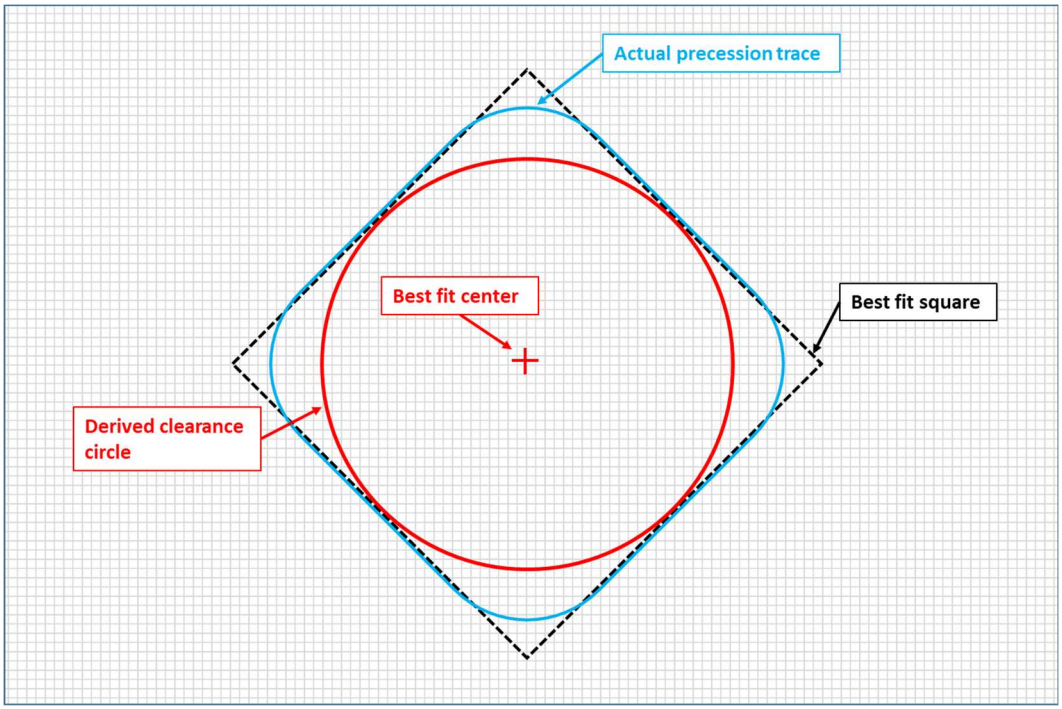


**Figure 11: Schematic representation of an ECS produced precession map of a four-pad TPJB with the best fit square, bearing center, and derived clearance constructions. Reprinted/adapted from Ref [27].**

The experimental data includes a unique ECS map for each set of operational shaft speed and flow combinations. The test procedure sequentially increases the applied specific static loading from the lowest (345 kPa) to the highest (2068 kPa) setting while maintaining a constant shaft speed and flow rate condition, collecting static and dynamic data after each load adjustment. After recording the data for operation with 2068 kPa specific load, the rig operator then quickly reduces the shaft speed and static load to zero, precesses the bearing using the hydraulic actuators, and records the ECS precession map. This ECS map and the derived bearing center and clearance apply to operation with each of the three load increments for a given family of shaft speed/flow rate combinations. Table 4 provides the calculated radial bearing clearances for the ECS precession maps recorded for each combination of shaft speed and flowrate along with the baseline "cold" precession. The "cold" clearance values describe the bearing at ambient temperature (24.4 °C) and prior to the application of lubricant or the commencement of operation. The values listed as bearing clearance are the averages of the four pads' radial clearances calculated using the best fit center.

Note that the bearing precession extents, the bearing center, and the resulting bearing equilibrium position are inherently difficult quantities to determine. Due to the nature of the position measurements, they cannot be performed real-time during operation. By necessity, as described above, the rig operation is halted prior to performing the precession. The position measurements are then made as quickly as possible following the rig shut down. However, some cooling of the test apparatus components occurs as the rig shuts down and during the precision before the position measurements are fully collected. Analogously, any deformation of the bearing/housing that occurs due to the static load condition during operation is not necessary reflected in the position measurement as a (necessarily) reduced radial load is used for the precession. Although these factors can potentially contribute to discrepancies between the operating and as-measured bearing position, the method described above is the best available for estimating the operating condition of the bearing.

**Table 4: Bearing average radial clearances and individual pad radial clearances for the cold condition and for each listed "hot" operating condition.**

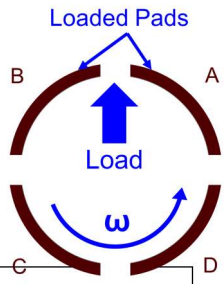


| Operating Condition | Maximum Pad Temperature | Radial Clearance | | | | |
|---|---|---|---|---|---|---|
| | | Average | Pad A | Pad B | Pad C | Pad D |
| "Cold" | 21°C | **115 µm** | 117 µm | 113 µm | 117 µm | 113 µm |
| 6 KRPM, 150% Nominal Flow | 90.8°C | **107 µm** | 109 µm | 106 µm | 109 µm | 106 µm |
| 6 KRPM, 100% Nominal Flow | 93.0°C | **104 µm** | 106 µm | 103 µm | 106 µm | 103 µm |
| 6 KRPM, 50% Nominal Flow | 96.2°C | **106 µm** | 108 µm | 105 µm | 108 µm | 105 µm |
| 6 KRPM, 25% Nominal Flow | 102.2°C | **108 µm** | 110 µm | 107 µm | 110 µm | 107 µm |
| 12 KRPM, 150% Nominal Flow | 102.7°C | **110 µm** | 112 µm | 109 µm | 112 µm | 109 µm |
| 12 KRPM, 100% Nominal Flow | 106.8°C | **105 µm** | 106 µm | 104 µm | 106 µm | 104 µm |
| 12 KRPM,50% Nominal Flow | 112.4°C | **108 µm** | 110 µm | 107 µm | 110 µm | 107 µm |
| 12 KRPM, 25% Nominal Flow | 118.9°C | **108 µm** | 108 µm | 109 µm | 108 µm | 109 µm |

### *Predictions of Bearing Performance*

San Andrés, et al. (2017) [14] develop a computational physics analysis to predict the performance of an evacuated TPJB under variations in lubricant flow. The model and program account for the effect of pad oil film starvation on shaft eccentricity, pad temperature rise, and dynamic force coefficients as a function of excitation frequency, rotor surface speed, bearing configuration, and flowrate. The authors successfully validate the model through comparison to the measured TPJB responses of example four-pad and five-pad tilt pad journal bearings. The work is unique not only for its accurate prediction of static and dynamic TPJB performance but also for its successful prediction of SSV brought on by the reduction in damping of unloaded (starved) side pad vibration modes. For the present work, the inputs to the program include the rotor speed/applied load/flowrate combinations listed in Table 1 and the bearing geometry in listed in Table 2.

# EXPERIMENTAL RESULTS AND DISCUSSION[6]

### *Measurements of Journal Eccentricity and Film Thickness*

Figures 12 and 13 show the journal (bearing) center locus relative to the applied specific load for operation at 6 krpm and 12 krpm, respectively. Conditions of supplied flow are noted in each graph. Figures 14 and 15 show the measured bearing eccentricity vs. oil flowrate. The results demonstrate an expected effect of reducing eccentricity with increasing surface speed due to film stiffening owing to the increased Couette oil flow delivered to the film gap. The results also demonstrate an expected increase in eccentricity mostly parallel to the load vector as load increases for constant speed and constant oil flow.

The results do not display a consistent increasing or decreasing trend vs. change in supplied flowrate for operation between 150% and 50% of the nominal flow rate. However, further reducing the flowrate to less than 50% of nominal and ultimately to the minimum flow observed before halting testing due to pad temperature limitations results in eccentricity increases of 2 μm to 11 μm for operation at 6 krpm and 11 μm to 15 μm for operation at 12 krpm.

The magnitude of the journal eccentricity ($e$), is

$$e = \sqrt{e_X{}^2 + e_Y{}^2} \qquad (7)$$

and is dominated by the magnitude of $e_Y$, the bearing center movement parallel to the load vector, with the trends in total eccentricity governed by this magnitude as described earlier. However, Figure 12 and 13 also reveal a clear decreasing trend in the magnitude of $e_X$ (perpendicular to the load vector and in the direction of journal rotation) with reducing flow. The magnitude of $e_X$ decreases 9 μm, 11 μm, and 12 μm for 345 kPa, 1034 kPa, and 2068 kPa respectively for operation at 6 krpm for a flow rate reduction from 150% of the nominal flow to the minimum flow observed. The magnitude of $e_X$ decreases 21 μm, 25 μm, and 8 μm respectively for the same flow rate reduction while operating at 12 krpm. Figures 16 and 17 highlight the decrease in $e_X$ with respect to a reduction in flow rate. The same figures also show

[6]Parts of this section reprinted/adapted with permission from Ref [27]

the magnitude of $e_Y$ over the same range of flow rates. Note that the magnitudes of $e_Y$ are very similar to the magnitudes of total eccentricity, $e$, presented in Figures 14 and 15.

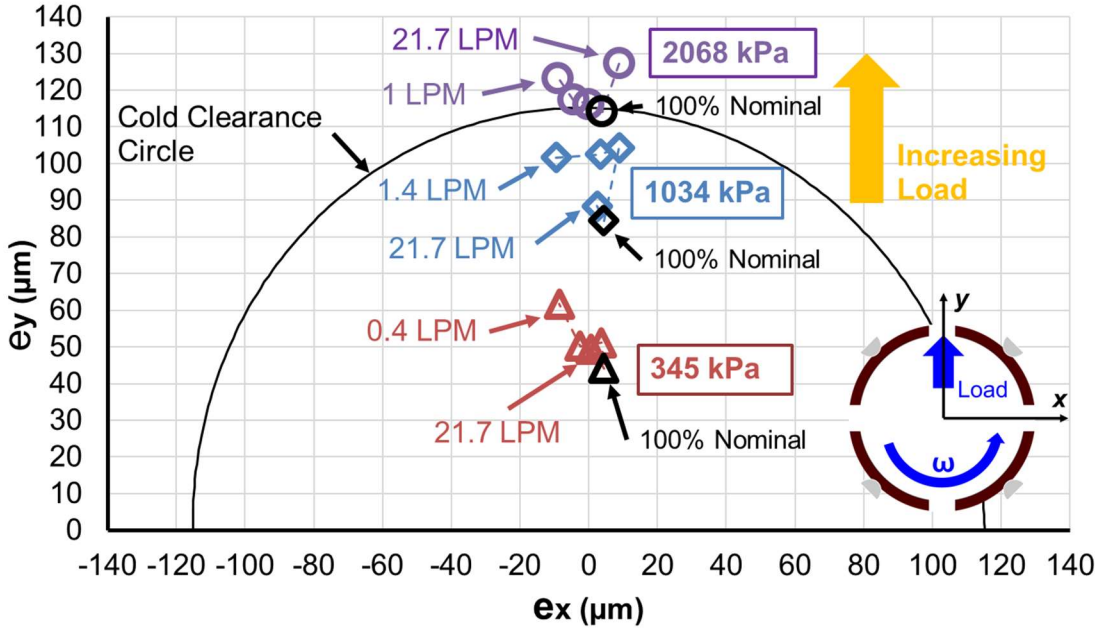


**Figure 12: Bearing center locus $e_Y$ vs. $e_X$ for operation with shaft surface speed = 32 m/s (6 krpm) and under three specific loads, $W_Y/(LD)$= 345 kPa, 1,034 kPa, and 2,068 kPa. Tests conducted at various supply oil flow rates, high to low as noted in graph. Reprinted/adapted from Ref [27].**

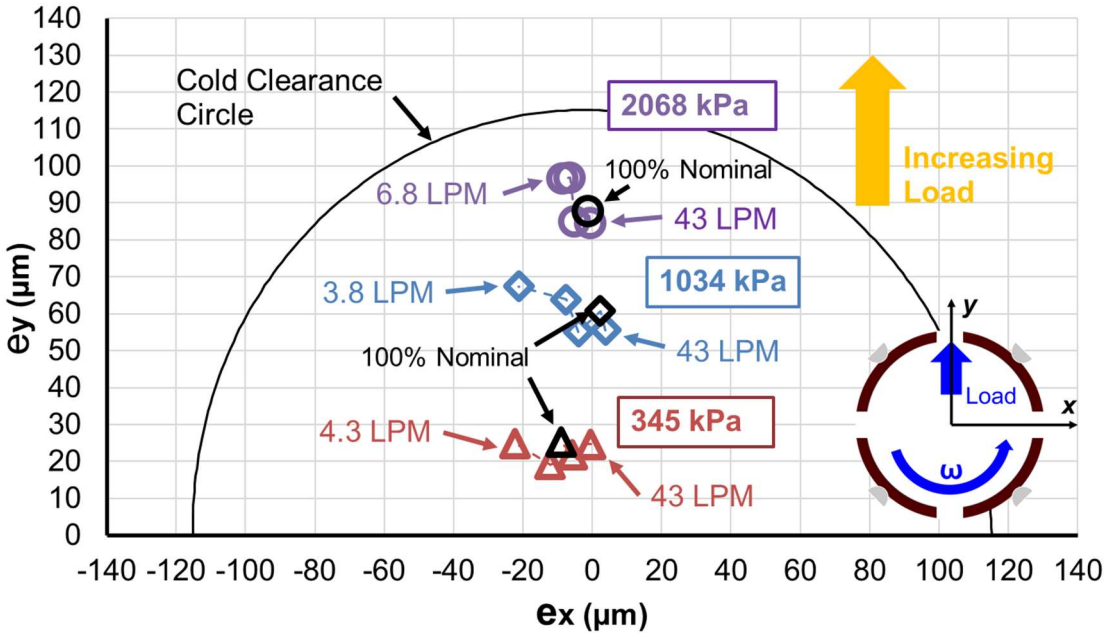


**Figure 13: Bearing center locus $e_Y$ vs. $e_X$ for operation with shaft surface speed = 64 m/s (12 krpm) and under three specific loads, $W_Y$ /($LD$)= 345 kPa, 1,034 kPa, and 2,068 kPa. Tests conducted at various supply oil flow rates, high to low as noted in graph. Reprinted/adapted from Ref [27].**

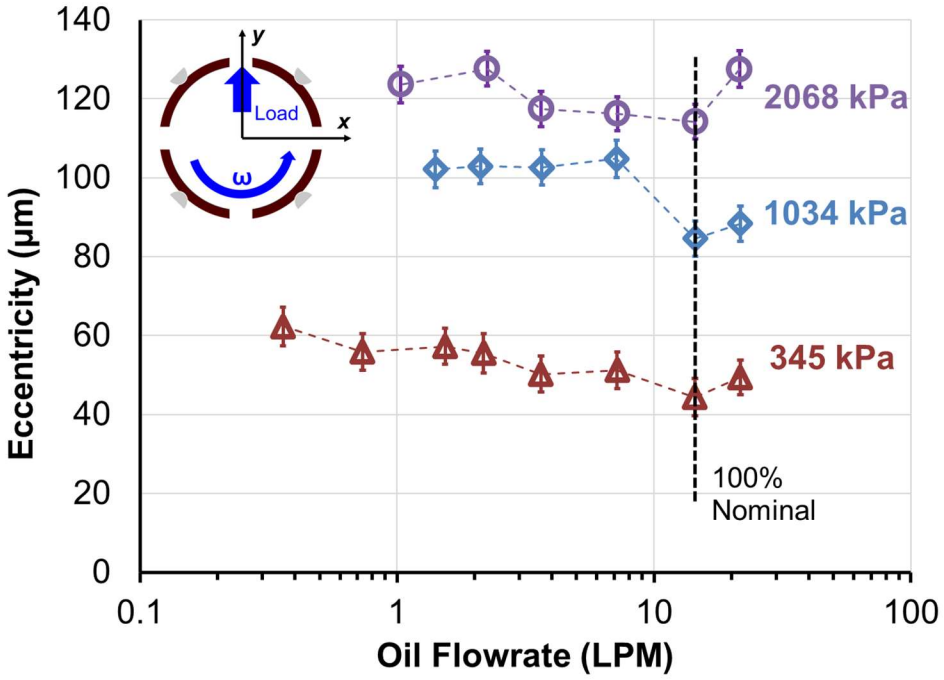


**Figure 14: Bearing eccentricity ($e$) vs. supply flow rate for operation with shaft surface speed = 32 m/s (6 krpm) and under three specific loads, $W_Y$ /($LD$)= 345 kPa, 1,034 kPa, and 2,068 kPa. Reprinted/adapted from Ref [27].**

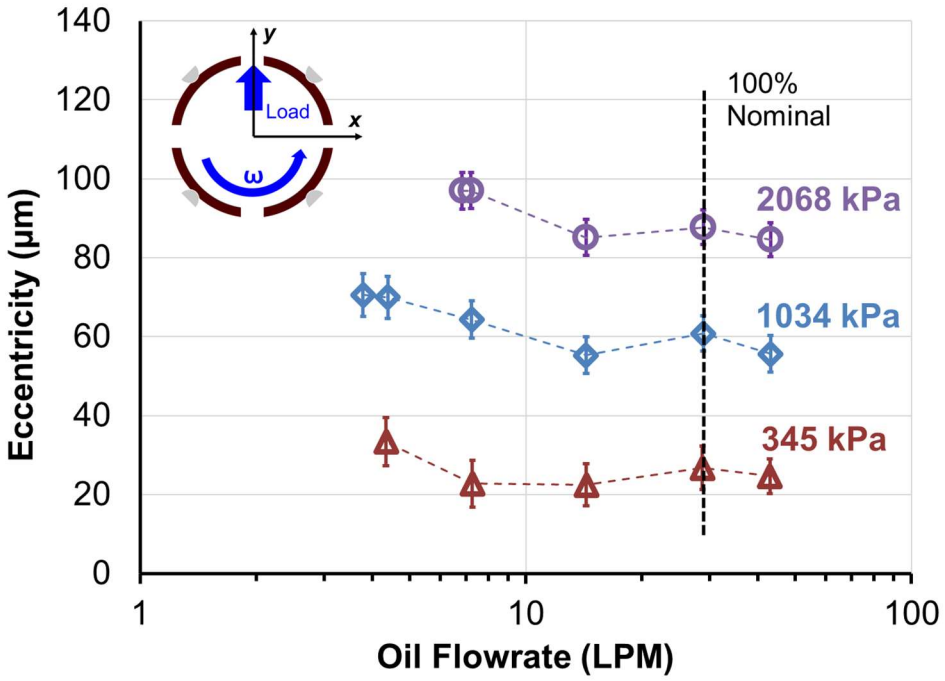


**Figure 15: Bearing eccentricity (*e*) vs. supply flow rate for operation with shaft surface speed = 64 m/s (12 krpm) and under three specific loads, $W_Y/(LD)$=345 kPa, 1,034 kPa, and 2,068 kPa. Reprinted/adapted from Ref [27].**

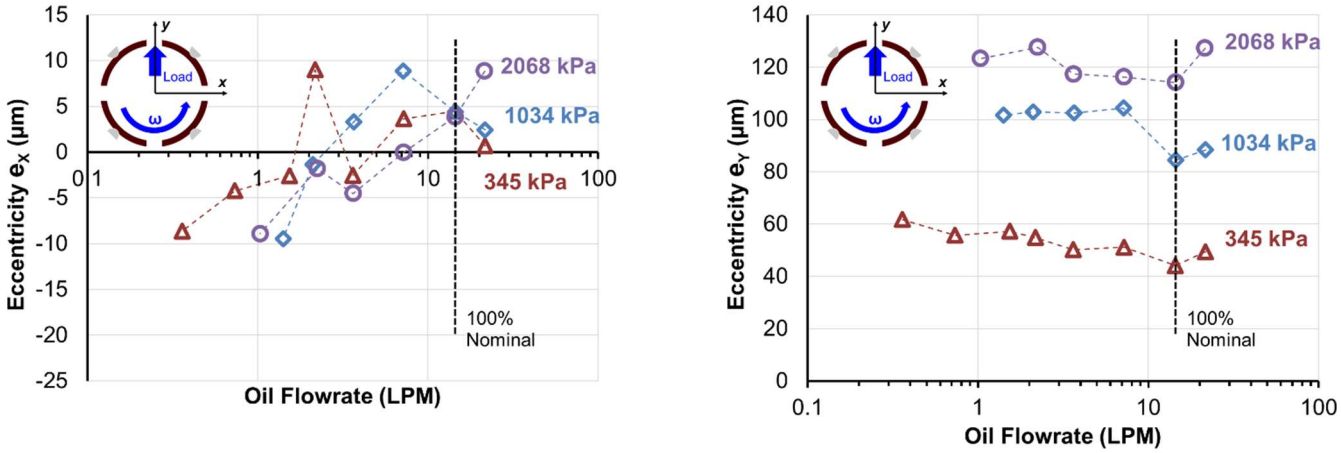


**(a) $e_X$** **(b) $e_Y$**

**Figure 16: Bearing eccentricities $e_X$ (left) and $e_Y$ (right) vs. supply flow rate for operation with shaft surface speed = 32 m/s (6 krpm) and under three specific loads, $W_Y/(LD)$= 345 kPa, 1,034 kPa, and 2,068 kPa.**

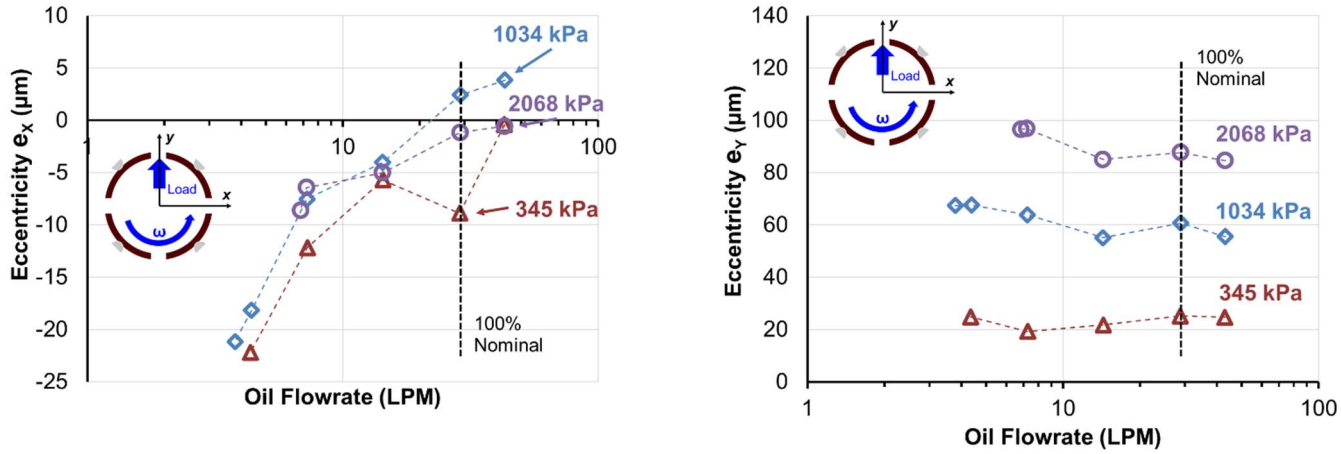


**(a) $e_X$** **(b) $e_Y$**

**Figure 17: Bearing eccentricities $e_X$ (left) and $e_Y$ (right) vs. supply flow rate for operation with shaft surface speed = 64 m/s (12 krpm) and under three specific loads, $W_Y/(LD)$= 345 kPa, 1,034 kPa, and 2,068 kPa.**

Figures 18 and 19 show the estimated minimum film thickness vs. flowrate for operation at 6 krpm and 12 krpm. The minimum film thickness is given as

$$T_{film} = C_{average,\ radial,\ hot} - e \quad (8)$$

and is the difference of the bearing average (hot) radial clearance as presented in Table 4 and the corresponding bearing eccentricity given in Figures 14 or 15. The displacement occurs along a line between Pad A and Pad B, the two loaded pads for this LBP arrangement.

Note that the average radial clearance does not vary dramatically over the observed range of flowrates: 4 μm for all observed flow conditions while operating at 6 krpm and 5 μm for operation at 12 krpm. Recall that the LBP arrangement of the test bearing can, given sufficient load, permit operation at a position slightly outside of the bearing clearance circle. Operation in this condition produces an eccentricity slightly larger than the average radial clearance under the pad pivot resulting in an estimation of a negative film thickness. This is the case for operation at 6 krpm and 2068 kPa applied specific load, resulting in the estimated negative film thicknesses shown in Figure 18. The negative thicknesses are artifacts of the calculation for an LBP arrangement as the film obviously possesses a finite thickness for an operating bearing.

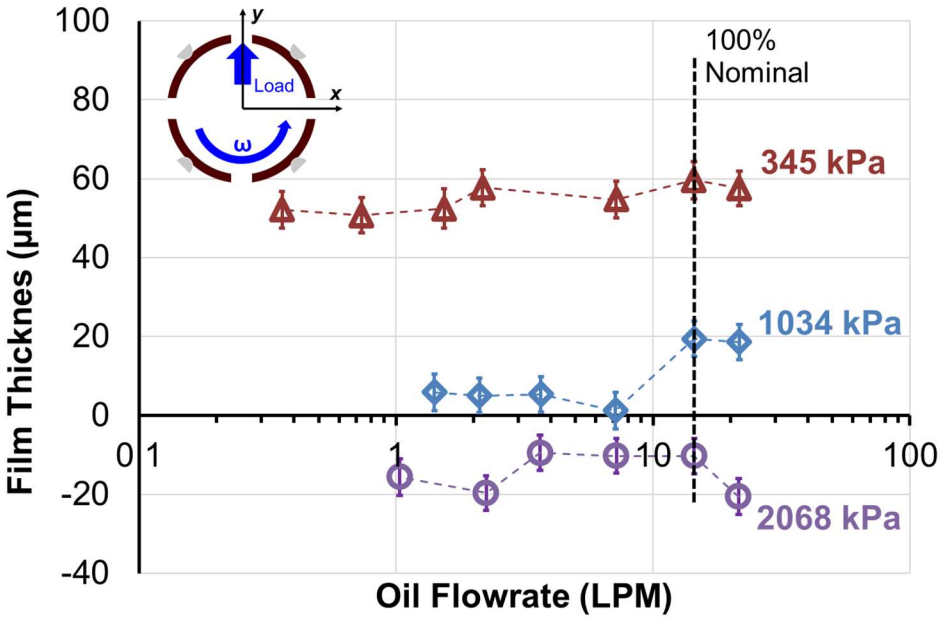


**Figure 18: Estimated minimum film thickness vs. supply flow rate for operation with shaft surface speed = 32 m/s (6 krpm) and under three specific loads, $W_Y/(LD)$= 345 kPa, 1,034 kPa, and 2,068 kPa.**

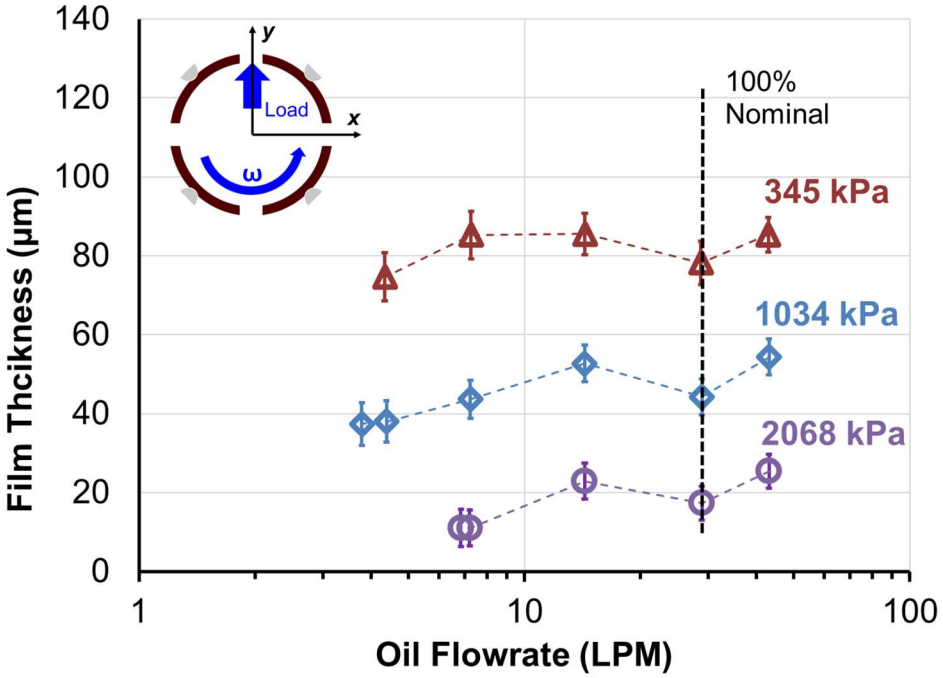


**Figure 19: Estimated minimum film thickness vs. supply flow rate for operation with shaft surface speed = 64 m/s (12 krpm) and under three specific loads, $W_Y/(LD)$= 345 kPa, 1,034 kPa, and 2,068 kPa.**

***Measurement of Pads' Metal Temperature***

Figures 20 and 21 present the pad metal temperature rise above the oil inlet temperature ($T_{in}$ = ~60°C) for operation at 32 m/s (6 krpm) and 64 m/s (12 krpm) respectively for both the loaded pad B and the unloaded pads C and D vs. supplied oil flow rate. The pad metal temperature rise for the loaded pads increases with an increase in load, 5°C to 10°C for each load step increase from 345 kPa to 1034 kPa to 2068 kPa for comparable flow rates for operation at 6 krpm shaft speed. Load step increases for comparable flow rates for operation at 12 krpm result in increases of 5°C to 14°C. Similarly, the pad metal temperature rise is 5°C to 15°C higher for all load conditions when the shaft operates at 64 m/s vs. 32 m/s surface speed. An increase in both parameters, load and surface speed, increases the shear rate of the oil in the hydrodynamic film leading to higher oil and pad surfaces temperatures in the loaded pads. The unloaded pad metal temperature rise displays little dependency on the specific load, but shows a similar 5°C to 17°C increase in temperature with an increase in shaft speed from 6 krpm to 12 krpm for comparable fractions of nominal flow.

The pad metal temperature rise for both the loaded and the unloaded pads is nearly linear when reducing the oil flow from 150% to 50% of the nominal flowrate for operation at both rotor surface speeds. However, supply flowrates less than 50% of the nominal flow produce a dramatic rise in pad metal temperature for any further flow reduction. The steep gradient in pad metal temperature rise for further reduction in flow below 50% of the nominal flow (and especially below 25% of the nominal) reveals that, although the bearing could be successfully operated in this flow regime in a laboratory setting, this flow regime is likely not desirable for long term industrial operation since a disruption amounting to only a few LPM in the delivered oil supply can result in exceedance of pad metal temperature limits. For example, the maximum pad metal temperature for a loaded pad increases by 4°C for a decrease of 7.2 LPM from 100% to 50% of the nominal flow when operating at 6 krpm and 2068 kPa specific load. However, for the same shaft speed and applied load, a decrease of only 1.2 LPM from 10% to 5% of the nominal flow results in a pad metal temperature equaling 120°C, likely an unacceptable result for long term operation in an industrial setting.

The dramatic increase in pad metal temperature (at 6 krpm) for flow rates below 25% of the nominal flow contrasts with previous experimental findings, for both flooded and evacuated end

bearings, such as Dmochowski and Blair (2006) [9] (flooded and evacuated), Nichols (2017) [12] (flooded) and San Andrés (2020) [19] (flooded) showing relatively little change in temperature when reducing the flow rate. However, these works observed operation at relatively higher flowrates as compared to the very low flowrates (1 or less LPM) in the present experiments.

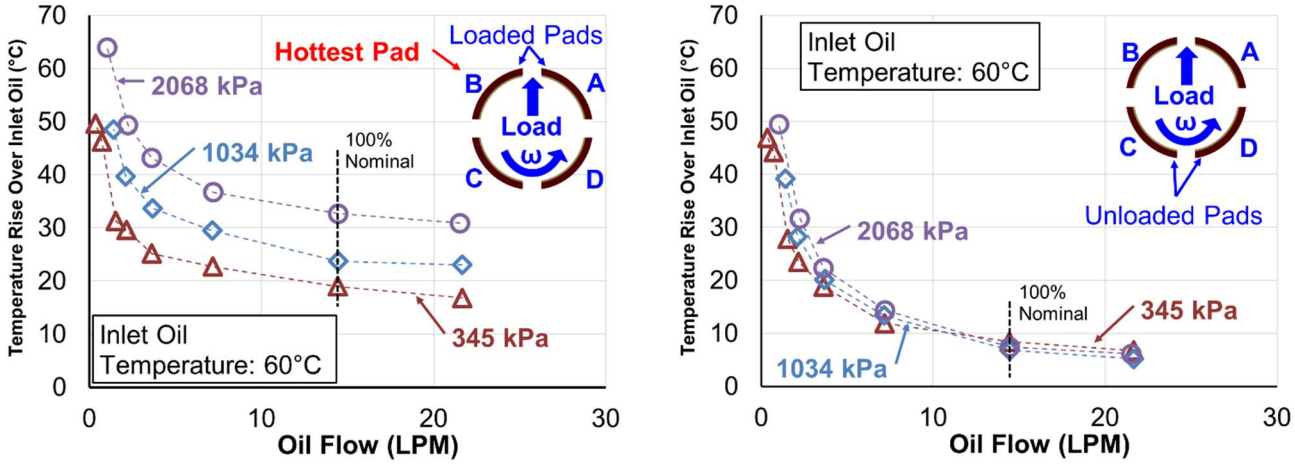


(a) Loaded pad B

(b) Unloaded pad C or D

**Figure 20: Pads maximum temperature rise, (a) loaded and (b) unloaded, vs. supplied flow rate for operation with shaft surface speed = 32 m/s (6 krpm) and under three specific loads, $W_Y/(LD)$=345 kPa, 1,034 kPa, and 2,068 kPa. Rise relative to oil inlet temperature at 60°C. Reprinted/adapted from Ref [27].**

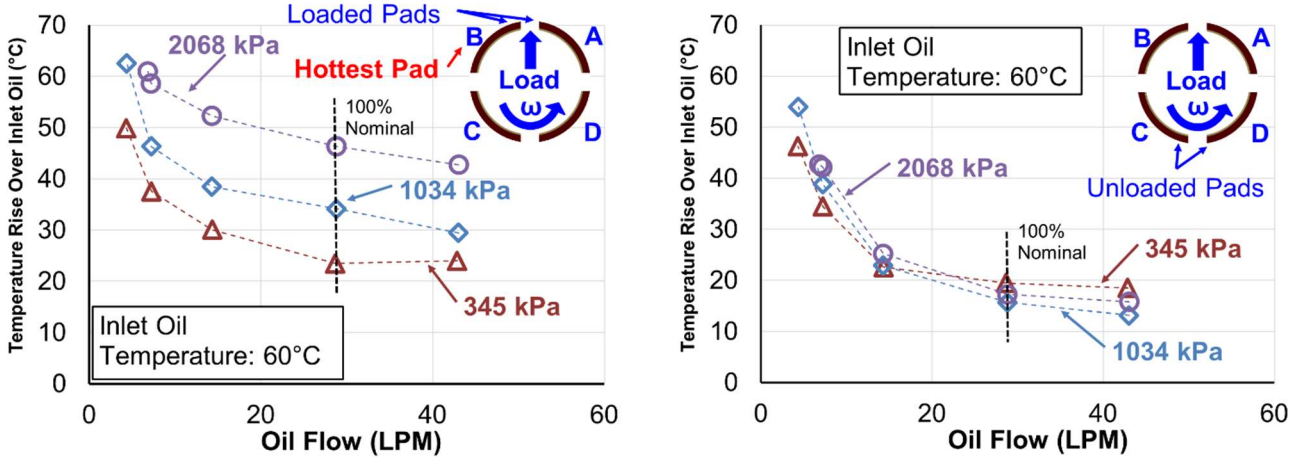


(a) Loaded pad B

(b) Unloaded pad C or D

**Figure 21: Pads maximum temperature rise, (a) loaded and (b) unloaded, vs. supplied flow rate for operation with shaft surface speed = 64 m/s (12 krpm) and under three specific loads, $W_Y/(LD)$=345 kPa, 1,034 kPa, and 2,068 kPa. Rise relative to oil inlet temperature at 60°C. Reprinted/adapted from Ref [27].**

### *Measurement of Oil Exit Temperature*

Thermocouples installed in the endcaps of the test bearing fixture, between the outboard side of the bearing end seals and the oil return drains, offer a measurement of the lubricant temperature soon after it exits the bearing cavity. Figure 22 displays the average exit oil temperature rise over the inlet oil temperature (average temperature of the exiting oil from both sides of the bearing) vs. supply oil flowrate for operation at both 6 krpm and 12 krpm. The average exit oil temperature rise vs. flow rate curves for both rotor surface speeds bear the same sharp temperature increase with reducing flow for operation below 50% of the nominal flow rate as the pad metal temperature data shown in Figures 20 and 21. Note the inset in Figure 22 shows an infrared thermograph of the test bearing and enclosure during operation (right side of inset) with a photograph of the same location (left side of inset) for comparison. The thermograph shows the axial location of the exit oil temperature measurements and presents the reader with a visualization of the relative surface temperatures of the test bearing during operation.

Consideration of these measurements in tandem, pad metal temperature rise and exit oil temperature rise, indicate the drastic change in the relationship between heat generation in the film relative to the mass flow of the oil available to remove the heat as the supplied flow decreases below 50% of the nominal flowrate. The steep increase in temperature(s) for flowrates below 25% of the nominal flow place the bearing in an operating regime where even a small further flow reduction (i.e. even a few LPM) will cause the pads to exceed the allowable Babbitt temperature limit, 121°C for this experiment.

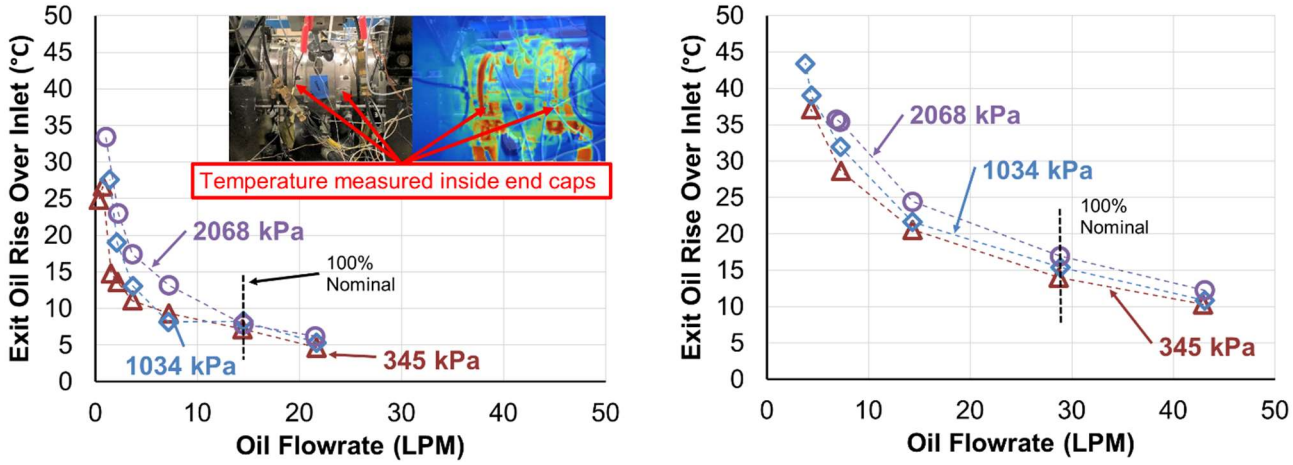


**Figure 22: Exit oil temperature rise vs. supplied flow rate for operation at two shaft surface speeds = 32 and 64 m/s (6 and 12 krpm) and under three specific loads, $W_Y/(LD)$=345 kPa, 1,034 kPa, and 2,068 kPa. Rise relative to oil inlet temperature at 60°C. Exit temperature is the mean value of the temperature measurements on both sides of the bearing. Reprinted/adapted from Ref [27].**

### *Measurement of Temperatures in Oil Supply Annulus*

Four separate thermocouples located in the oil supply annulus measure the local temperature of the lubricant flowing into each supply groove between the pads within the bearing cavity, see Figure 7. The temperature measurements provided by these thermocouples reveal the variation in lubricant temperature around the circumference of the annulus (bearing OD) relative to changes in flow rate, applied load, and shaft speed. For supply flow rates greater than 25% of the nominal flow (3.6 LPM for operation at 6 krpm and 7.2 LPM for operation at 12 krpm), the temperatures recorded in the annulus are uniform and nearly equal to the set target inlet oil temperature (~60°C). However, as the flowrate drops below 25% of the nominal flow, the temperatures diverge from each other and from the target inlet oil temperature. Figure 23 displays a representative example of annulus oil temperatures differing from $T_{in}$ = ~60°C as a result of a sufficiently low flowrate, in this case flow less than 3.6 LPM for operation at 6 krpm and 2068 kPa applied specific load.

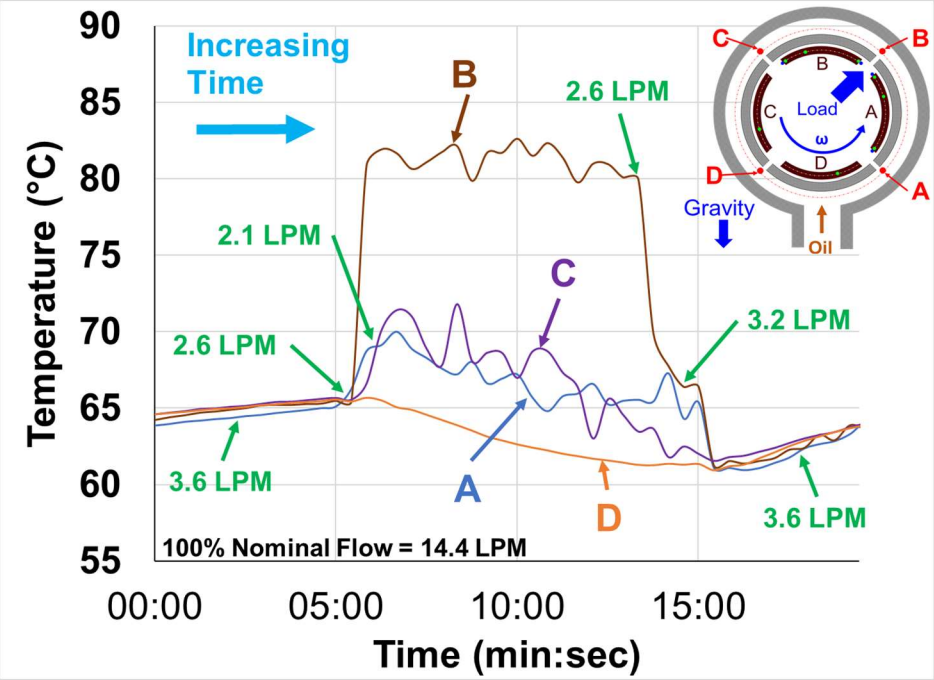


**Figure 23: Oil supply temperatures in supply annulus over a selected time span with rotor speed of 6 krpm and a static load of $W_Y/(LD)$= 2,068 kPa. Oil flow varies between 3.6 LPM and 2.1 LPM. Refer to inset for thermocouple layout. Reprinted/adapted from Ref [27].**

In the figure, the four annulus temperatures are uniform and similar for operation with 3.6 LPM supply flow rate (25% of nominal). A reduction in flow to 2.6 LPM causes the oil supply temperature registered at the "B" location to increase significantly compared to the other three temperatures. As the flow reduces further to 2.1 LPM, the "A" and "C" annulus temperatures increase compared to the "D". Note that when the flow increases (returns) to 3.6 LPM, the annulus temperatures converge sequentially toward the set temperature.

The annulus temperature vs. time measurements also reveal a rapid oil temperature fluctuation at very low flowrates, suggesting a non-steady flow in the region of the thermocouple. Figure 24 shows the annulus temperatures for a selected time span while operating with a flowrate of 2.1 LPM. The annulus temperatures at the A, B, and C locations fluctuate as much as 8°C. Note that the annulus temperature at the D location remains steady throughout the low flow period.

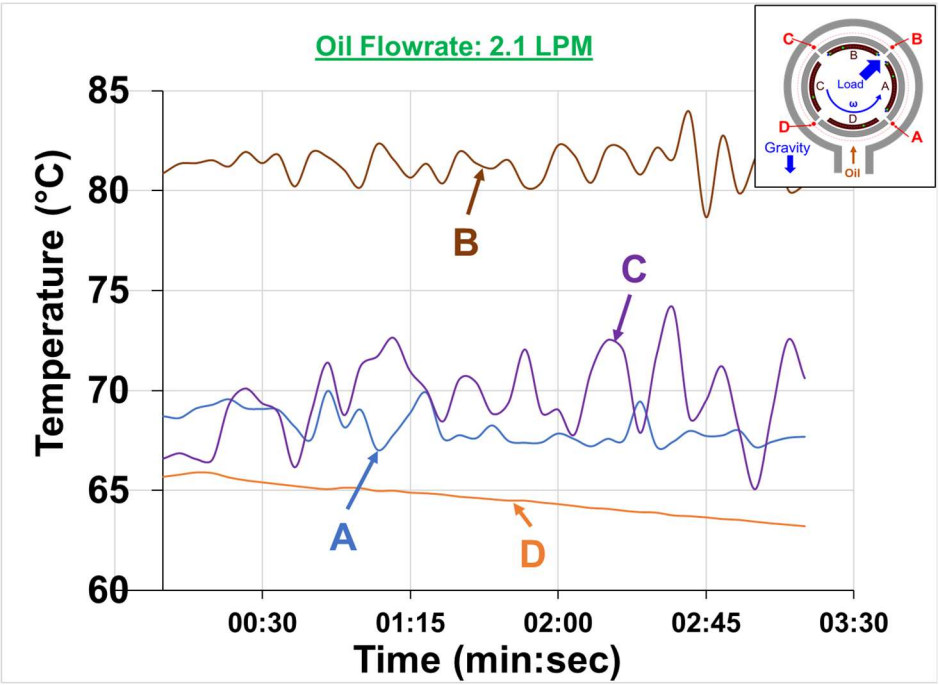


**Figure 24: Oil supply temperatures in supply annulus over a selected time span while operating with rotor speed of 6 krpm, a static load of $W_Y/(LD)$= 2,068 kPa, and a supply flow rate of 2.1 LPM.**

Appendix C provides an extended discussion of the behavior of the oil in the housing annulus and its effect on the bearing behavior observed during operation with very low flows.

### *Measurement of Bearing Drag Torque and Power*

As noted earlier, the test apparatus includes a strain gauge type coupling torque meter that provides a means to directly measure the drive torque (and absorbed power) of the rotor. The pedestal rolling element bearings contribute a small fraction of the total torque measured. As determined from a baseline test without a fluid film bearing installed, the tare torque is (0.5 Nm).

Figures 25 and 26 display the bearing drive torque ($T_{net}$) and drag power ($P_{measured} = T_{net}\omega$) vs. oil flowrate for operation at 6 krpm and 12 krpm rotor speeds and for three applied loads. For operation at 6 krpm, the drag torque and power remain constant for conditions with flows of 150% and 100% of the nominal flowrate, and then begin to decrease rapidly as the flow reduces below 100%. The bearing demonstrates a power savings of between 12% and 19% when comparing operation at 50% nominal flowrate with that at 100% nominal flow.

For operation at 12 krpm, the drag power reduces nearly linearly with a reduction in oil flowrate. Similar to operation at 6 krpm, the power consumption at 50% of the nominal flow is between 13% and 19% less than the power consumption observed at 100% of nominal flow.

Overall machine efficiency improves as parasitic power losses from its bearings decreases. However, for the efficiency improvement to be valuable, an adequate pad metal temperature operating margin must be maintained. Comparing the power loss reduction to the relative pad metal temperature increase as flow rate reduces provides a context to evaluate the value of the efficiency improvement possible as flow rate reduces. For example, the 13% and 19% power loss reductions for a 50% reduction in the nominal flow and for operation at 12 krpm and 345 kPa and 2068 kPa applied load result in pad metal temperatures equal to 90°C and 112°C respectively (note Figures 20 and 21 with a 60°C inlet oil temperature). Some operators may consider these pad metal temperatures to be too warm for long term operation or to provide too little margin to allowable pad metal temperature limits, at least for initial machine design evaluation. As noted earlier, temperatures escalate rapidly for flows below 50% of the nominal and are even less conducive to reliable long-term operation.

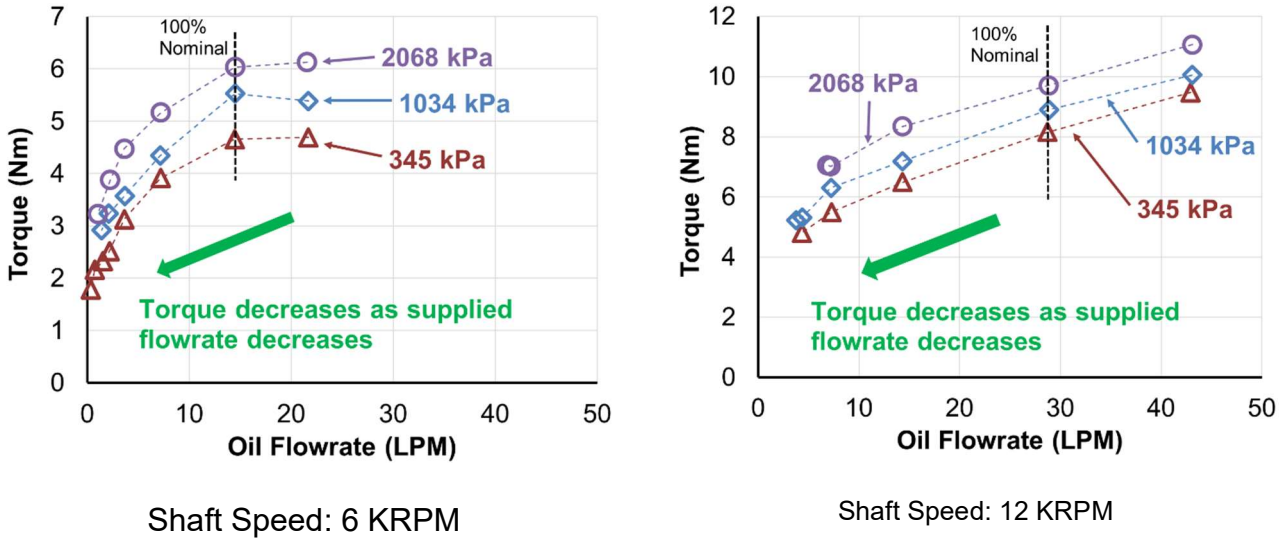


**Figure 25: Measured bearing drag torque vs. supplied flow rate for operation at two shaft surface speeds = 32 and 64 m/s (6 and 12 krpm) and under three specific loads, $W_Y/(LD)$= 345 kPa, 1,034 kPa, and 2,068 kPa. Reprinted/adapted from Ref [27].**

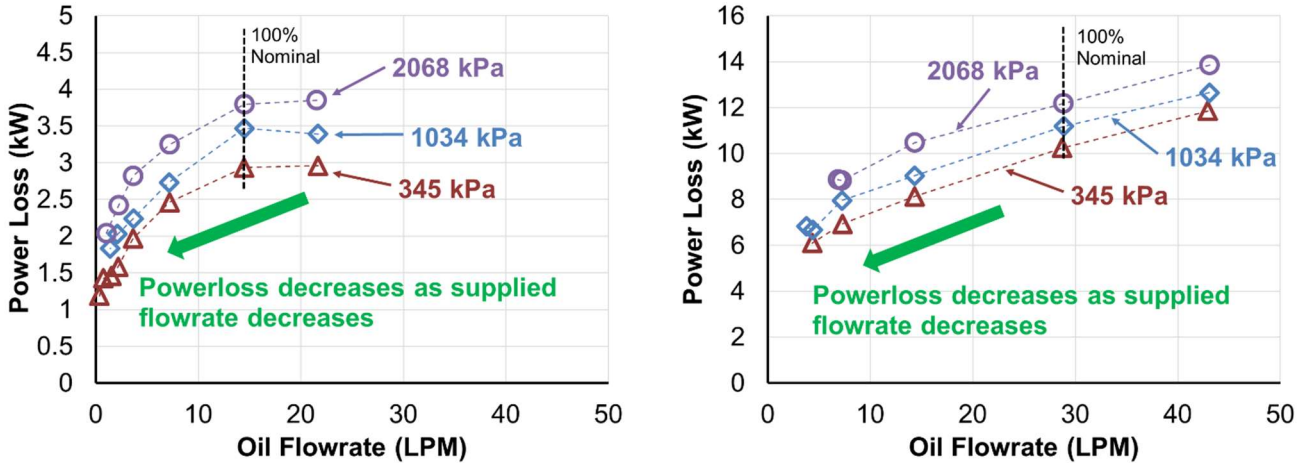


**Figure 26: Shear drag power loss vs. supplied flow rate for operation at two shaft surface speeds = 32 and 64 m/s (6 and 12 krpm) and under three specific loads, *W*/(*LD*)=345 kPa, 1,034 kPa, and 2,068 kPa. Reprinted/adapted from Ref [27].**

An estimate of the heat carried away by the lubricant flow as it travels through the bearing provides an alternate means to estimate the bearing drag power:

$$P_{est,thermal} = \frac{\rho C_p Q}{\kappa}(T_{exit} - T_{inlet}) \qquad (9)$$

Above $\rho$ is the fluid density, $C_p$ is the lubricant specific heat, $Q$ is the supplied lubricant volumetric flow rate, $T_{inlet}$ and $T_{exit}$ are the inlet temperature and exit temperature of the lubricant, respectively. $\kappa$ is an empirical coefficient describing the fraction of mechanical energy carried by the lubricant. Here $\kappa \cong 1$ and is found by solving Eqn. (9) for $\kappa$ after setting $P_{est,thermal}$ equal to $P_{measured}$ for 150% of nominal flow at 6 krpm[7].

Figure 27 shows $P_{est,thermal}$ as a percentage of $P_{measured}$ vs. flowrate for operation at two shaft surface speeds and under three specific loads. The percentage value is given as

$$P_{est,thermal}\ as\ a\ \%\ P_{measured} = \left(\frac{P_{est,therm}}{P_{measured}}\right) x\ 100 \qquad (10)$$

where a value equal to 100% indicates $P_{est,thermal}$ is equal to $P_{measured}$, a value less than 100% indicates $P_{est,thermal} < P_{measured}$, and a value greater than 100% indicates $P_{est,thermal} > P_{measured}$.

[7] Values for $\kappa$ found at for operation at other flow conditions are likely different than the value found for operation at 150% of nominal flow.

By definition, the power loss estimated from the heat carried by the lubricant equals the measured power loss for 150% of the nominal flow at 6 krpm. However, for flows less than 150%, the power loss is increasingly underestimated as flowrate reduces. For operation at 12 krpm, the power loss overestimates the measure power loss for operation with all flows greater than 50% of the nominal flow rate.

The fidelity of the power loss estimate based on oil flow and temperature difference depends mainly on the proper location of the end cap thermocouples to ensure adequate immersion in the exit oil stream as it leaves the bearing end seals. Without complete immersion in the exit oil, the temperature measurement can be altered by the buffering air that is also present in the exit chamber. Complete immersion of the thermocouple junction for all operating conditions cannot be confirmed with the present test apparatus as visual observation of the oil flow over the exit chamber thermocouple is not possible.

Also note that the bearing stator and rotor both remove heat from the bearing cavity in addition to that carried by the oil. This heat removal can affect the accuracy of the power loss estimate. For sufficiently high flowrates, and for any selection of $\kappa$, the ratio of heat lost to the surroundings compared to heat carried to the exit oil measurement location is lower than for operation at low flow rates. For a fixed $\kappa$, this factor results in an overstatement of thermally estimated power loss at high flow rates and an understated loss at low flow rates. This effect can be seen in the power loss estimates for both shaft speeds, with cross over points between overestimate and underestimate of the bearing power loss as flow rate reduces below 50% and 25% of the nominal flow for 6 krpm and 12 krpm, respectively. The results underscore the difficulty in obtaining an accurate power loss estimate using exit temperature due to the difficulty in obtaining an accurate exit oil temperature and the difficulty in selecting the appropriate value for $\kappa$.

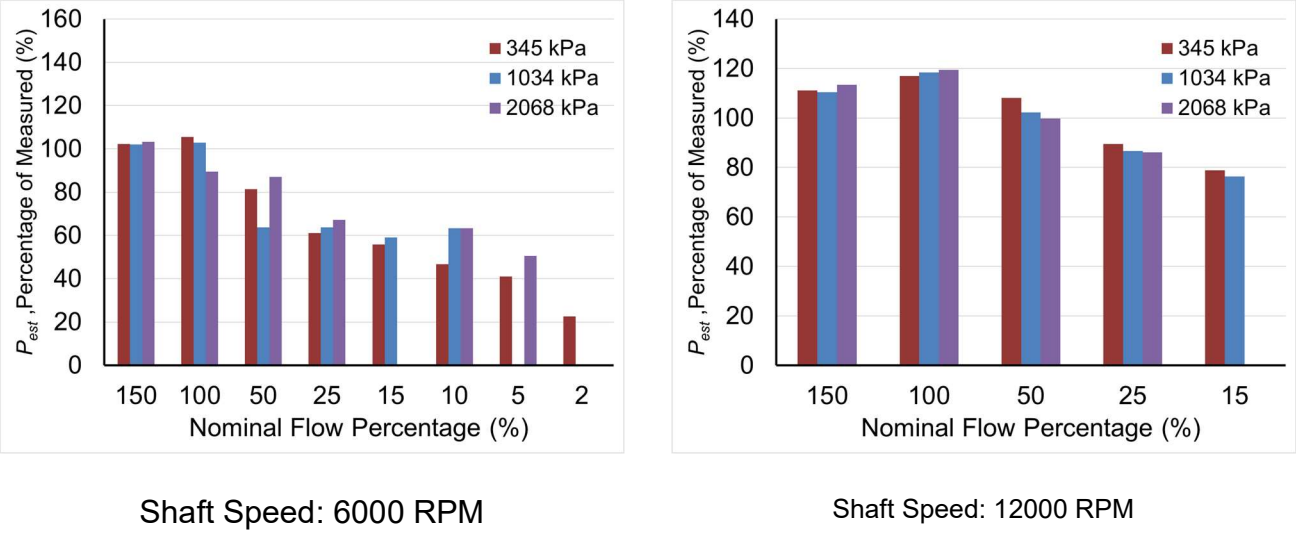


**Figure 27: Estimated drag power loss as a percentage of measured drag power vs. lubricant flow rate (% nominal) at two shaft surface speeds = 32 and 64 m/s (6 and 12 krpm) and under three specific loads, $W_Y/(LD)$= 345 kPa, 1,034 kPa, and 2,068 kPa. Reprinted/adapted from Ref [27].**

### *Evidence of Subsynchronous Bearing Motions at Low Oil Supply Flow Rate*

Figure 28 shows representative plots of the *Y*-displacement amplitude spectra for operation at 32 m/s (6000 rpm), a low 345 kPa specific load, and two low magnitude flowrates. As the flowrate decreases from 15% to 2% of the nominal flow the spectra display the emergence of subsynchronous vibration, specifically SSV "hash" discernable as a broad band signal below the synchronous frequency (100 Hz) and lacking discrete frequency peaks as described in DeCamillo, et al. (2008) [11]. However, the amplitude of the SSV hash at 2% nominal flowrate is low compared to the synchronous vibration amplitude and low overall. Note the bearing still operated stably without showing an excessive overall vibration magnitude.

Earlier investigations into the onset of SSV, for example Nichols (2017) [12] and DeCamillo, et al. (2008) [11], attribute the onset of shaft SSV to pad rotational oscillations forcing vibration of the shaft as the flowrate reduces. DeCamillo, et al. [11] provide experimental evidence in the form of directly measured pad motion showing that shaft vibration correlates to pad vibration manifesting in the side pad (or pads) orthogonal to the load direction. Note that DeCamillo, et al. [11] show that the completely unloaded pads (i.e. those pads diametrically opposed to the load vector) can also experience significant rotational excitation as flow reduces, however the pad vibration for these fully unloaded pads is rarely correlates to the emergence of shaft SSV. Further,

San Andres, et al. (2017) [14] present a full-coefficient bearing model predicting the decrease in the magnitude of the bearing's horizontal damping force coefficient as flow decreases. The authors successfully correlate the reduction of both horizontal damping and the damping of pad rotational modes to the onset of SSV in an operating machine.

The predicted decrease in damping in San Andres, et al. (2017) [14], considered with the experimentally measured side pad vibration correlated with shaft SSV reported in DeCamillo, et al. (2008) [11] suggest that as the horizontal damping decreases with decreasing flowrate the shaft is left increasingly vulnerable to forced SSV from the emerging excitation of partially starved side pads. The estimated magnitude of the damping force coefficient for the present experiment is shown (later) to decrease with reducing flowrate. It is reasonable to suspect the decrease in the magnitude of damping to leave the system more vulnerable to subsynchronous excitation from one or more of the pads' excitation. However, the exact pad or pads, if any, that become excited at low oil flows cannot be confirmed as pad motion measurements are not part of the scope of this experiment.

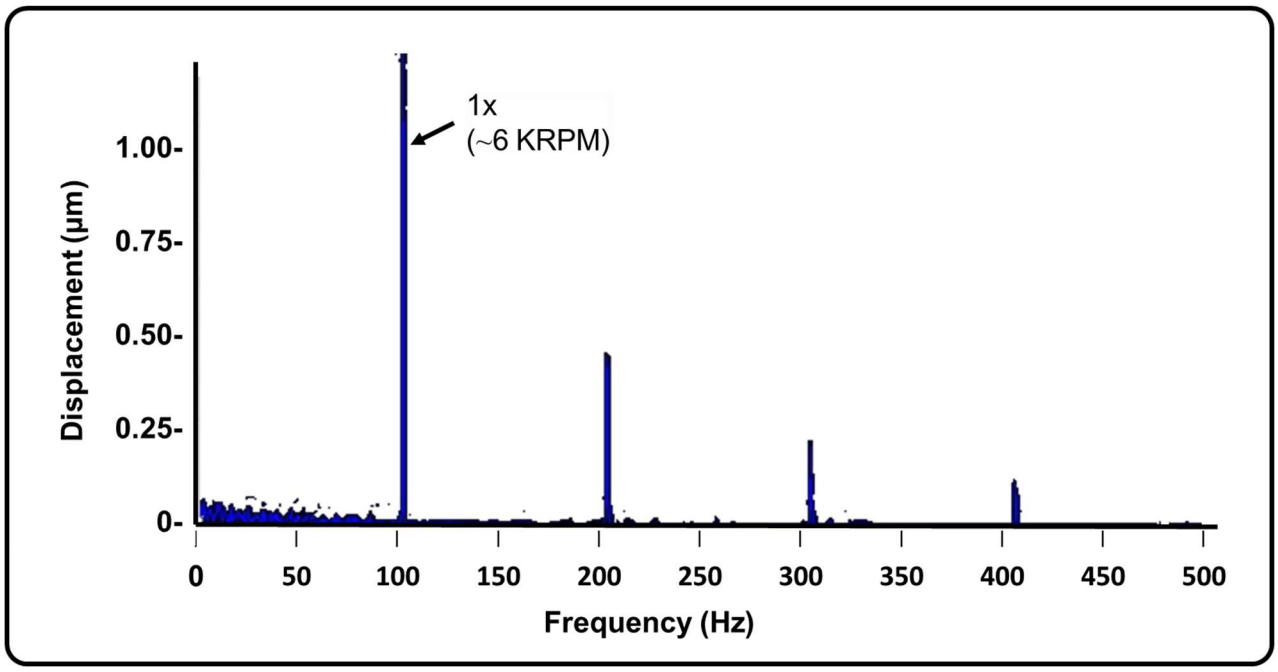


(a) 15% nominal flowrate

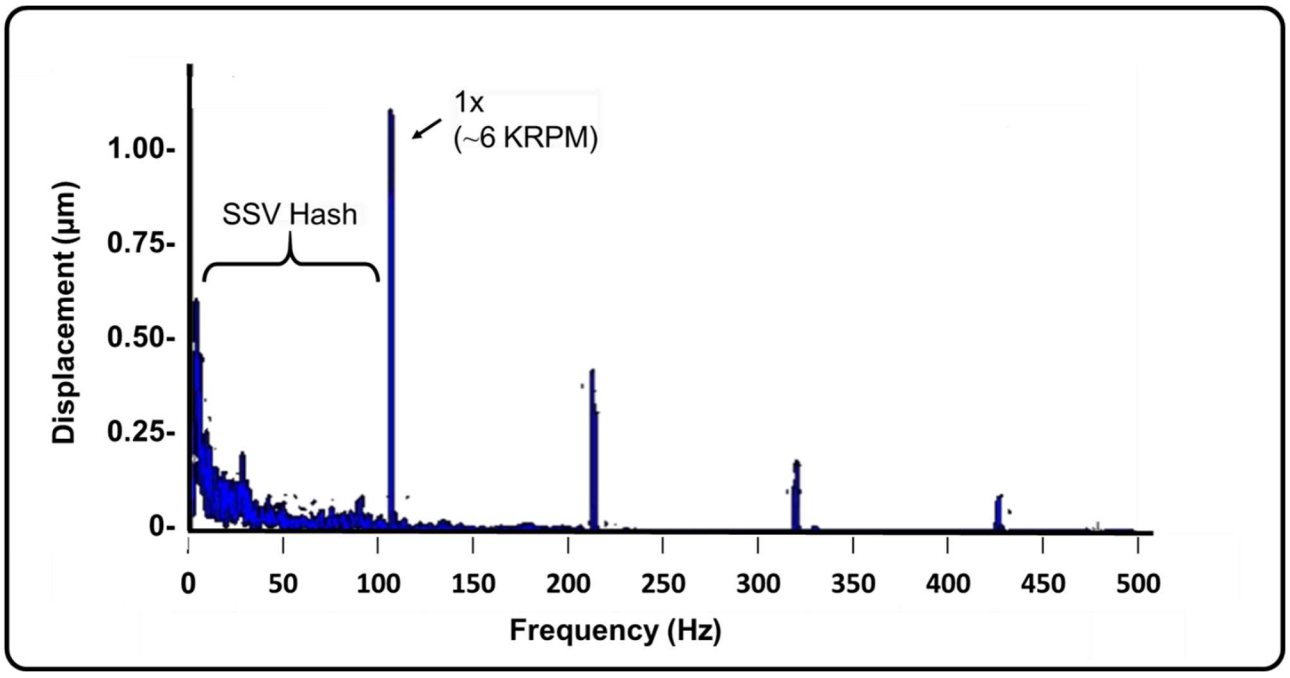


(b) 2% nominal flowrate

**Figure 28: Spectra of bearing displacement amplitude in the *Y*-direction vs. frequency and depicting the emergence of SSV hash as flowrate reduces from 15% of nominal flow (a) to 2% of nominal flow (b) while operating with rotor speed of 6 krpm and a static load of $W_y/(LD)$= 345 kPa. Reprinted/adapted from Ref [27].**

***Experimentally Derived Complex Dynamic Stiffnesses for Test Bearing***

Figures 29 and 30 present the real part of the complex impedance(s) $H_{xx}$ and $H_{yy}$ vs. frequency for operation at 6000 rpm and 12,000 rpm, respectively, and under three applied load conditions. Each graph shows the physical parameter for four oil flow rates. Recall that that direction $Y$ is along the applied static load vector.

The figures reveal Re($H_{xx}$) and Re($H_{yy}$) are nearly independent of flowrate and that Re($H_{xx}$) is approximately equal to Re($H_{yy}$) for operation at 6 krpm and 345 kPa and 1034 kPa specific loads. The invariance of the impedance with flow rate indicates that the estimated static (and dynamic) stiffnesses are also independent of flow rate variation. Operation at a specific load of 2,068 kPa displays different behavior than that for the lighter loads. Re($H_{xx}$) and Re($H_{yy}$) increase slightly as flow rate decreases thus indicating a slight stiffening with decreasing flow rate. Additionally, Re($H_{yy}$) is greater than Re($H_{xx}$) for all flowrates thus showing the stiffness in the load direction to exceed that in the orthogonal direction.

Operation at 12 krpm rotor speed contrasts with operation at 6 krpm in that Re($H_{xx}$) and Re($H_{yy}$) *decrease* with decreasing flow for 345 kPa specific load. This decrease indicates a slight softening of the bearing with decreasing flow at the lightest specific load. Re($H_{xx}$) and Re($H_{yy}$) are mostly invariant for operation at 1034 kPa and 2068 kPa.

Note the pronounced curvature and decreasing magnitude of Re($H$) with increasing $\omega$ for operation at 12 krpm, contrasting with the invariant behavior of the Re($H$) for increasing $\omega$ operation at 6 krpm. Recalling the Re($H$)$\rightarrow$($K$-$\omega^2 M$), the downward curvature for operation at 12 krpm indicates the influence of increased added mass for operation at the highest surface speed.

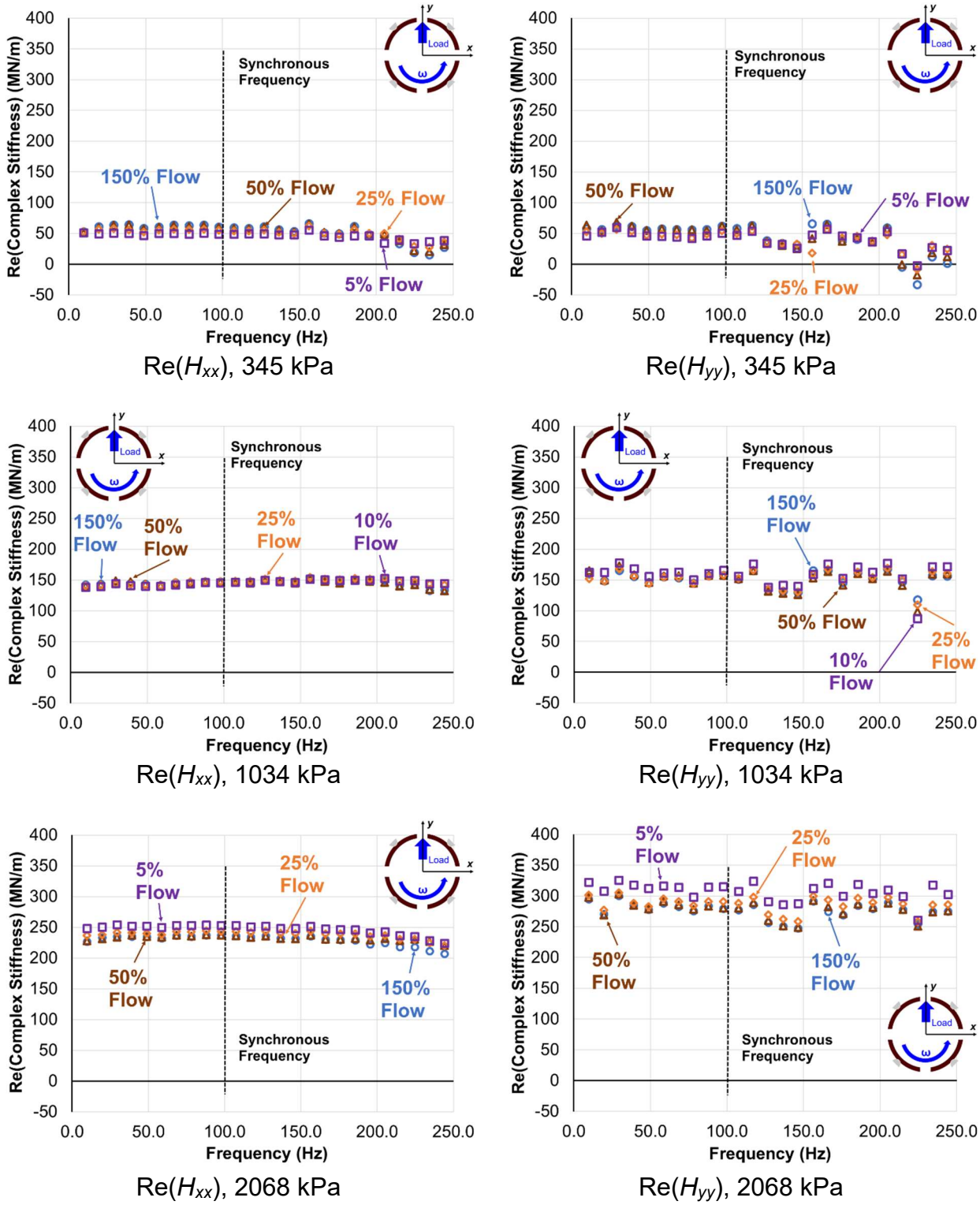


**Figure 29: Real part of the complex stiffnesses, $H_{xx}$ (left) and $H_{yy}$ (right) vs. excitation frequency (Hz) for four oil flowrates (as % nominal flow) and for operation at surface speed = 32 m/s (6 krpm) under three specific loads, $W_Y/(LD)$= 345 kPa, 1,034 kPa, and 2,068 kPa. Reprinted/adapted from Ref [27].**

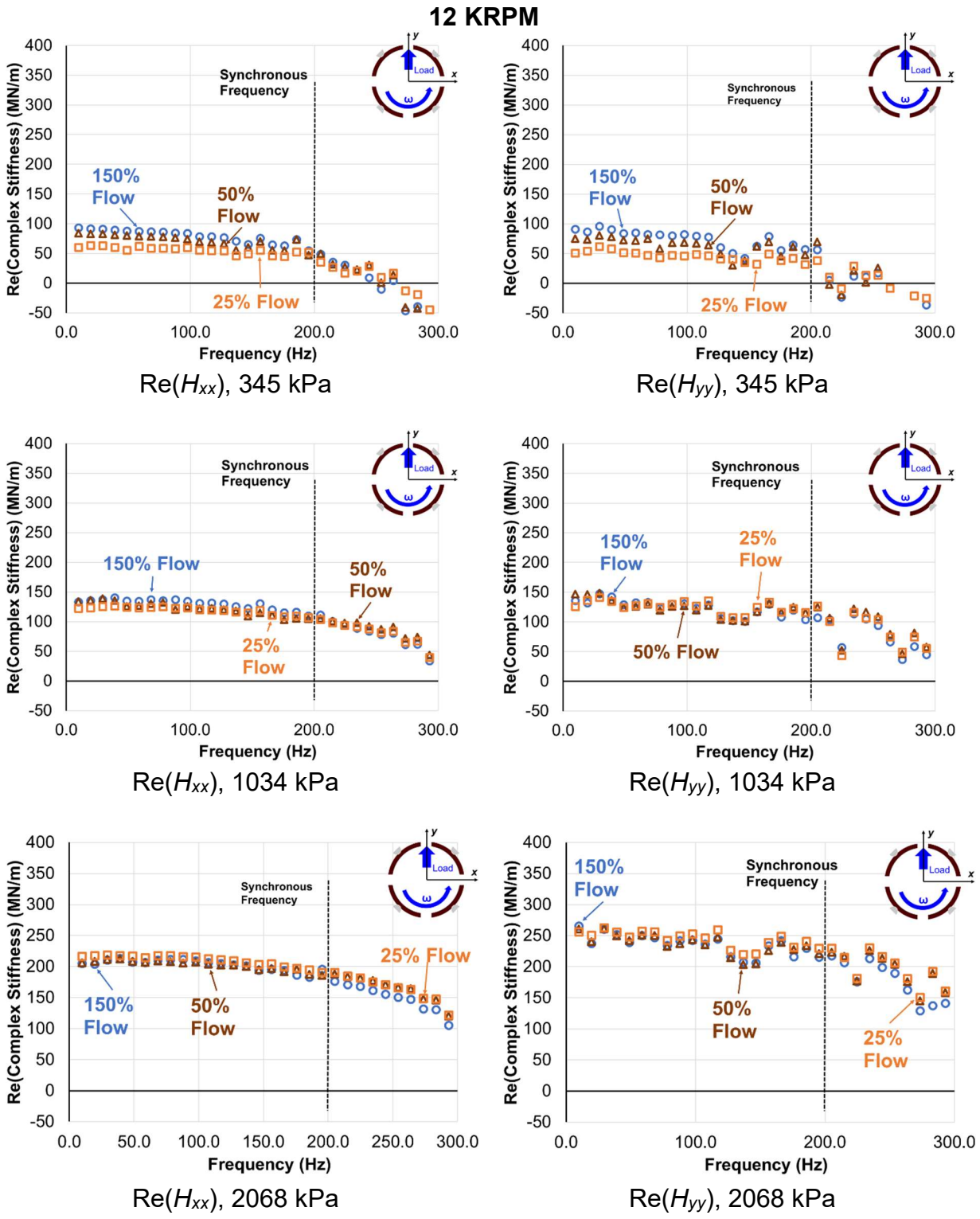


**Figure 30: Real part of the complex stiffnesses, $H_{xx}$ (left) and $H_{yy}$ (right) vs. excitation frequency (Hz) for four oil flowrates (as % nominal flow) and for operation at surface speed = 64 m/s (12 krpm) under three specific loads, $W_Y/(LD)$= 345 kPa, 1,034 kPa, and 2,068 kPa. Reprinted/adapted from Ref [27].**

Figures 31 and 32 present the imaginary part of the complex stiffnesses $H_{xx}$ and $H_{yy}$ vs. frequency for operation at 6 krpm and 12 krpm, respectively, and under three specific loads. Each graph shows data for distinct oil flow rates expressed as % of the nominal flow condition. The slope of the best fit line of Im($H$) vs. $\omega$ produces an estimate of the bearing damping coefficient(s). The experimental results show Im($H_{xx}$) and Im($H_{yy}$) rate of increase with excitation frequency reduces for frequencies above 1X, thus indicating a change in slope to occur above the synchronous frequency. Presently, for the fit yielding the reported damping coefficient(s), the highest frequency range includes rotor speed frequency (1X).

The magnitudes of both Im($H_{xx}$) and Im($H_{yy}$) are larger for the same excitation frequencies and nominal flow rate fractions for operation at 6 krpm compared to 12 krpm, indicating the increased ability for the bearing to dissipate energy when operating at the lower shaft speed. The increased magnitude(s) of Im($H$) at 6 krpm vs. 12 krpm shaft speed result in an increase in the magnitude of the damping coefficient (shown later) of between 24% and 105%. The largest increases in the damping coefficient occur at the lowest comparable flow between the two shaft speeds, 25% of the nominal flow rate, for each of the three applied loads. Additionally, the magnitudes of Im($H_{xx}$) are not perfectly symmetrical to Im($H_{yy}$). Im($H_{yy}$) is greater than Im($H_{xx}$) for all flows and load combinations for operation at 12 krpm shaft speed. Im($H_{yy}$) is greater than Im($H_{xx}$) for all flow rates with 1034 kPa or 2068 kPa for operation at 6 krpm, resulting in damping coefficients 10% to 41% higher in the load direction. The converse is true for operation at 345 kPa applied specific load (and 6 krpm) with the damping coefficient 1% to 10% more in the direction orthogonal to the load.

Additionally, note the droop in the plot of Im($H$) vs. $\omega$ compared to a line of constant slope fit between zero and synchronous excitation frequencies. The droop underscores the fact that the estimated damping coefficient derived from application of the K-C-M model described in Childs and Hale (1994) [21] is valid only for the description of the bearing between zero and approximately the synchronous excitation frequencies.

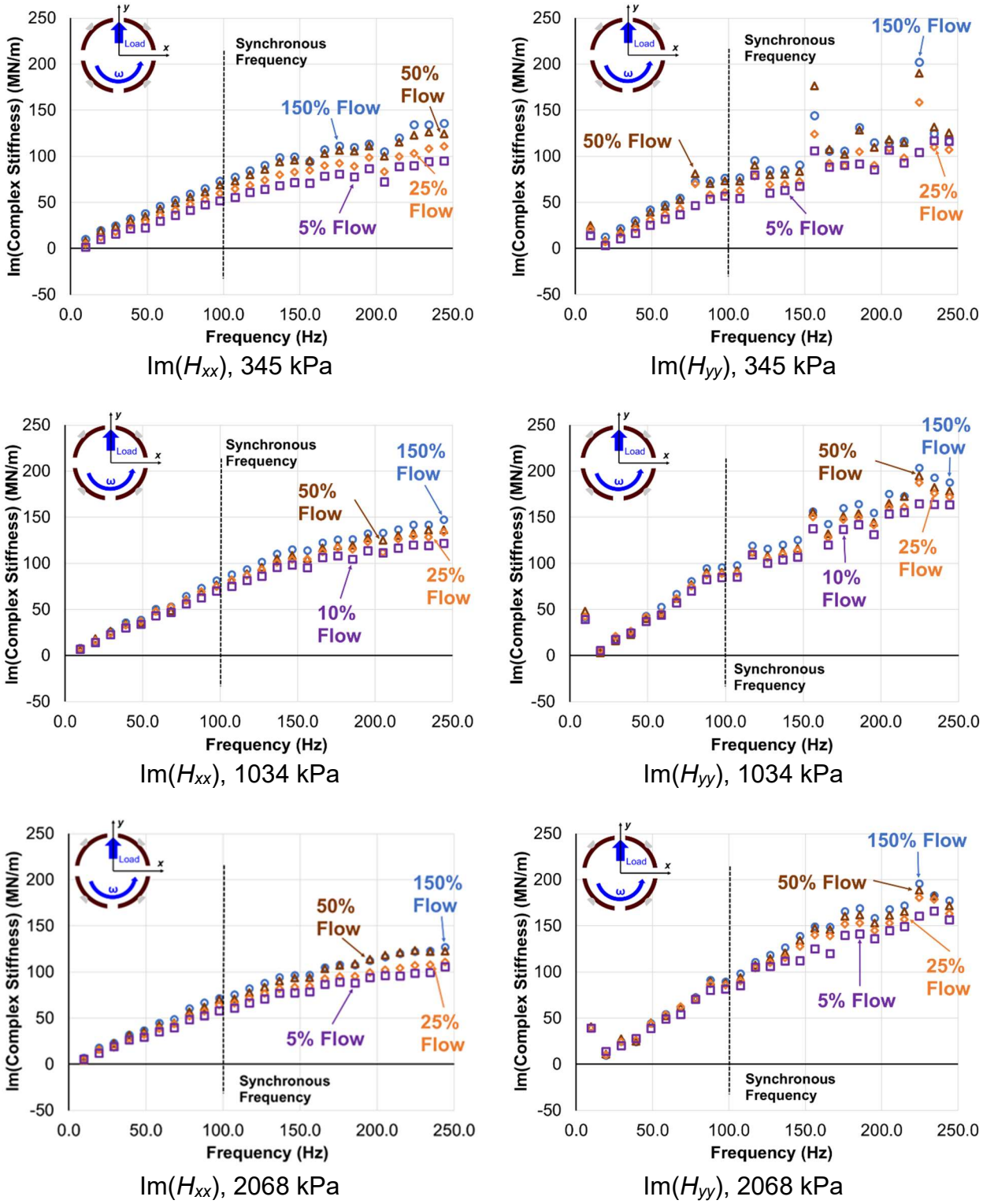


**Figure 31: Imaginary part of the complex stiffnesses, $H_{xx}$ (left) and $H_{yy}$ (right) vs. excitation frequency (Hz) for four oil flowrates (as % nominal flow) and for operation at surface speed = 32 m/s (6 krpm) under three specific loads, $W_Y/(LD)$= 345 kPa, 1,034 kPa, and 2,068 kPa. Reprinted/adapted from Ref [27].**

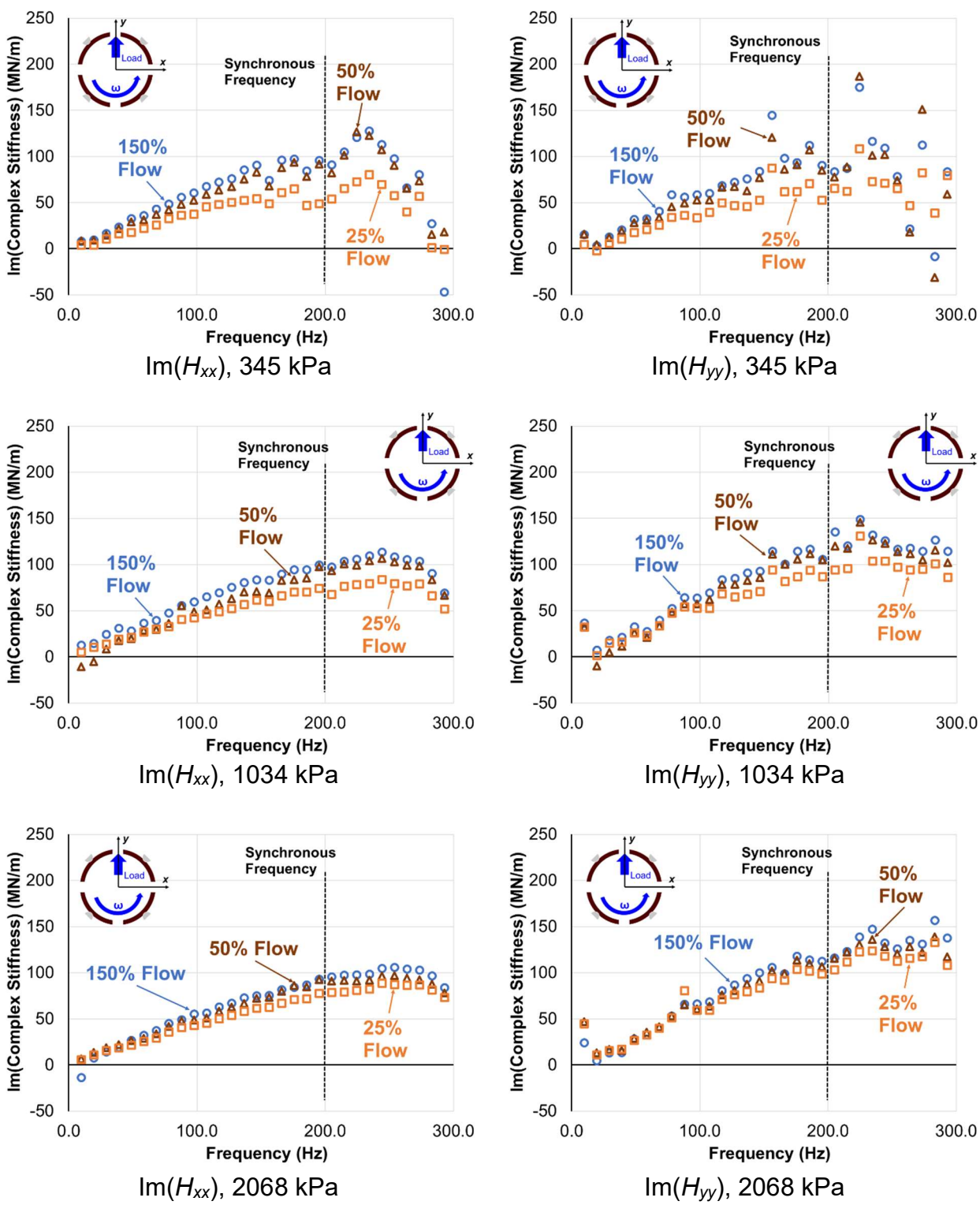


**Figure 32: Imaginary part of the complex stiffnesses, $H_{xx}$ (left) and $H_{yy}$ (right) vs. excitation frequency (Hz) for three oil flowrates (as % nominal flow) and for operation at surface speed = 64 m/s (12 krpm) under three specific loads, $W_{YI}/(LD)$ = 345 kPa, 1,034 and 2,068 kPa. Reprinted/adapted from Ref [27].**

***Experimentally Estimated Stiffnesses for Test Bearing***

Figures 33 and 34 show the direct stiffnesses, ($K_{xx}$, $K_{yy}$), estimated from Re($H$), vs. supplied oil flow rate for operation with shaft speeds equal to 6 krpm and 12 krpm, and under three applied loads. The force coefficients are representative of frequencies to a maximum equal to slightly above the synchronous speed (146 Hz and 215 Hz), respectively. The direct stiffnesses increase with increasing load for operation at both shaft speeds. However, the stiffnesses do not show an increase in magnitude with increasing shaft speed. Appendix B presents a tabulation of the experimental uncertainty in the estimations of the direct stiffnesses, ($K_{xx}$, $K_{yy}$). Uncertainty in $K_{xx}$ ranges from ±1 MN/m to ±4 MN/m. Uncertainty in $K_{yy}$ ranges from ±4 MN/m to ±11 MN/m. The stiffness uncertainty tends slightly higher for operation at 6 krpm shaft speed compared to the uncertainty for operation at 12 krpm.

Additionally, linear correlation of the experimentally measured impedance test data is strong, at least over the excitation frequencies selected to perform the estimations of both stiffnesses and damping, indicating it is reasonable to apply the parameter identification method described in Childs and Hale (1994) [21]. See Appendix A for more detail on the "goodness of fit" of regression lines to the recorded test data.

The bearing direct stiffnesses demonstrate some level of orthotropy at all operating conditions. $K_{xx} > K_{yy}$ for operation at 6 krpm shaft speed and 345 kPa by up to 12%. For all other load conditions for operation at 6 krpm as well as for all load conditions at 12 krpm, $K_{yy} > K_{xx}$, by a range of 2% to 30%. Note that Coghlan [24] also reports bearing direct stiffness orthotropy, $K_{yy} > K_{xx}$ by up to 20%, for a four-pad bearing with smaller radial clearance but of otherwise identical geometry.

Shaft speed does not have a significant effect on either $K_{xx}$ or $K_{yy}$. Similarly, the direct stiffnesses do not show a dependency on flowrates varying from 150% to 25% of the nominal conditions. The stiffnesses increase slightly, for the highest applied load, 2068 kPa, for operation below 25% of the nominal flowrate for both 6 krpm and 12 krpm shaft speed. The small changes in bearing stiffness realized below 25% of the nominal flowrate echo the findings for the bearing eccentricity (see Figures 12 - 15).

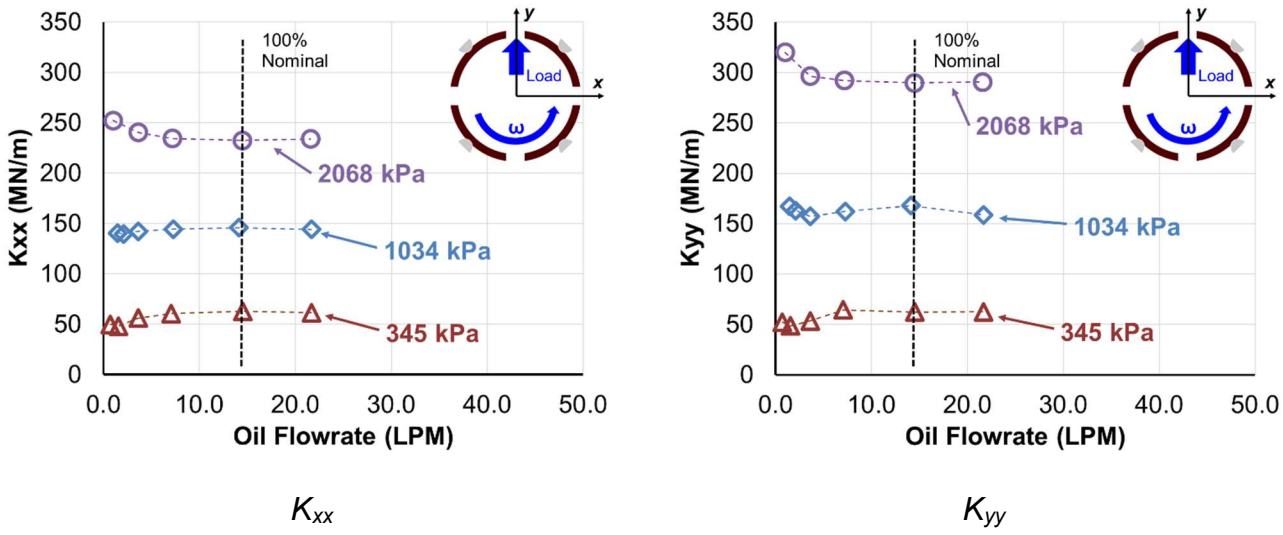


$K_{xx}$ $K_{yy}$

**Figure 33: Bearing direct stiffnesses, $K_{xx}$ (left) and $K_{yy}$ (right), vs. supplied flow rate for operation at surface speed = 32 m/s (6 krpm) and under three specific loads, $W_Y/(LD)$= 345 kPa, 1,034 kPa, and 2,068 kPa. Reprinted/adapted from Ref [27]. Reprinted/adapted from Ref [27].**

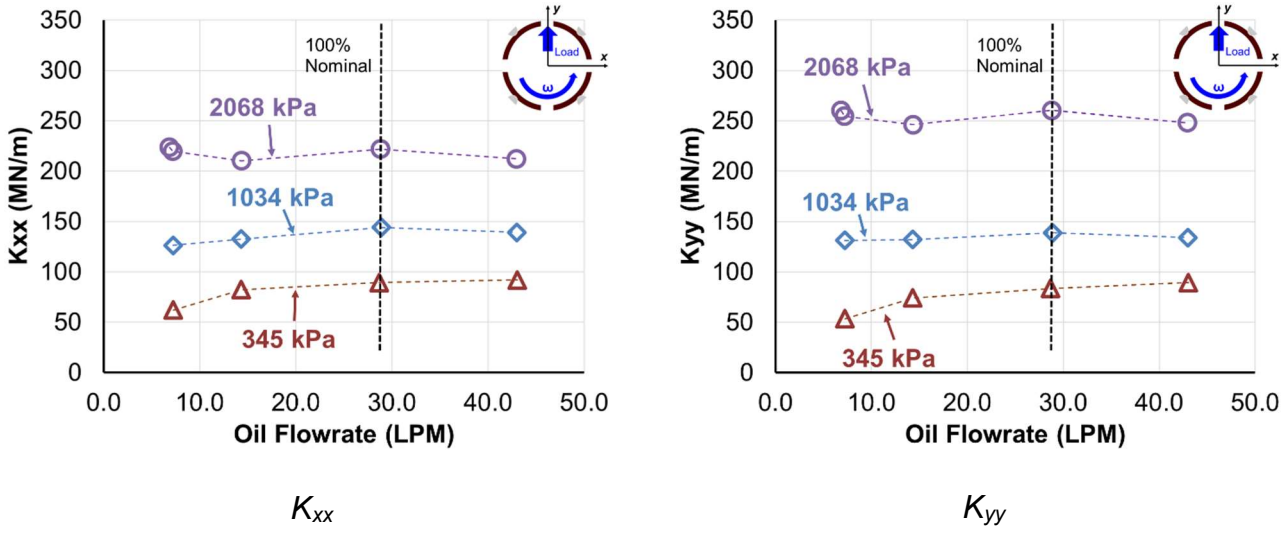


$K_{xx}$ $K_{yy}$

**Figure 34: Bearing direct stiffnesses, $K_{xx}$ (left) and $K_{yy}$ (right), vs. supplied flow rate for operation at surface speed = 64 m/s (12 krpm) and under three specific loads, $W_Y/(LD)$= 345 kPa, 1,034 kPa, and 2,068 kPa. Reprinted/adapted from Ref [27].**

Figure 35 displays the bearing direct stiffnesses, $K_{xx}$, $K_{yy}$, vs. specific load and with oil flowrate between 25% and 150% of the nominal condition. The bearing direct stiffnesses increase

nearly proportionally with an increase in applied load regardless of the supplied oil flowrate. The increase in stiffness is a result of the (expected) reduction in film thickness as load increases (refer to graphs of minimum film thickness vs. supplied flow rate shown in Figures 18 and 19).

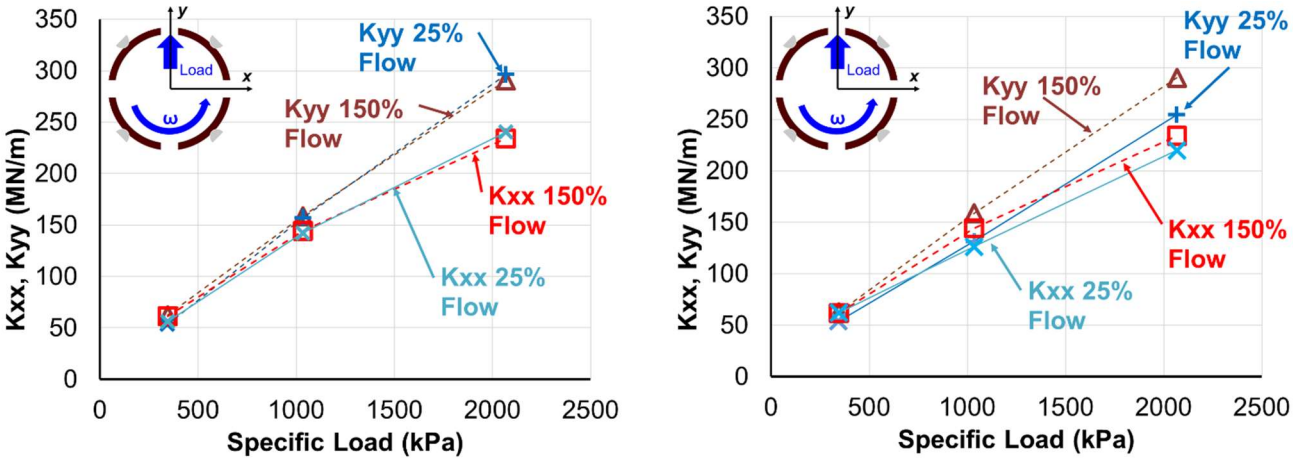


**Figure 35: Bearing direct stiffnesses, $K_{xx}$ and $K_{yy}$, vs. specific load, $W_Y/(LD)$= 345 kPa, 1,034 kPa, and 2,068 kPa, for operation at two shaft surface speeds = 32 m/s at 6 krpm (left) and 64 m/s at 12 krpm (right) and for three oil flow rates, 25%, 100%, and 150% of nominal. Reprinted/adapted from Ref [27].**

Figure 36 depicts the bearing cross-coupled stiffnesses, $K_{xy}$ and $K_{yx}$, vs. flowrate for operation at shaft speed = 6 krpm and 12 krpm, and for three applied loads. Similar to the direct stiffnesses, the magnitudes of the cross-coupled stiffnesses do not show a dependency on oil flowrate. Notice that the magnitude of the cross-coupled stiffnesses is much lower than the corresponding direct stiffness magnitude for the same flowrate and applied specific load, an expected result for a tilting pad journal bearing. Uncertainty in the estimation of $K_{xy}$ is ±1 MN/m to ±5 MN/m, $K_{yx}$ uncertainty is ±5 MN/m to ±12 MN/m.

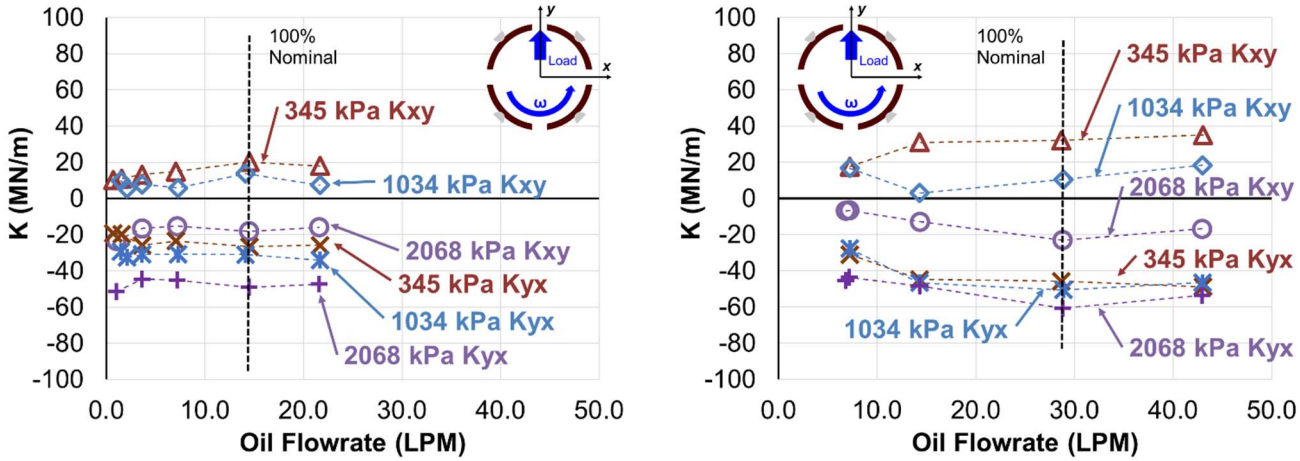


**Figure 36: Bearing cross-coupled stiffnesses, $K_{xy}$ and $K_{yx}$, vs. supplied flow rate for operation at two shaft surface speeds = 32 m/s at 6 krpm (left) and 64 m/s at 12 krpm (right) and under three specific loads, $W_Y/(LD)$=345 kPa, 1,034 kPa, and 2,068 kPa. Reprinted/adapted from Ref [27].**

### *Experimentally Estimated Damping Coefficients for Test Bearing*

Figures 37 and 38 show the bearing direct damping coefficients, $C_{xx}$ and $C_{yy}$, vs. flow rate for operation at 6 krpm and 12 krpm, respectively, and under three static load conditions. A damping force coefficient is derived from a fit of Im($H$) ~ $\omega C$ for frequencies to a maximum $\omega$ =1.46 Ω and 1.07 Ω for 6 krpm and 12 krpm, respectively. Uncertainty in the measurement of $C_{xx}$ and $C_{yy}$ are ±4 kN-s/m to ±14 kN-s/m and ±11 kN-s/m to ±28 kN-s/m, respectively. Although, uncertainty is greater for $C_{yy}$ compared to $C_{xx}$, the results do not otherwise display a clear trend with regard to load or speed.

The direct damping coefficients show a reduction in magnitude for flowrates less than 50% of nominal for operation at the two shaft speeds. The damping is relatively constant or only slightly declining for operation above 50% of the nominal flowrate. However, the reduction in damping is not mirrored by a corresponding increase in stiffness (shown earlier) over the same flowrates. This experimental result contrasts with rationale presented in the literature, for example Nicholas (1994) [4] and He, et al. (2005) [26], indicating a change in operating condition serving to decrease the magnitude of direct damping is expected to couple with an increase in direct stiffness. Coghlan in (2014) [24] finds, experimentally, that an increase in shaft speed lead to an increase in bearing

direct stiffness and an associated reduction in direct damping for an overflooded four-pad LBP bearing of identical geometry but with a reduced radial clearance. Incidentally, San Andrés (2020) [19] shows a decrease in damping, estimated from experimental data, of up to 16% to be associated with only a slight increase in stiffness when flow reduces from 100% to 27% of the nominal flowrate for a five-pad TPJB arranged as LBP in a flooded housing. The results shown in San Andrés [19] and in the present experiment indicate that the aggregate stiffness and damping contributed by a TPJB to a rotor-bearing system, especially under reduced flow conditions, may not follow established trends for bearing operation at least in a flooded end seal arrangement. Additionally, as noted earlier, Zemella, et al. (2020) find that a decrease in damping for a flooded bearing follows when the bearing experiences a sufficient level of film starvation, even without a significant change in estimated stiffness. However, film starvation for the test bearing at reduced flowrates is not known as it is not measured.

Also observe that $C_{yy} = C_{xx}$ for operation at 6 krpm and 345 kPa or 1034 kPa applied load. $C_{yy} > C_{xx}$ for operation at 6 krpm and 2068 kPa applied load. However, $K_{yy} > K_{xx}$ regardless of flow rate or applied load for operation at 6 krpm. Orthotropy in direct stiffness does not correspond to asymmetry in the direct damping coefficients, $C_{yy}$ and $C_{xx}$. Similarly, for all loads and flowrates while operating at 12 krpm, $C_{yy} > C_{xx}$. However, $K_{yy} \approx K_{xx}$ for 345 kPa and 1034 kPa, and $K_{yy}$ is greater than $K_{xx}$ for 2068 kPa load and operation at 12 krpm.

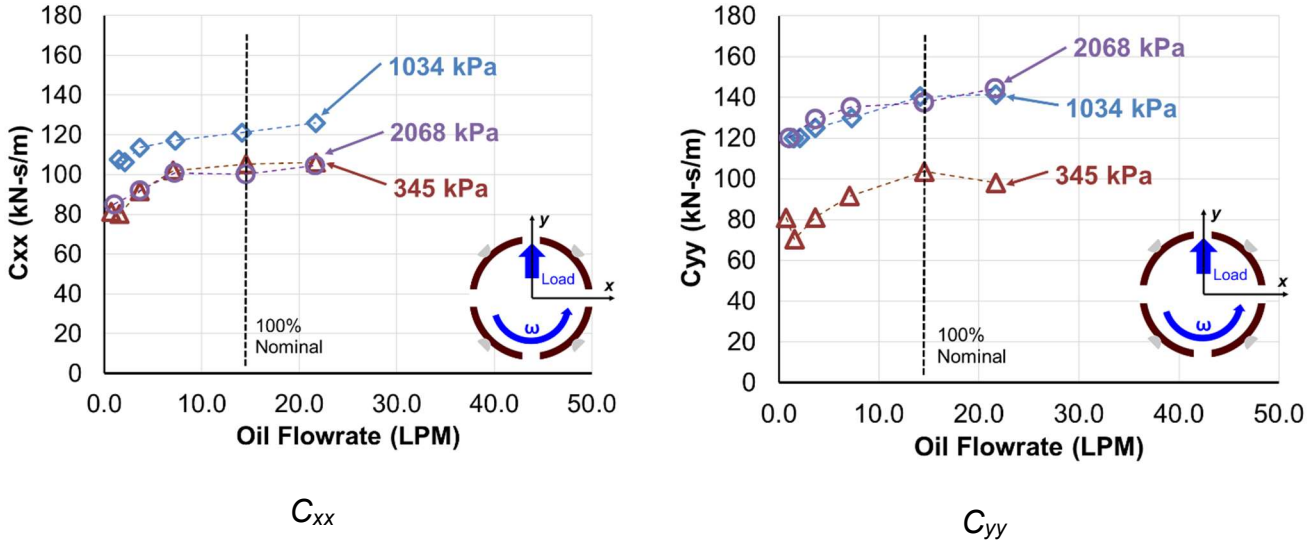


$C_{xx}$ $C_{yy}$

**Figure 37: Bearing direct damping coefficients, $C_{xx}$ (left) and $C_{yy}$ (right), vs. supplied flow rate for operation at surface speed = 32 m/s (6 krpm) and under three specific loads, $W_Y/(LD)$= 345 kPa, 1,034 kPa, and 2,068 kPa. Reprinted/adapted from Ref [27].**

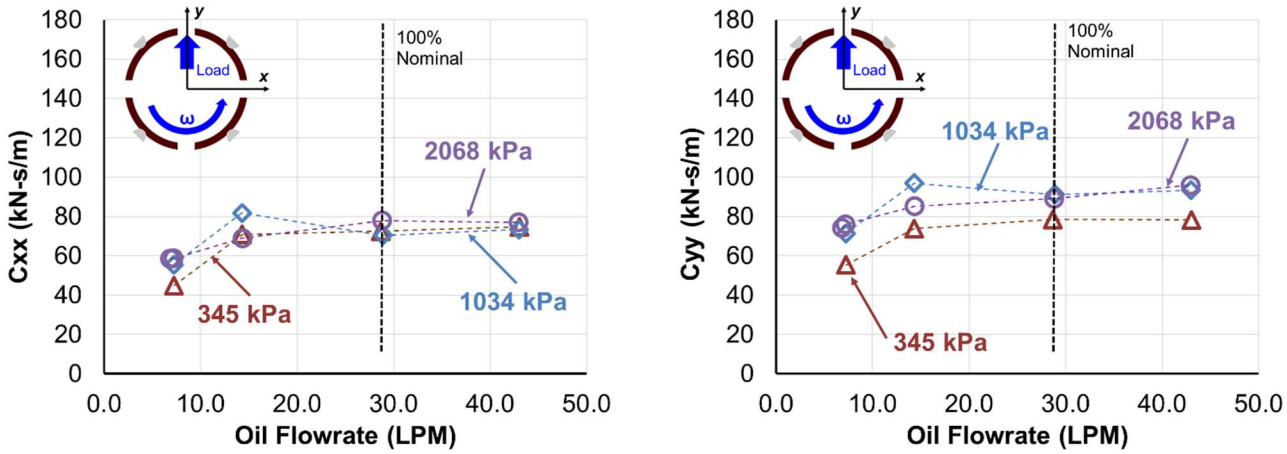


$C_{xx}$ $C_{yy}$

**Figure 38: Bearing direct damping coefficients, $C_{xx}$ (left) and $C_{yy}$ (right), vs. supplied flow rate for operation at surface speed = 64 m/s (12 krpm) and under three specific loads, $W_Y/(LD)$= 345 kPa, 1,034 kPa, and 2,068 kPa. Reprinted/adapted from Ref [27].**

Figure 39 displays the direct damping vs. applied load at two shaft speeds. The graphs show data for three oil flow conditions, ranging from over flooded (150% nominal flow) to starved (25% nominal flow) The damping for 6 krpm is greater than that at 12 krpm and varies little for loads greater than 1034 kPa. At the lowest applied load, 345 kPa, a moderate 14% to 34% reduction in damping is apparent.

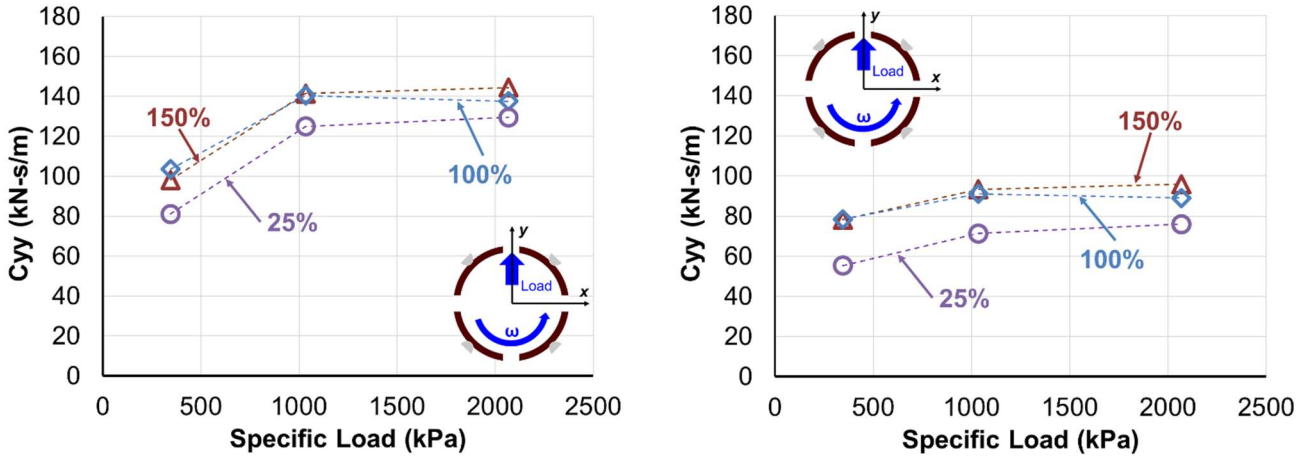


(a) Shaft speed: 6 krpm (b) Shaft speed 12 krpm

**Figure 39: Bearing direct damping coefficients, $C_{yy}$, vs. specific load, $W_Y/(LD)$= 345 kPa, 1,034 kPa, and 2,068 kPa, for operation at two shaft surface speeds = 32 and 64 m/s (6 and 12 krpm), and for oil flow rates 25%, 100% and 150% of nominal. Reprinted/adapted from Ref [27].**

### *Experimentally Estimated Virtual Mass Coefficients for Test Bearing*

Figures 40 and 41 depict the direct virtual mass coefficients $M_{xx}$ and $M_{yy}$ vs. flowrate for shaft speed = 6 krpm and 12 krpm, respectively, and for three applied loads. Uncertainty in the estimation of virtual mass are ±2 kg to ±6 kg for $M_{xx}$ and ±5 kg to ±16 kg for $M_{yy}$. The uncertainty is greater for $M_{yy}$ than $M_{xx}$ and increases slightly with load, at least for $M_{yy}$. The supplied flow rate has a minimal effect on virtual mass for operation above 50% of the nominal. At low flowrates (<50% nominal), the virtual mass approaches zero as the flow rate reduces for operation at 6 krpm. Operation at 12 krpm shaft speed shows a reduction in the magnitude of virtual mass for reducing flowrate for operation below 50% of the nominal flow. Not surprisingly based on the significant curvature of the direct complex stiffnesses with increasing excitation frequency for operation at 12 krpm (shown earlier) vs. the relatively constant direct complex stiffnesses observed for operation at 6 krpm, the magnitudes of the virtual mass coefficients are larger at the higher operating shaft speed.

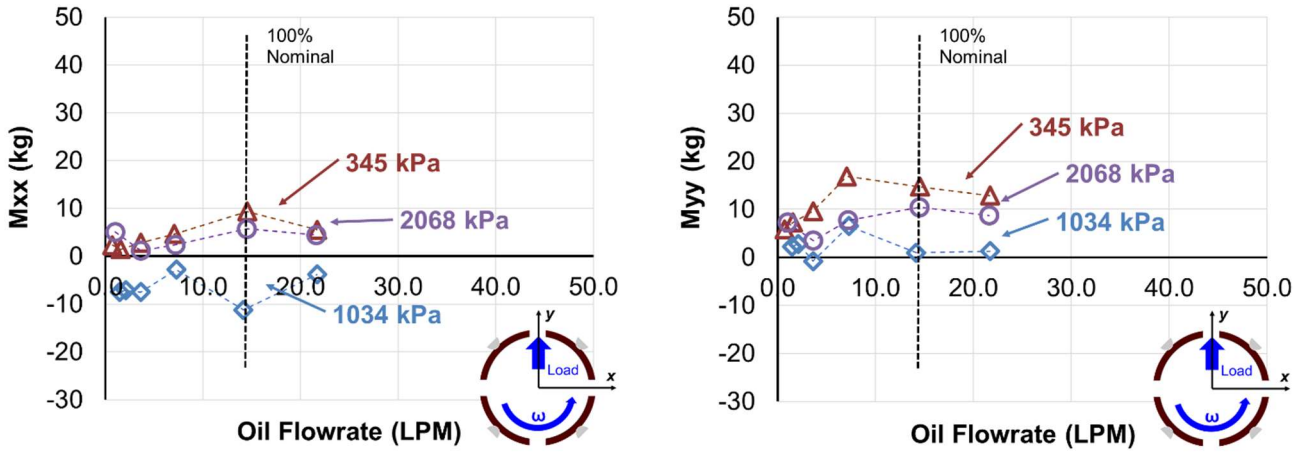


**Figure 40: Direct virtual mass coefficients, $M_{xx}$ (left) and $M_{yy}$ (right), vs. supplied flow rate for operation at surface speed = 32 m/s (6 krpm) and under three specific loads, $W_Y/(LD)$= 345 kPa, 1,034 kPa, and 2,068 kPa.**

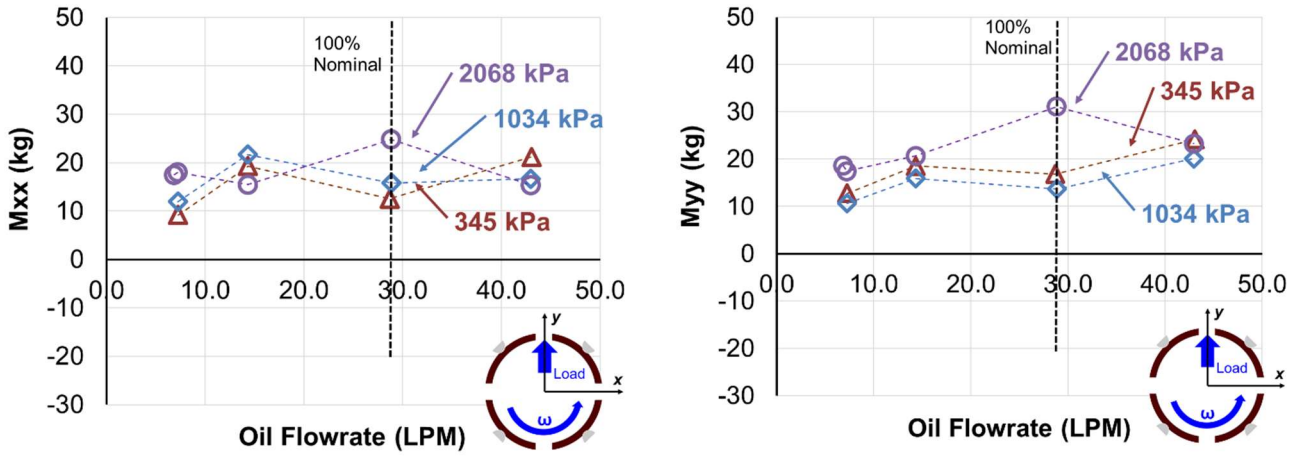


**Figure 41: Direct virtual mass coefficients, $M_{xx}$ (left) and $M_{yy}$ (right), vs. supplied flow rate for operation at surface speed = 64 m/s (12 krpm) and under three specific loads, $W_Y/(LD)$= 345 kPa, 1,034 kPa, and 2,068 kPa.**

Figure 42 shows the direct virtual masses, $M_{xx}$ and $M_{yy}$, vs. applied load for operation at 6 krpm and 12 krpm, respectively, and for 100% nominal flowrate. The virtual mass decreases with decreasing specific load for operation at 12 krpm owing to the decreased effect of fluid inertia as the film thickness increases with reducing load (for a constant 64 m/s shaft surface speed). Virtual mass does not have a dependency on applied load for operation at 6 krpm. However, notice the report of a negative value of $M_{xx}$ for operation at 6 krpm and 1034 kPa applied load. An estimated negative virtual mass signifies the (slight) stiffening of the system with increasing excitation frequency for operation under this flow and load condition, at least over the range of frequencies used to fit the data.

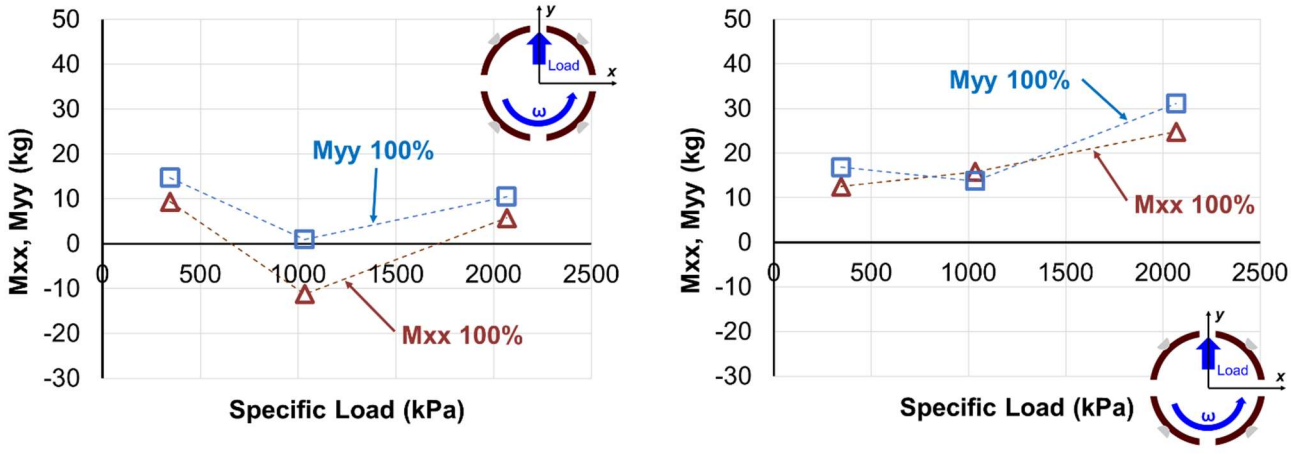


**Figure 42: Direct virtual mass coefficients, $M_{xx}$ and $M_{yy}$, vs. specific load $W_Y/(LD)$, for operation at two shaft surface speeds = 32 and 64 m/s (6 and 12 krpm). Reprinted/adapted from Ref [27].**

# PREDICTION OF BEARING PERFORMANCE

Table 5 provides a summary of physical parameters input to the model described in San Andrés, et al. (2017) [14] to generate predictions for eccentricity, maximum pad metal temperature rise, and bearing dynamic stiffness and damping (presentation following).

**Table 5: Bearing and lubricant parameters for analysis.**

| | |
|---|---|
| ***Bearing*** | |
| Bearing Bore | 101.77 mm |
| Bearing Length | 61 mm |
| Number of Pads | 4 |
| Pivot Type | Spherical |
| Pivot Stiffness | $4.12 \times 10^8$ N/m ([1]) |
| Pivot Offset | 0.50 |
| Pad Arc Length | 72° |
| Bearing Radial Clearance | Refer to Table 4 |
| Pad Preload | 0.30 ([1]) |
| Lubrication Condition | Single orifice B/W Pads |
| Housing Type | Flooded w/end seals |
| Load Orientation | Load Between Pad |
| Analysis Type | Thermo-hydro-dynamic (THD) |
| Thermal Mixing Coefficient | 1 |
| Pad Thermal Conductivity (W/m-°C) | 51.9 W/m-°C ([1]) |
| Pad Mass (kg) | 0.635 kg ([1]) |
| Pad Moment of Inertia About Pivot | $4.6 \times 10^{-4}$ kg-m$^2$ ([1]) |
| Pad Thickness | 0.019 m |
| ***Lubricant*** | |
| Lubricant Type | ISO VG46 |
| Supply Temperature, $T_s$ | 60 °C |
| Viscosity at $T_s$ | 16.4 cP |
| Density at $T_s$ | 837.4 kg/m$^3$ |
| Thermal Conductivity | 0.1227 W/m-°C |
| Viscosity Temperature Coefficient | 0.0369 |
| ([1]) Reference taken from Coghlan [24] | |

Input to the model includes the bearing "hot" radial clearances given in Table 4. The table presents a discrete set of clearances, with each clearance measurement specific to the operating condition listed. Note that the discrete nature of the recorded hot clearances results in some discontinuity in the reported modeling results. The discontinuity is visible as the sharp inflection points in the figure lines reporting the prediction results presented later this section (Figures 43 to 52).

Also note that following on the method and analysis in San Andrés, et al. (2017) [14], the bearing is modeled as a two-pad bearing for very low flows where complete (predicted) cavitation of the unloaded pads would otherwise prevent convergence of a four-pad model. In this case, the two modeled pads represent the loaded pad pair. Utilizing a two-pad model requires adjusting the supply flowrate input to the model by the ratio of flow consumed by the loaded pads to the total bearing supply flow that would be required in a four-pad model. This flow ratio adjustment also results in a discontinuity in the reported modeling results where the model changes from a four-pad to two-pad representation as necessitated by reducing flow.

Figures 43 and 44 show the predicted and experimentally measured bearing eccentricity vs. oil flowrate for operation at 6 krpm and 12 krpm. The predictions agree well with the experimental observations for operation at 6 krpm and for high flowrates (~50% to 150% of nominal flow for 345 kPa and 1034 kPa and 100% to 150% for 2068 kPa). However, for lower flows the predicted eccentricity significantly exceeds the experimentally observed values. Similarly, for operation at 12 krpm, the predictions align well with the experimental data for 50% to 150% flows at 345 kPa load and 100% to 150% flows at 1034 kPa load with the predicted eccentricity exceeding the measured at lower flow rates. However, the model wholly overpredicts the eccentricity for operation at 2068 kPa.

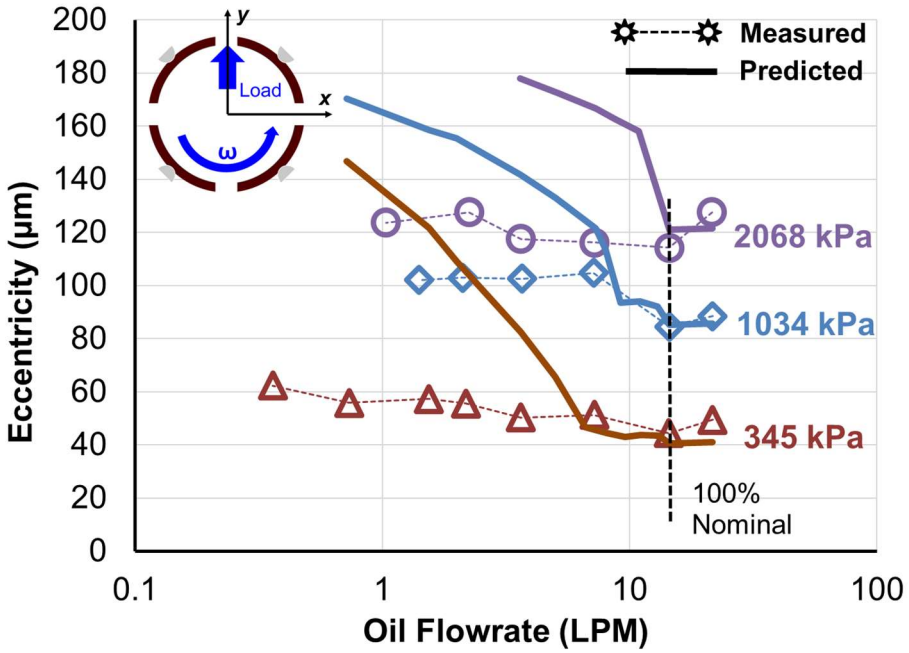


**Figure 43: Bearing eccentricity (*e*) vs. supply flow rate, predicted (solid lines) and measured (symbols), for operation with shaft surface speed = 32 m/s (6 krpm) and under three specific loads, $W_Y/(LD)$= 345 kPa, 1,034 kPa, and 2,068 kPa.**

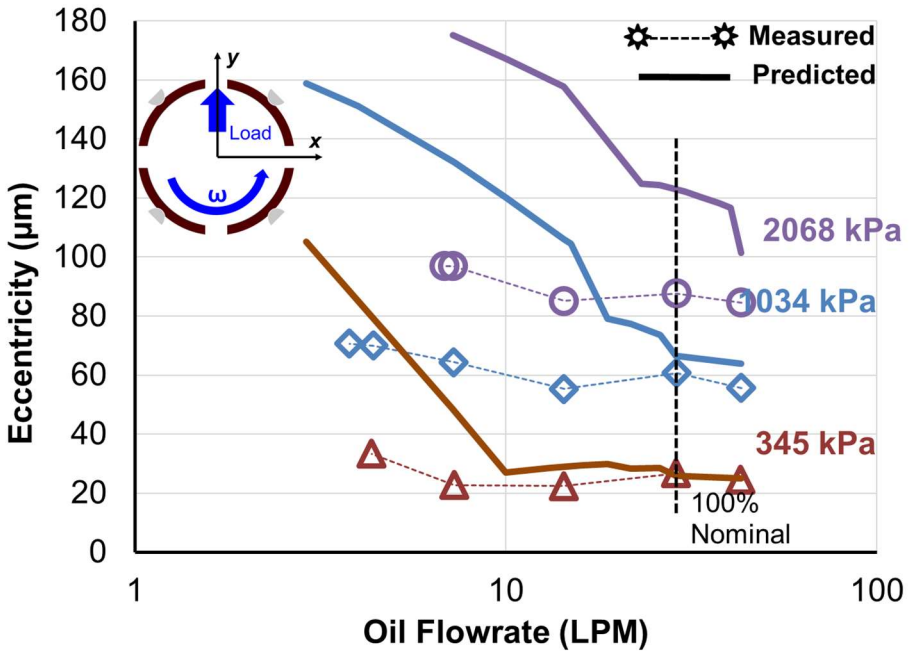


**Figure 44: Bearing eccentricity (*e*) vs. supply flow rate, predicted (solid lines) and measured (symbols), for operation with shaft surface speed = 64 m/s (12 krpm) and under three specific loads, $W_Y/(LD)$= 345 kPa, 1,034 kPa, and 2,068 kPa.**

Note the model is designed to predict the performance of a direct lubricated, evacuated end seals bearing, contrasting with the test bearing flooded arrangement. An evacuated end seals bearing, operating at reduced flow conditions and without the benefit of oil retention offered by the close clearance end seals installed in a flooded bearing arrangement, can experience film starvation resulting in the reduction of film arc length across the pad. Kawashita, et al. experimentally measure such a film length reduction with reducing flowrate in an evacuated bearing arrangement in reference [13]. Indeed, as shown in Figure 45 presenting the predicted film arc length vs. flow rate, the predicted film length reduces compared to the full pad arc (72°) as the flow rate reduces.

Notice that the predicted increase in eccentricity shown earlier in Figures 43 and 44, correlates well with the predicted reduction in the film length. The correlation evidences the model expectation that, as the film length reduces with reducing flowrate and progressing oil starvation, the film thickness also reduces yielding the necessary increase in film pressure needed to support the applied load given the loss in developed film area. For reference, Figure 46 presents predicted maximum film pressure vs. flow rate for operation at both 6 krpm and 12 krpm. The maximum film pressure increase correlates with the reduction in film length and increase in bearing eccentricity. Further, the dramatic difference in predicted vs. measured eccentricity with reducing flow rate, coupled with the correlated predicted film pressure and film length suggest that the test bearing film likely does not suffer from a significant reduction in length, at least for the operating conditions observed. However, the film length and pressure are not measured, so direct comparison of experimental results to the model predictions is not possible.

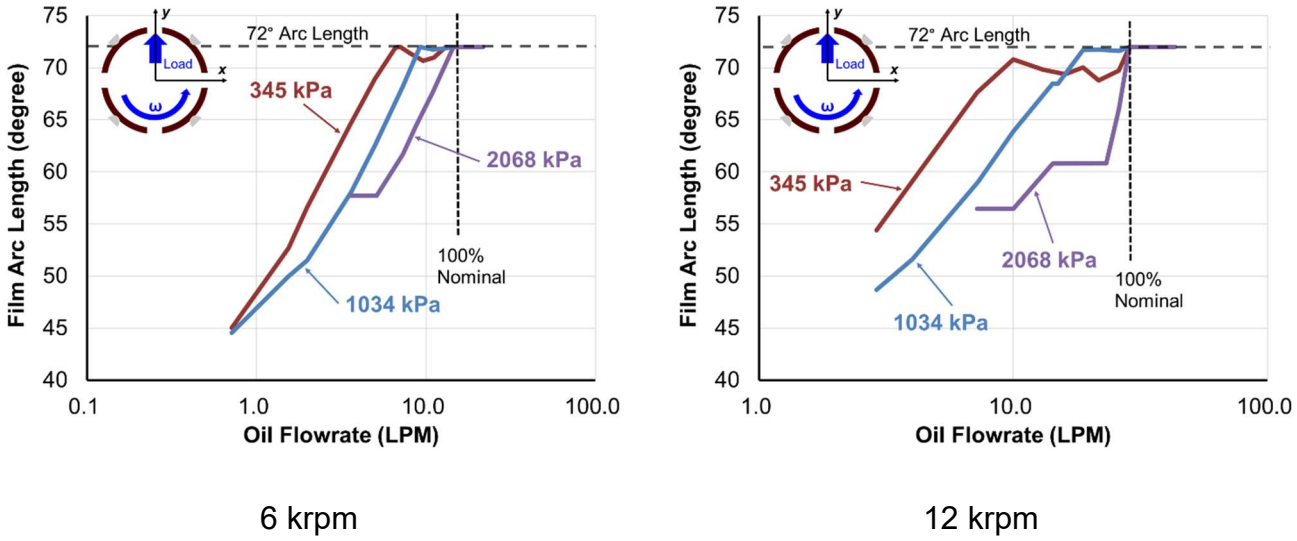


**Figure 45: Predicted film arc length for the loaded pads vs. supplied flow rate for operation at two shaft surface speeds = 32 and 64 m/s (6 and 12 krpm) and under three specific loads, $W_Y/(LD)$= 345 kPa, 1,034 kPa, and 2,068 kPa.**

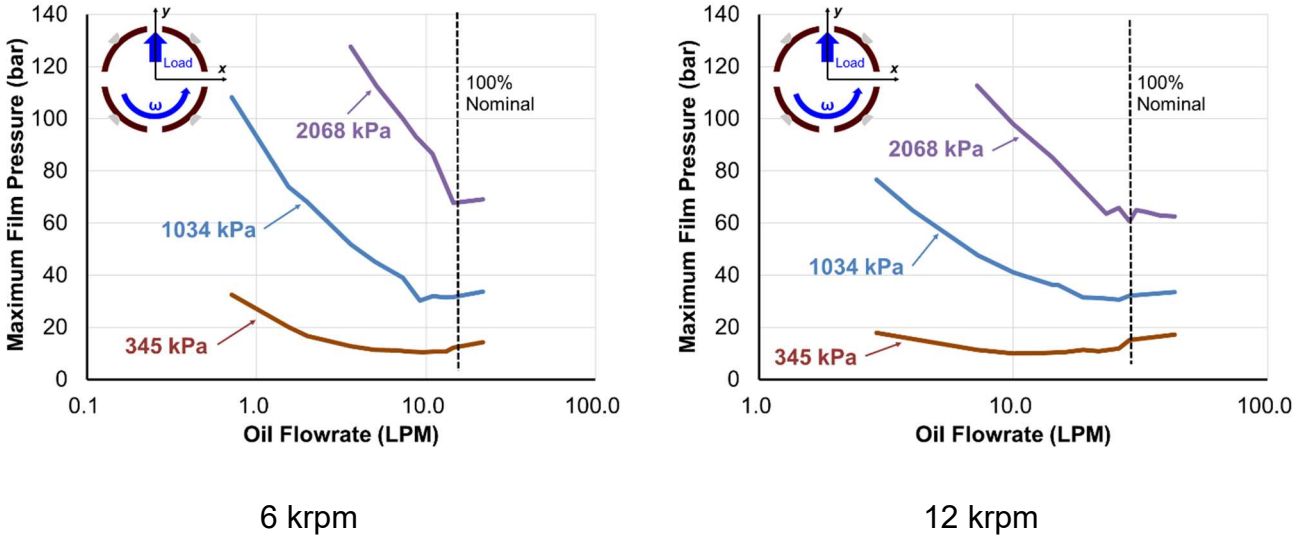


**Figure 46: Predicted maximum film pressure for the loaded pads vs. supplied flow rate for operation at two shaft surface speeds = 32 and 64 m/s (6 and 12 krpm) and under three specific loads, $W_Y/(LD)$= 345 kPa, 1,034 kPa, and 2,068 kPa.**

Figure 47 shows the predicted and experimentally measured maximum pad temperature rise vs. flowrate for operation at surface speeds of 32 m/s and 64 m/s. The model generally underpredicts the experimental results for higher flowrates (> ~50% of the nominal flow). This result is expected as a wealth of experimental results, such as those reported by DeCamillo and Brockwell (2001) [8], Dmochowski and Blair (2006) [9], and Coghlan (2014) [24], have shown

evacuated bearings operate with lower maximum pad temperatures than flooded bearings do for the loaded pads and for otherwise comparable operating conditions. As flow rate reduces below ~25% of the nominal flow, the model correctly predicts a rapid increase in maximum pad temperature rise with further reduction in flowrate.

Interestingly, the model very accurately predicts the pad metal temperature rise at the lowest flowrates for some shaft speed/load combinations and over or underpredicts for others. For example, predicted pad metal temperature rise agrees well with measured values for operation at 6 krpm and 345 kPa for flows less than 25% of the nominal flow. However, for the same flow range (< 25% of the nominal), the model over predicts temperature for operation at 6 krpm and 2068 kPa and underpredicts temperature for operation at 12 krpm and 345 kPa. The exact cause of the inconsistent agreement between predicted and measured values is not known.

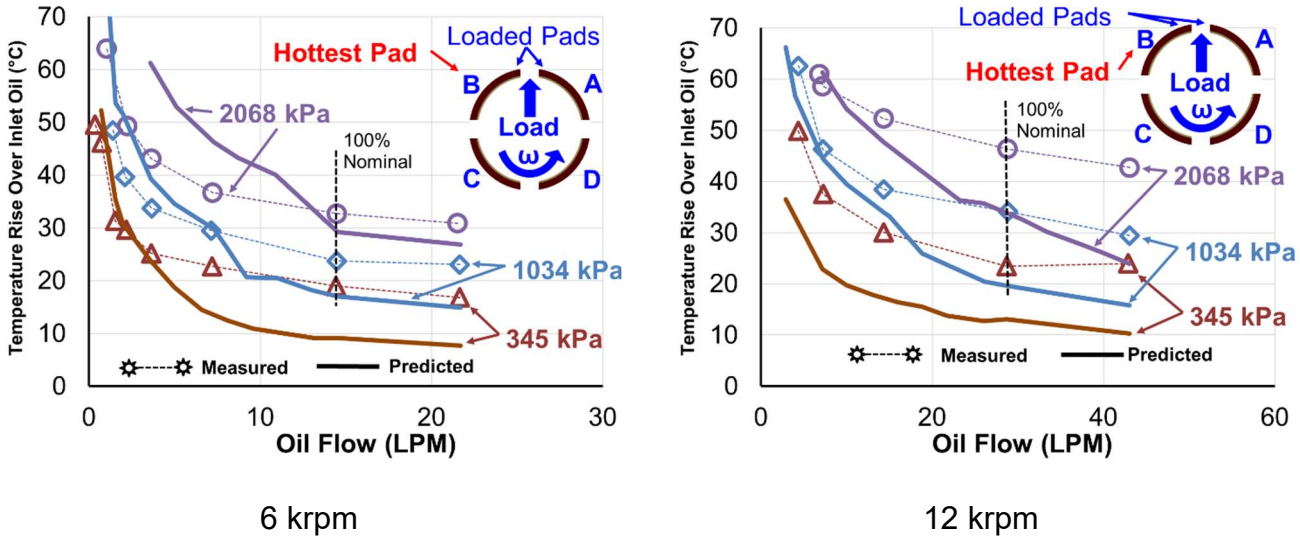


**Figure 47: Pad maximum temperature rise for the loaded pads vs. supplied flow rate, predicted (lines) and measured (symbols), for operation at two shaft surface speeds = 32 and 64 m/s (6 and 12 krpm) and under three specific loads, $W_Y/(LD)$= 345 kPa, 1,034 kPa, and 2,068 kPa. Pad temperature rise relative to oil inlet temperature at 60°C.**

Figure 48 presents predicted and measured power loss for operation at both 32 m/s and 64 m/s (6 and 12 krpm) vs. supply flowrate. At both surface speeds, the bearing consumed significantly more power (1-2x) than predicted across all flowrates and load conditions observed. However, similar to the experimental results, the predictions show a dramatic reduction in power

loss as the flowrate is reduced below 25% of the nominal flowrate. Although the decreasing power loss trend with a decreasing flowrate agrees with the experimentally observed trends, the model expectation of low churning losses owing to an evacuated housing has likely contributed in the underprediction of power consumption at all flowrates, shaft speeds and applied loads.

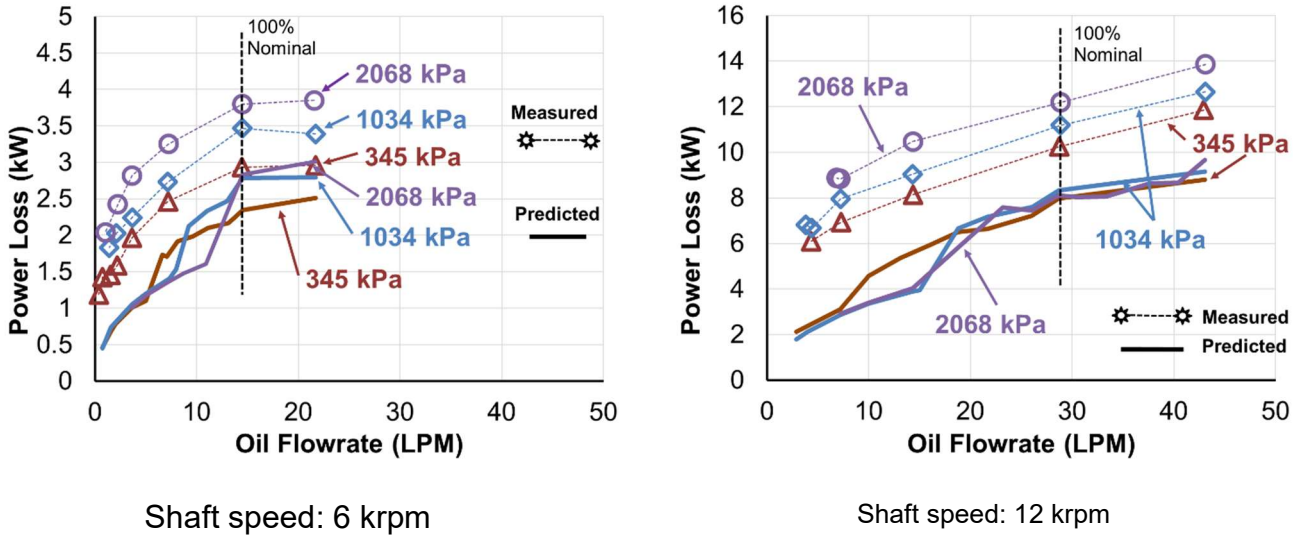


**Figure 48: Bearing power loss vs. supply flow rate, predicted (solid lines) and measured (symbols), for operation at two shaft surface speeds = 32 and 64 m/s (6 and 12 krpm) and under three specific loads, $W_Y/(LD)$= 345 kPa, 1,034 kPa, and 2,068 kPa.**

Figures 49 and 50 present the predicted and experimentally estimated direct stiffness and damping force coefficients vs. oil flow rate for operation at 32 m/s. At the highest flowrates (>100% of nominal for 2068 kPa, > ~75% and 50% of nominal for 1034 kPa and 345 kPa respectively), the predicted and experimentally determined stiffness values in the direction orthogonal to the load agree quite well. The model underpredicts stiffness for 1034 kPa and 2068 kPa applied loads in the *Y*-direction (parallel to the load direction) primarily since the model predicts symmetry between $K_{xx}$ and $K_{yy}$, while the experiment reports $K_{yy} > K_{xx}$ for loads greater than 345 kPa. At flowrates below 25% of the nominal flowrate, the predictions show a sharply increasing direct stiffness not reflected in the experimental results.

Additionally, for flowrates greater than 25% of the nominal, the model underpredicts the experimentally estimated damping coefficients by 50% to 86%, with the discrepancy increasing

for increasing load. The predicted damping decreases sharply and approaches zero as the supplied flow rate approaches zero for operation below 25% of the nominal flow. As noted earlier, the experimentally estimated damping does decrease for decreasing flowrate with a sharper decline below 25% of nominal, but does not decrease as drastically as the predicted values.

The predicted stiffness and damping coefficient values are consistent with the onset of film starvation in an evacuated bearing, specifically the manifestation of a film retreating from the leading edge of the pad resulting in stiffening of the bearing (as discussed earlier). The increased bearing stiffness attenuates the movement of the journal through the film, leading to a reduced damping contribution to the journal-bearing system. The results also highlight the ability of the test bearing flooded arrangement to preserve the magnitude of its stiffness and damping contributions even when operating with only small fractions of the nominal flow rate.

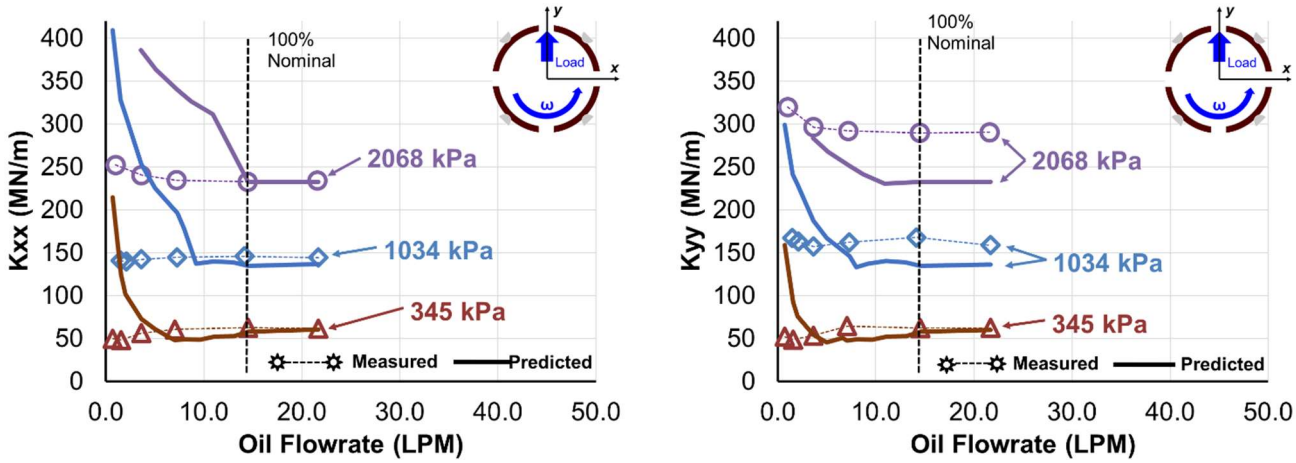


**Figure 49: Bearing direct stiffnesses, $K_{xx}$ (left) and $K_{yy}$ (right), vs. supplied flow rate, predicted (solid lines) and measured (symbols), for operation at surface speed = 32 m/s (6 krpm) and under three specific loads, $W_I/(LD)$= 345 kPa, 1,034 kPa, and 2,068 kPa.**

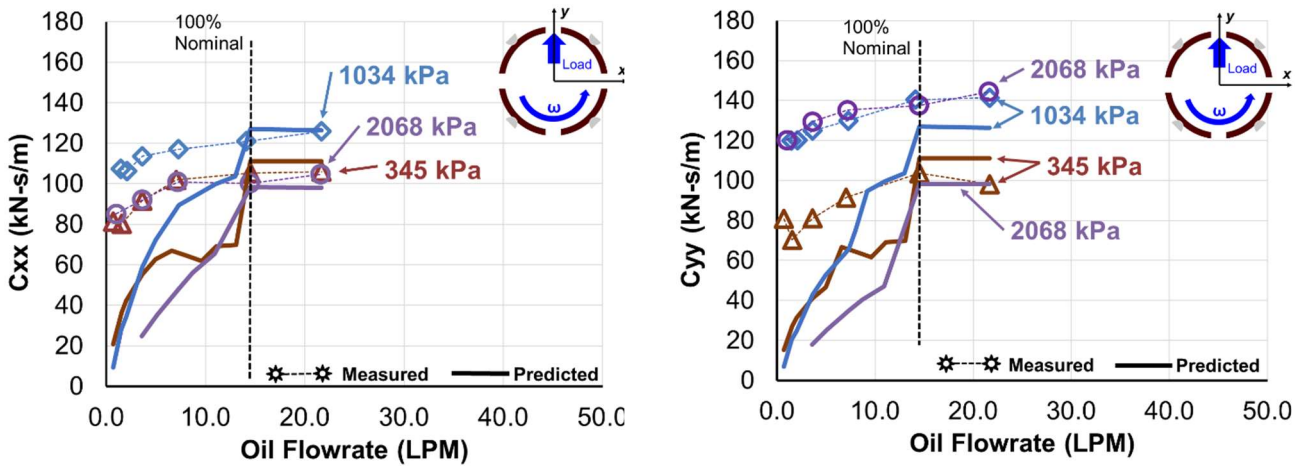


**Figure 50: Bearing direct damping coefficients, $C_{xx}$ (left) and $C_{yy}$ (right), vs. supplied flow rate, predicted (solid lines) and measured (symbols), for operation at surface speed = 32 m/s (6 krpm) and under three specific loads, $W_Y/(LD)$= 345 kPa, 1,034 kPa, and 2,068 kPa.**

Figures 51 and 52 present predicted and experimentally estimated direct stiffness and damping coefficients for operation at 64 m/s surface speed (12 krpm). Similar to operation at 6 krpm, the predicted magnitudes for $K_{xx}$ and $K_{yy}$ agree reasonably well with experiment, especially for high flowrates (>100% of the nominal) with the exception of $K_{yy}$ for operation at 2068 kPa. Also similar to operation at 6 krpm, a sharp increase of the predicted stiffness compared to the experimentally estimated value correlating with a (predicted) retreating film is still apparent. Damping is moderately underpredicted by 1-40% for operation with flows larger than 100% of the nominal. As flow rate reduces below 100%, the magnitude of the underprediction increases dramatically to as much as 60% to 80% less than the experimentally estimated values. The model correctly captures the general trend of decreasing damping with decreasing flowrate, however the model also clearly expects less effective damping across the entire operating range from an evacuated setup than that observed in the experiment.

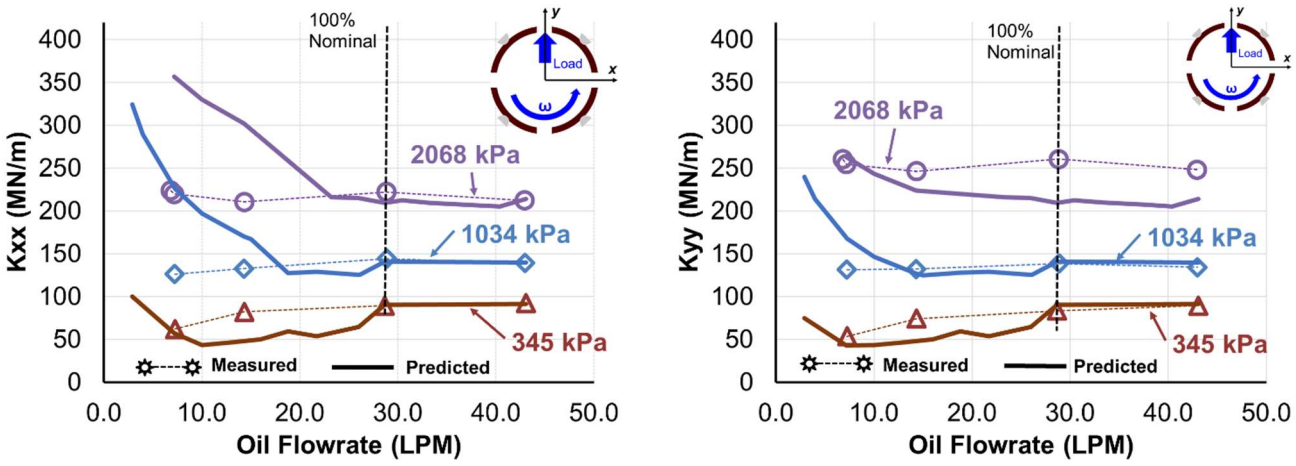


**Figure 51: Bearing direct stiffnesses, $K_{xx}$ (left) and $K_{yy}$ (right), vs. supplied flow rate, predicted (solid lines) and measured (symbols), for operation at surface speed = 64 m/s (12 krpm) and under three specific loads, $W_I/(LD)$= 345 kPa, 1,034 kPa, and 2,068 kPa.**

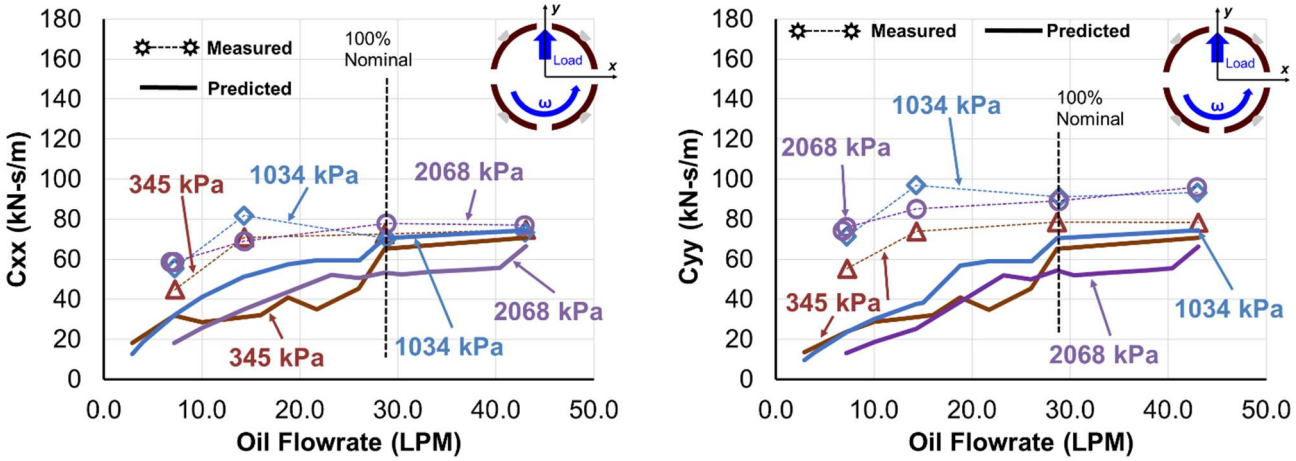


**Figure 52: Bearing direct damping coefficients, $C_{xx}$ (left) and $C_{yy}$ (right), vs. supplied flow rate, predicted (lines) and measured (symbols), for operation at surface speed = 64 m/s (12 krpm) and under three specific loads, $W_I/(LD)$= 345 kPa, 1,034 kPa, and 2,068 kPa.**

# CONCLUSIONS[8]

This thesis quantifies the response of a 4-pad, spherical pivot, 50% offset TPJB with flooded end seals to variation in lubrication flowrate. The bearing performance defined by its change in operating eccentricity, pad metal temperature, power loss, vibration signature and dynamic force coefficients evidences its response to oil flowrates varied from 150% of a nominal value to 25% (or lower) while operating at 32 m/s or 64 m/s and for three specific loads, 345 kPa, 1034 kPa, and 2068 kPa. The experimental results compare to the results from a predictive model designed to account for variation in lubricant flowrate.

- Power loss decreases between 12% and 19% for a 50% reduction in nominal flowrate for operation at 6 krpm and applied specific loads between 345 kPa and 2068 kPa. Power savings of between 13% and 19% are realized for the same 50% reduction in flowrate from the 100% nominal flow for operation at 12 krpm. Power consumption for operation at 12 krpm is 3-4 times the power consumption at 6 krpm for comparative fractions of the nominal flowrate. Power consumption increases roughly proportionally to load at all flowrates and for both operating shaft speeds.
- However, although power consumption is reduced as flowrate decreases, the same 50% reduction in flow results in a 3.7°C to 4°C increase in pad metal temperature rise over inlet oil temperature at 100% nominal flow for operation at 6 krpm and a 5.9°C to 6.6°C increase for operation at 12 krpm. The increase in pad metal temperature rise results in actual pad metal temperatures of 90°C and 112°C for 345 kPa and 2068 kPa, respectively, for operation at 12 krpm. This temperature is likely too warm for long term reliable operation. Flow reduction below 50% does result in additional power savings, however also results in actual pad metal temperatures rapidly approaching the allowable pad metal temperature safety limit. Exceeding the limit puts the bearing at risk for damage due to Babbitt deformation and so is not a desirable operating condition.
- Direct stiffnesses $K_{xx}$ and $K_{yy}$ as well as eccentricity do not show a clear dependency on lubricant flowrate, remaining mostly invariant with reducing flow rate across most of the

[8] Parts of this section reprinted/adapted with permission from Ref [27]

range of flows observed. A modest stiffness increase or decrease depending on applied specific load is apparent at the very lowest flows observed. Cross-coupled stiffnesses remain similarly invariant with flow rate modulation and are much smaller in magnitude than the direct stiffness estimates. The results highlight the ability of the bearing to maintain stiffness even when subjected to very low supply flowrates.

- In contrast to stiffness, damping coefficients change with changing flowrate. Specifically, damping decreases monotonically between 14% and 28% for operation at 6 krpm between the maximum and minimum flows observed. The damping remains nearly constant between 150% and 50% of the nominal flow for operation at 12 krpm, then demonstrates a dramatic decline between 16% and 30% for flows below 50% of the nominal value.
- Broadband subsynchronous vibration emerges at very low flows and, most prevalently, at lightly loaded operating conditions. The amplitude of the vibration, when it did emerge, is low relative to the synchronous vibration amplitude and in no cases resulted in unstable bearing vibration. The results demonstrate the ability of this flooded arrangement to attenuate SSV response, at least over the test conditions observed in this experiment.
- A model designed to account for lubricant flowrate variation in a direct lubricated bearing with evacuated end seals provides predictions for comparison to the experimental results. The predictions for eccentricity, stiffness, and damping compare well with the experimental results for high flowrates (~50% to 100% and above of the nominal flow) with discrepancies between measured and predicted values increasing for reducing flowrate. The model generally underpredicts maximum pad temperature for flowrates greater than 100% of the nominal flow as well as bearing power consumption for all flowrates. The underprediction of pad temperature and power loss (as well as the differences in stiffness, damping, and eccentricity at low flows) likely stem from the predicted reduction in film arc along the pad as lubricant starvation progresses with reducing flowrate.
- Comparisons of the bearing measured performance to the predicted results highlight the ability of the flooded experimental setup to tolerate significant reductions in flowrate without suffering catastrophic losses in direct stiffness or damping and without exceeding allowable pad metal temperature limits.

# REFERENCES


[1] Lund, J., 1964, "Spring and Damping Coefficients for the Tilting Pad Journal Bearing", ASLE Transactions, 7:4, 342-352, DOI: 10.1080/05698196408972064

[2] Lund, J., Orcutt, F., 1967, "Calculations and Experiments on the Unbalance Response of a Flexible Rotor", J. Eng. Ind., **89(4)**, pp. 785–796. https://doi.org/10.1115/1.3610155

[3] Nicholas, J., Gunter, E., and Barret, L., 1978, "The Influence of Tilting Pad Bearing Characteristics on the Stability of High-Speed Rotor Bearing Systems," Topics in Fluid Film Bearings and Optimization, ASME, New York, NY, pp. 55-78.

[4] Nicholas, J., 1994, "Tilting Pad Bearing Design", Proceedings of the 23rd Turbomachinery Symposium, The Turbomachinery Laboratory, Texas A&M University, September 13-15, Dallas, TX, USA, pp. 179-194, https://doi.org/10.21423/R11H2H

[5] Whalen, J., Hess, T., Allen, J., and Craighton, J., 2012, "Babbitted Bearing Health Assessment", 41st Turbomachinery Symposium, The Turbomachinery Laboratory, Texas A&M University, September 24-27, Houston, TX, USA, https://doi.org/10.21423/R1135H

[6] McCloskey, T., 1995, "Troubleshooting Bearing and Lube Oil System Problems" 24th Turbomachinery Symposium, The Turbomachinery Laboratory, Texas A&M University, September 26-28, Houston, TX, USA, pp. 147-166, https://doi.org/10.21423/R1KD3T

[7] Dixon, J. E. and Simmons, S., 1994, "Effect of Load Direction, Preload, Clearance Ratio, and Oil Flow on the Performance of a 200 mm Journal Pad Bearing," Trib. Trans., **37**, pp. 227-336. DOI: 10.1080/10402009408983287

[8] DeCamillo, S. and Brockwell, K., 2001, "A Study of Parameters that Affect Pivoted Shoe Journal Bearing Performance in High-Speed Turbomachinery", Proceedings of the 30th Turbomachinery Symposium, The Turbomachinery Laboratory, Texas A&M University, September 17-20, Houston, TX, USA, pp. 9-22, https://doi.org/10.21423/R1PW8G

[9] Dmochowski, W. M. and Blair, B., 2006, “Effect of Oil Evacuation on the Static and Dynamic Properties of Tilting Pad Journal Bearings”, Trib. Trans., **49**, pp. 536-544. https://doi.org/10.1080/10402000600885175

[10] Tanaka, M., 2000, “Journal Bearing Performance Under Starved Lubrication”, Tribol. Int., **33**, pp. 259-264. https://doi.org/10.1016/S0301-679X(00)00040-2

[11] DeCamillo, S., He, M., Cloud, C. H. and Byrne, J., 2008, “Journal Bearing Vibration and SSV Hash”, Proceedings of the 37th Turbomachinery Symposium, The Turbomachinery Laboratory, Texas A&M University, September 7-11, Houston, TX, USA, pp. 179-194, https://doi.org/10.21423/R1DH1J

[12] Nichols, B., 2017, “Experimental Measurements and Modeling of Tilting-Pad Bearing Performance and System Stability Under Reduced Oil Supply Flow Rates”, Ph.D. dissertation, University of Virginia, Charlottesville, VA, USA.

[13] Kawashita, R., Iwasaki, M., Nishioka, T., Isayama, S., Yokoyama, and S., Waki, Y., 2018, “Study on Subsynchronous Vibration with Tilting Pad Journal Bearing Under Starved Lubrication”, Proceeding of ASME Turbo Expo 2018 Turbomachinery Technical Conference and Exposition, Oslo, Norway, June 11-15, 2018, ASME Paper No. GT2018-75607, pp. V07AT33A014.

[14] San Andrés, L., Koo, B., and Hemmi, M., 2017, "A Flow Starvation Model for Tilting Pad Journal Bearings and Evaluation of Frequency Response Functions: A Contribution Towards Understanding the Onset of Low Frequency Shaft Motions," ASME J. Eng. Gas Turbines Power, **140**(5):052506, https://doi.org/10.1115/1.4038043

[15] Heshmat, H., and Pinkus, O., 1985, “Performance of Starved Journal Bearings with Oil Ring Lubrication”, J. Tribol., **107**(1), pp. 23-31. https://doi.org/10.1115/1.3260998

[16] He, M., Allaire, P., Barrett, L., and Nicholas, J., 2005, “Thermohydrodynamic Modeling of Leading-Edge Groove Bearings under Starvation Condition”, Trib. Trans., **48**, pp. 362-369. DOI: 10.1080/05698190591008531

[17] Booser, E. R., and Missana, A. 1990, “Parasitic Power Losses in Turbine Bearings”, Trib. Trans., **33:3**, pp. 157-162. https://doi.org/10.1080/10402009008981942

[18] Abdollahi, B., and San Andrés, L., 2018, "Improved Estimation of Bearing Pads' Inlet Temperature: A Model for Lubricant Mixing at Oil Feed Ports and Validation against Test Data", ASME J. Tribol., **141**, 031703 (12 pages). https://doi-org.srv-proxy1.library.tamu.edu/10.1115/1.4041720

[19] San Andrés, L., Jani, H., Kaizar, H., and Thorat, M., 2020, "On the Effect of Supplied Flow Rate to the Performance of a Tilting-Pad Journal Bearing – Static Load and Dynamic Force Measurements", Proceedings of ASME Turbo Expo 2020 Turbomachinery Technical Conference and Exposition GT2020, Virtual Conference, Online, September 21-25, 2020, ASME Paper No. GT2020-16215.

[20] Zamella, P., Hagemann, T., Pfau, B., Schwarze, H., 2020 "Identification of Dynamic Coefficients of a Five-Pad Tilting Pad Journal Bearing Up to Highest Surface Speeds", Proceedings of ASME Turbo Expo 2020 Turbomachinery Technical Conference and Exposition GT2020, Virtual Conference, Online, September 21-25, 2020, ASME Paper No. GT2020-14991.

[21] Childs, D. W., and Hale, K., 1994, "A Test Apparatus and Facility to identify the Rotordynamic Coefficients of High-Speed Hydrostatic Bearings," ASME J. Tribol., **116**, pp. 337-343. https://doi.org/10.1115/1.2927226

[22] Rodriguez, L. E., 2004, "Experimental Frequency-Dependent Rotordynamic Coefficients for a Load-On-Pad, High-Speed, Flexible-Pivot Tilting-Pad Bearing," M.S. Thesis, Texas A&M University, College Station, TX, USA.

[23] San Andrés, L., 2009, "Experimental Identification of Bearing Force Coefficients," Modern Lubrication Theory, Notes 14, Libraries Texas A&M University Repository, http://hdl.handle.net/1969.1/93254 [access date Nov. 9, 2019].

[24] Coghlan, D., 2014, "Static, Rotordynamic, and Thermal Characteristics of a Four Pad Spherical-Seat Tilting Pad Journal Bearing with Four Methods of Directed Lubrication", M. S. Thesis, Texas A&M University, College Station, Texas.

[25] Mitsui, J., Hori, Y., Tanaka, M., 1983, "Thermohydrodynamic Analysis of Cooling Effect of Supply Oil in Circular Journal Bearing", J. of Lubrication Tech., 105(3), pp. 414-420, DOI: 10.1115/1.3254629

[26] He, M., Cloud, C. H. and Byrne, J., 2005, "Fundamentals of fluid Film Bearings", Proceedings of the 34th Turbomachinery Symposium, The Turbomachinery Laboratory, Texas A&M University, December 12-15, Houston, TX, USA, pp. 155-176, https://doi.org/10.21423/R14M2G

[27] San Andrés, L., Toner, J. 2020, "Measurement to Quantify the Effect of a Reduced Flow Rate on the Performance of a Tilting Pad Journal Bearing (LBP) with Flooded Ends", TRC-B&C-04-20, Technical Progress Report to the Texas A&M University Turbomachinery Research Consortium, Texas A&M University, College Station, TX.

[28] Illowsky, B., Dean, S., 2018, "Introductory Statistics", OpenStax, Rice University, Houston, TX, Ch. 12.

[29] Ruppert, D., Matteson, D., 2015, "Statistics and Data for Financial Engineering, Second Edition", Springer Science+Business Media LLC New York, NY, Ch. 9.

[30] Taylor, J., 1997, "An Introduction to Error Analysis. The Study of Uncertainties in Physical Measurements", University Science Books, Sausalito, CA, Ch. 3, 8.

# APPENDIX A

# K-C-M CORRELATION COEFFICIENTS

Table 6 presents correlation coefficients giving measure to the "goodness of fit" of the regression lines used to estimate the stiffness and damping coefficients presented earlier. Recall that the zero-frequency intercept of the linear fit of the real part of the complex dynamic stiffness and the slope of the linear fit of the imaginary part yield the estimated stiffness and damping coefficients, respectively. A strong linear correlation of the test data supports utilizing the results of a linear fit to estimate the magnitude of stiffness or damping per the model described in Childs and Hale (1994) [21].

The "*R*" value, or the correlation coefficient, or the Pearson product-moment correlation coefficient, measures the strength of the linear relationship of a set of test data. *R* ranges between (+1) and (-1), with an *R* value approaching (+1) indicating a strong positive correlation, i.e. a strong linear relationship between an increasing independent variable and an *increasing* dependent variable. Conversely, a value approaching (-1) indicates a strong negative correlation, i.e. a strong linear relationship between an increasing dependent variable and a *decreasing* independent variable, Illowsky Dean (2018) [28].

The "$R^2$" value, also known as the coefficient of determination, is the square of the Pearson correlation coefficient, *R,* with a value ranging between 0 and 1. The coefficient of determination quantifies how much of the variation in the independent variable is resultant from the variation of the dependent variable. An $R^2$ value approaching unity indicates most of the variation in the independent variable is due to the change in the dependent variable and that the test data is tightly correlated about a line of best fit, [28]. In this way, $R^2$, following from *R,* is typically taken as a measure of the goodness of fit of the test data to a line produced by performing a linear regression. For example, referring to Table 6, the direct damping coefficients, $C_{xx}$ and $C_{yy}$, demonstrate $R^2$ values approaching 1 indicating the strength of the linear correlation of the test data and confidence in the stated values for damping, at least over the range of excitation frequencies used to produce the fit. The test data for the direct damping coefficients shows a strong increasing trend with increasing excitation frequency.

However, data with little variation in magnitude for an increasing independent variable (i.e. a "flat" or horizontal trend) yield a low $R^2$ value regardless of how well the data is approximated by a linear regression fit. The $Re(H_{xx})$ and $Re(H_{yy})$ data for 6 KRPM shaft speeds, demonstrate such a flat trend when plotted against increasing $\omega^2$, at least over the fit frequency range used to determine their stiffness estimates. The corresponding $R^2$ values for these data sets approach zero (see Table 6), otherwise suggesting a poor linear correlation. However, for these operating conditions, $S_{err}$ or standard error or standard deviation of the residuals, an alternative measure of goodness of fit, provides a more suitable means to judge the adequacy of utilizing a linear model to estimate, in this case, stiffness. $S_{err}$, found as

$$S_{err} = \frac{\sqrt{\Sigma(y_{test} - y_{fit})^2}}{n-2} \qquad (11)$$

with $y_{test}$ equal to the experimentally measured value of complex dynamic stiffness, $y_{fit}$ equal to the complex dynamic stiffness predicted by the fit line, and $n$ equal to the number of sample data values, quantifies the typical error of the data set about a line of best fit (adapted from Ruppert Matteson (2015) [29]). The units of $S_{err}$ are the same as the reported quantity (i.e. MN/m for $K_{ij}$ or kN-s/m for $C_{ij}$). Test data correlation to a linear model increases as $S_{err}$ approaches zero. Notice that the value(s) of $S_{err}$ for the direct stiffnesses, $K_{xx}$ and $K_{yy}$ are low (1-10 MN/m) for operation at 6 KRPM. These magnitudes of $S_{err}$ represent only 1% to 12% of the estimated magnitude of stiffness. The low values of $S_{err}$ evidence the good correlation to a linear model even though the $R^2$ values are low due to near zero slope of the regression line. Recalling that the zero-excitation frequency intercept of the line of best fit of Re($H$) yields an estimate for stiffness, a "flat" fit line reveals a relatively constant stiffness with increasing excitation frequency and the minimal influence of virtual mass. In these cases, provided correlation of the test data with the fit line is good (i.e. low value of Serr), the *K-C-M* model used to estimate the bearing dynamic force coefficients can be simplified by omitting *M*.

The same goodness of fit considerations apply to the cross-coupled stiffness and damping coefficients that also display generally little variance with increasing excitation frequency and therefore yield low $R^2$ values. However, note that the values for $S_{err}$ as a percentage of $K_{ij}$, or in the case of damping, $S_{err}$ as a percentage of the average value of $Im(H_{ij})$, are relatively large compared to the similar fractions of direct stiffness. These larger relative percentages bely the

difficulty in accurately measuring and characterizing the cross-coupled coefficients given their relatively lower magnitude(s) compared to the direct stiffnesses and damping estimates.

**Table 6: Correlation measures for the estimated dynamic force coefficients.**

| Operating Point | | | Freq. Fit Range | Correlation Coefficient | | | | | | | | | | | | | | | | | | | | | | | |
|---|---|---|---|---|---|---|---|---|---|---|---|---|---|---|---|---|---|---|---|---|---|---|---|---|---|---|---|
| Rotor Speed | App. Load | Flowrate | Inclusive | $K_{xx}$ | | | $K_{xy}$ | | | $K_{yx}$ | | | $K_{yy}$ | | | $C_{xx}$ | | | $C_{xy}$ | | | $C_{yx}$ | | | $C_{yy}$ | | |
| (RPM) | (kPa) | (% Nominal) | (Hz) | $R^2$ | $S_{err}$ | $\%K_{ij}$ | $R^2$ | $S_{err}$ | $\%K_{ij}$ | $R^2$ | $S_{err}$ | $\%K_{ij}$ | $R^2$ | $S_{err}$ | $\%K_{ij}$ | $R^2$ | $S_{err}$ | $\%Im\bar{H}_{ij}$ | $R^2$ | $S_{err}$ | $\%Im\bar{H}_{ij}$ | $R^2$ | $S_{err}$ | $\%Im\bar{H}_{ij}$ | $R^2$ | $S_{err}$ | $\%Im\bar{H}_{ij}$ |
| 6000 | 345 | 5 | 0 - 146.5 | 0.2 | 1.1 | 2.3 | 0.0 | 1.3 | 12.6 | 0.4 | 3.2 | 16.4 | 0.5 | 6.2 | 11.8 | 1.0 | 1.9 | 4.8 | 0.8 | 2.7 | 37.0 | 0.1 | 3.8 | 108.1 | 0.9 | 7.9 | 19.1 |
| 6000 | 345 | 10 | 0 - 146.5 | 0.2 | 1.6 | 3.2 | 0.0 | 1.8 | 16.2 | 0.4 | 4.0 | 20.0 | 0.7 | 5.2 | 10.7 | 1.0 | 1.9 | 4.6 | 0.8 | 2.4 | 34.7 | 0.2 | 4.2 | 108.6 | 0.9 | 7.7 | 20.4 |
| 6000 | 345 | 25 | 0 - 146.5 | 0.3 | 1.9 | 3.4 | 0.0 | 1.4 | 11.0 | 0.5 | 3.8 | 14.7 | 0.5 | 5.5 | 10.4 | 1.0 | 1.4 | 3.1 | 0.8 | 2.2 | 31.7 | 0.4 | 4.1 | 142.8 | 0.9 | 9.3 | 19.4 |
| 6000 | 345 | 50 | 0 - 146.5 | 0.2 | 3.6 | 5.9 | 0.5 | 1.7 | 11.6 | 0.4 | 5.3 | 22.6 | 0.6 | 7.9 | 12.3 | 1.0 | 1.5 | 2.7 | 0.7 | 2.6 | 49.2 | 0.5 | 4.5 | 131.1 | 0.9 | 10.7 | 18.8 |
| 6000 | 345 | 100 | 0 - 146.5 | 0.7 | 2.0 | 3.1 | 0.4 | 1.2 | 6.2 | 0.6 | 4.9 | 18.4 | 0.5 | 4.8 | 7.7 | 1.0 | 2.5 | 4.3 | 0.5 | 2.6 | 33.1 | 0.5 | 4.4 | 73.7 | 1.0 | 5.4 | 9.7 |
| 6000 | 345 | 150 | 0 - 146.5 | 0.2 | 3.4 | 5.6 | 0.2 | 1.7 | 9.4 | 0.5 | 5.5 | 21.1 | 0.6 | 7.2 | 11.6 | 1.0 | 1.6 | 2.7 | 0.7 | 2.7 | 42.7 | 0.6 | 4.6 | 100.5 | 0.9 | 8.1 | 13.8 |
| 6000 | 1034 | 10 | 0 - 146.5 | 0.7 | 1.9 | 1.4 | 0.2 | 1.8 | 18.8 | 0.6 | 6.8 | 23.3 | 0.4 | 9.7 | 5.8 | 1.0 | 1.6 | 2.9 | 0.8 | 3.1 | 30.2 | 0.1 | 10.0 | 156.2 | 0.9 | 11.5 | 17.8 |
| 6000 | 1034 | 15 | 0 - 146.5 | 0.7 | 1.8 | 1.3 | 0.0 | 1.3 | 23.0 | 0.6 | 6.3 | 19.4 | 0.4 | 11.0 | 6.8 | 1.0 | 1.8 | 3.2 | 0.8 | 3.3 | 27.9 | 0.1 | 8.7 | 171.6 | 0.9 | 12.8 | 20.3 |
| 6000 | 1034 | 25 | 0 - 146.5 | 0.7 | 2.0 | 1.4 | 0.0 | 1.8 | 22.6 | 0.6 | 7.2 | 198.2 | 0.3 | 9.6 | 6.1 | 1.0 | 2.0 | 3.4 | 0.8 | 3.1 | 24.4 | 0.1 | 7.2 | 198.2 | 0.9 | 11.6 | 16.9 |
| 6000 | 1034 | 50 | 0 - 146.5 | 0.1 | 2.5 | 1.7 | 0.4 | 2.2 | 38.5 | 0.5 | 6.7 | 21.9 | 0.5 | 10.2 | 6.3 | 1.0 | 2.4 | 3.9 | 0.8 | 2.6 | 22.6 | 0.0 | 9.6 | 2327.1 | 0.9 | 13.9 | 20.1 |
| 6000 | 1034 | 100 | 0 - 146.5 | 0.8 | 2.6 | 1.8 | 0.2 | 2.8 | 20.5 | 0.7 | 6.2 | 20.0 | 0.4 | 9.2 | 5.5 | 1.0 | 2.0 | 3.0 | 0.9 | 2.8 | 19.7 | 0.1 | 8.7 | 291.2 | 0.9 | 11.7 | 15.9 |
| 6000 | 1034 | 150 | 0 - 146.5 | 0.4 | 1.9 | 1.3 | 0.1 | 2.8 | 38.0 | 0.6 | 5.6 | 16.6 | 0.4 | 9.0 | 5.7 | 1.0 | 2.0 | 3.1 | 0.9 | 2.1 | 15.5 | 0.1 | 7.9 | 948.8 | 0.9 | 12.1 | 16.5 |
| 6000 | 2068 | 5 | 0 - 146.5 | 0.1 | 2.0 | 0.8 | 0.4 | 2.5 | 10.6 | 0.6 | 6.0 | 11.6 | 0.5 | 9.4 | 2.9 | 1.0 | 2.1 | 4.6 | 0.9 | 3.0 | 22.1 | 0.0 | 9.3 | 714.9 | 0.9 | 9.2 | 13.8 |
| 6000 | 2068 | 25 | 0 - 146.5 | 0.1 | 2.3 | 1.0 | 0.5 | 2.5 | 15.2 | 0.5 | 6.2 | 13.9 | 0.5 | 10.3 | 3.5 | 1.0 | 2.6 | 5.3 | 0.9 | 3.7 | 27.4 | 0.0 | 9.0 | 386.1 | 0.9 | 9.1 | 13.0 |
| 6000 | 2068 | 50 | 0 - 146.5 | 0.0 | 3.0 | 1.3 | 0.8 | 1.9 | 12.1 | 0.5 | 6.3 | 13.9 | 0.6 | 10.7 | 3.7 | 1.0 | 2.7 | 5.1 | 0.9 | 2.4 | 17.7 | 0.0 | 9.2 | 170.8 | 0.9 | 9.6 | 13.2 |
| 6000 | 2068 | 100 | 0 - 146.5 | 0.0 | 2.9 | 1.3 | 0.9 | 1.6 | 8.7 | 0.5 | 5.8 | 11.8 | 0.7 | 8.3 | 2.9 | 1.0 | 2.6 | 4.7 | 0.9 | 2.3 | 16.9 | 0.0 | 8.6 | 183.6 | 0.9 | 9.8 | 13.8 |
| 6000 | 2068 | 150 | 0 - 146.5 | 0.0 | 2.9 | 1.2 | 0.9 | 1.8 | 11.5 | 0.5 | 6.1 | 12.8 | 0.6 | 9.8 | 3.4 | 1.0 | 2.6 | 4.5 | 0.9 | 2.4 | 17.2 | 0.0 | 8.1 | 169.7 | 0.9 | 9.6 | 13.0 |
| 12000 | 345 | 25 | 0 - 214.8 | 0.7 | 5.1 | 8.2 | 0.0 | 3.1 | 17.6 | 0.3 | 9.3 | 30.2 | 0.6 | 6.6 | 12.3 | 0.9 | 7.2 | 18.6 | 0.6 | 5.1 | 74.1 | 0.1 | 7.6 | 225.1 | 0.8 | 9.6 | 23.8 |
| 12000 | 345 | 50 | 0 - 214.8 | 0.8 | 6.7 | 8.2 | 0.0 | 6.2 | 20.0 | 0.4 | 12.5 | 27.9 | 0.4 | 15.1 | 20.4 | 0.9 | 6.7 | 11.8 | 0.3 | 6.2 | 59.8 | 0.5 | 10.1 | 117.5 | 0.8 | 13.0 | 22.4 |
| 12000 | 345 | 100 | 0 - 214.8 | 0.7 | 6.1 | 6.9 | 0.4 | 3.8 | 11.8 | 0.5 | 11.3 | 24.6 | 0.6 | 10.3 | 12.4 | 0.9 | 8.8 | 13.5 | 0.4 | 5.2 | 40.4 | 0.5 | 8.8 | 107.7 | 0.9 | 13.3 | 20.5 |
| 12000 | 345 | 150 | 0 - 214.8 | 0.9 | 5.4 | 5.9 | 0.0 | 4.7 | 13.5 | 0.6 | 11.2 | 22.9 | 0.7 | 12.4 | 13.8 | 0.9 | 8.1 | 12.9 | 0.3 | 6.0 | 53.4 | 0.5 | 8.6 | 113.0 | 0.8 | 17.2 | 27.0 |
| 12000 | 1034 | 25 | 0 - 214.8 | 0.9 | 2.4 | 1.9 | 0.3 | 1.8 | 10.9 | 0.1 | 8.5 | 30.8 | 0.3 | 9.1 | 6.9 | 1.0 | 3.4 | 7.5 | 0.7 | 3.0 | 29.8 | 0.3 | 8.6 | 142.0 | 0.9 | 8.6 | 15.0 |
| 12000 | 1034 | 50 | 0 - 214.8 | 0.9 | 3.8 | 2.9 | 0.2 | 7.0 | 230.1 | 0.4 | 8.0 | 17.3 | 0.3 | 11.5 | 8.7 | 1.0 | 5.8 | 11.0 | 0.8 | 6.1 | 60.5 | 0.0 | 7.6 | 182.6 | 0.9 | 10.8 | 16.5 |
| 12000 | 1034 | 100 | 0 - 214.8 | 0.8 | 4.6 | 3.2 | 0.4 | 3.8 | 36.2 | 0.5 | 6.6 | 13.1 | 0.3 | 10.9 | 7.9 | 1.0 | 4.8 | 7.8 | 0.6 | 5.8 | 28.5 | 0.0 | 8.2 | 633.3 | 0.9 | 11.2 | 15.5 |
| 12000 | 1034 | 150 | 0 - 214.8 | 0.9 | 3.6 | 2.6 | 0.5 | 4.2 | 22.9 | 0.5 | 6.4 | 13.9 | 0.6 | 9.3 | 6.9 | 1.0 | 4.4 | 6.9 | 0.7 | 6.5 | 31.8 | 0.0 | 6.5 | 819.5 | 0.9 | 9.9 | 13.6 |
| 12000 | 2068 | 25 | 0 - 214.8 | 1.0 | 2.0 | 0.9 | 0.6 | 2.3 | 36.0 | 0.4 | 7.8 | 17.8 | 0.5 | 9.9 | 3.9 | 1.0 | 2.1 | 4.5 | 0.7 | 3.1 | 26.2 | 0.1 | 8.6 | 884.2 | 0.9 | 10.7 | 16.2 |
| 12000 | 2068 | 50 | 0 - 214.8 | 0.9 | 2.2 | 1.1 | 0.8 | 2.3 | 18.3 | 0.3 | 8.7 | 17.9 | 0.4 | 12.7 | 5.2 | 1.0 | 2.8 | 5.1 | 0.8 | 2.6 | 21.3 | 0.1 | 9.2 | 773.2 | 0.9 | 9.6 | 13.7 |
| 12000 | 2068 | 100 | 0 - 214.8 | 0.9 | 5.8 | 2.6 | 0.7 | 5.7 | 24.8 | 0.3 | 15.4 | 25.3 | 0.5 | 15.5 | 6.0 | 1.0 | 5.2 | 9.6 | 0.8 | 4.6 | 38.4 | 0.1 | 11.1 | 5389.1 | 0.9 | 15.2 | 22.2 |
| 12000 | 2068 | 150 | 0 - 214.8 | 0.8 | 5.2 | 2.4 | 0.7 | 2.8 | 16.5 | 0.4 | 7.6 | 14.2 | 0.5 | 12.0 | 4.8 | 1.0 | 6.1 | 10.9 | 0.8 | 4.3 | 34.1 | 0.2 | 10.0 | 1317.0 | 1.0 | 8.5 | 12.0 |

# APPENDIX B

# UNCERTAINTY ANALYSIS

Table 7 lists the instrument measurement uncertainties.

**Table 7: Instrument measurement uncertainties.**

| Quantity Measured | Instrument Type | Measurement Uncertainty (unit) |
|---|---|---|
| Displacement | Eddy-current type proximity probe | ±2.5 (μm) |
| Shaft Speed | Eddy current type proximity probe and tachometer arrangement | ±5 (rpm) |
| Torque | Strain-gauge sensor integral to coupling | ±0.1 (Nm) |
| Pad and Oil Temperature | J-type Thermocouple | ±0.5 (°C) |
| Force: Dynamic | Strain gauge load cell | ±2 (N) |
| Force: Static | Piezoelectric load cell | ±2 (kN) |
| Acceleration | Piezoelectric accelerometer | ±0.01 (g) |

### *Uncertainty in Bearing Eccentricity*

The measured bearing eccentricity, $e$, results from subtracting the measured bearing center, in component form, from the measured operating position. The eddy-current sensor measurement uncertainty listed in Table 7 propagates through the position measurements and eccentricity calculation, following from the equations in Taylor (1997) [30] to determine the uncertainty in bearing eccentricity, $\delta_{eccentricity}$, as

$$\delta_{eccentricity} = |e| \left( \frac{\delta_{e_x}}{e_x} + \frac{\delta_{e_y}}{e_y} \right) \Big/ \left| {e_x}^2 + {e_y}^2 \right| \qquad \text{B.1}$$

Table 8 presents the eccentricity measurements with uncertainties.

**Table 8: Operating bearing eccentricities and uncertainties.**

| Operating Point | | | Eccentricity | |
|---|---|---|---|---|
| Rotor Speed (RPM) | App. Load (kPa) | Flowrate (% Nominal) | (μm ) | (±μm ) |
| 6000 | 345 | 2 | 62.3 | 4.9 |
| 6000 | 345 | 5 | 55.9 | 4.6 |
| 6000 | 345 | 10 | 57.3 | 4.5 |
| 6000 | 345 | 15 | 55.5 | 5.0 |
| 6000 | 345 | 25 | 50.2 | 4.5 |
| 6000 | 345 | 50 | 51.2 | 4.6 |
| 6000 | 345 | 100 | 44.3 | 4.7 |
| 6000 | 345 | 150 | 49.5 | 4.4 |
| 6000 | 1034 | 10 | 102.1 | 4.7 |
| 6000 | 1034 | 15 | 102.9 | 4.4 |
| 6000 | 1034 | 25 | 102.6 | 4.5 |
| 6000 | 1034 | 50 | 104.8 | 4.7 |
| 6000 | 1034 | 100 | 84.6 | 4.5 |
| 6000 | 1034 | 150 | 88.4 | 4.4 |
| 6000 | 2068 | 5 | 123.6 | 4.6 |
| 6000 | 2068 | 10 | 127.6 | 4.4 |
| 6000 | 2068 | 25 | 117.5 | 4.5 |
| 6000 | 2068 | 50 | 116.2 | 4.3 |
| 6000 | 2068 | 100 | 114.2 | 4.5 |
| 6000 | 2068 | 150 | 127.5 | 4.6 |
| 12000 | 345 | 15 | 33.3 | 6.1 |
| 12000 | 345 | 25 | 22.7 | 6.0 |
| 12000 | 345 | 50 | 22.5 | 5.3 |
| 12000 | 345 | 100 | 26.7 | 5.5 |
| 12000 | 345 | 150 | 24.7 | 4.4 |
| 12000 | 1034 | 13 | 70.6 | 5.4 |
| 12000 | 1034 | 15 | 70.0 | 5.3 |
| 12000 | 1034 | 25 | 64.3 | 4.8 |
| 12000 | 1034 | 50 | 55.3 | 4.6 |
| 12000 | 1034 | 100 | 60.8 | 4.5 |
| 12000 | 1034 | 150 | 55.7 | 4.6 |
| 12000 | 2068 | 23 | 97.0 | 4.7 |
| 12000 | 2068 | 25 | 97.0 | 4.6 |
| 12000 | 2068 | 50 | 85.1 | 4.6 |
| 12000 | 2068 | 100 | 87.7 | 4.4 |
| 12000 | 2068 | 150 | 84.6 | 4.3 |

***Uncertainty in Pad Metal and Oil Temperatures***

Type-J thermocouples measure the pad metal and oil temperatures. The reported thermocouple uncertainty, $\delta_{thermocouple}$ = ±0.5 (°C), applies directly to those measurements. 'Pad metal temperature rise' is the measured D annulus oil temperature subtracted from the measured pad metal temperature. The uncertainty for pad metal temperature rise results from the combined uncertainty of the oil and pad metal temperature thermocouple uncertainty.

$$\delta_{pad\ metal\ temperature\ rise} = \sqrt{\delta_{thermocouple,\ \ pad\ metal}{}^2 + \delta_{thermocouple,\ \ oil}{}^2} = \pm 0.7\ °\mathrm{C} \qquad \text{B.2}$$

***Uncertainty in Power***

The torque meter and tachometer measure the shaft drag torque and speed, respectively. The fractional uncertainties of the torque and speed sensor combine in quadrature to determine the uncertainty in reported bearing power consumption.

$$\delta_{power} = |P_{measured}|\sqrt{\left(\frac{\delta_\tau}{\tau_{measured}}\right)^2 + \left(\frac{\delta_\Omega}{\Omega_{measured}}\right)^2} \qquad \text{B.3}$$

The uncertainty in the power calculations are small compared to the magnitude of the measured power consumption, ranging from 62 W to 66 W and 125 to 126W for operation at 6 krpm and 12 krpm respectively.

***Uncertainty in Dynamic Force Coefficients***

The instrument uncertainties in the bearing to shaft displacement, bearing housing acceleration, and applied dynamic excitation force measurements propagate into the determination of $H_{ij}$ for each excitation frequency. The fractional uncertainties combine in quadrature to determine the bias uncertainty, $\delta_{H_{ij},measurement}$, for each measurement of $H_{ij}$.

$$\delta_{H_{ij},measurement} = \left|H_{ij}\right|\sqrt{\left(\frac{\delta_d}{d_{measured}}\right)^2 + \left(\frac{\delta_a}{a_{measured}}\right)^2 + \left(\frac{\delta_f}{f_{measured}}\right)^2} \qquad \text{B.4}$$

Where $d$ = displacement, $a$ = acceleration, and $f$ = force.

The test rig's dynamic excitation algorithm performs a multifrequency excitation, shaking the bearing with ten trials, each trial including components of 34 discrete frequencies from zero to 341.8 Hz. (Note, however that a smaller subset of these frequencies is ultimately used later for the linear fits determining *K*, *C*, and *M*). The results of the 10 trials produce an average $H_{ij}$ for each excitation frequency (with '$H_{ij}$' denoting the average of the ten '$h_{ij}$'s' constituting the set of each trial). This averaging induces a precision uncertainty, $\delta_{H_{ij}}$, in the determination of each $H_{ij}$ resulting from the variability the set of trials.

$$\delta_{H_{ij,variability}} = 1.96\sqrt{\frac{1}{N-1}\sum\left(h_{ij} - H_{ij}\right)^2} \qquad \text{B.5}$$

Where N = 10 trials and $h_{ij}$ is the result of a particular trial.

The instrument (bias) and precision uncertainties combine to yield a total uncertainty for each Hij with respect to excitation frequency.

$$\delta_{H_{ij,total}} = \sqrt{\delta_{H_{ij,measurement}} + \delta_{H_{ij,variability}}} \qquad \text{B.6}$$

For clarity the subscript '$H_{ij,total}$' is replaced with '$H_{ij}$' and represents the combined uncertainty in impedance measurement resulting from the instrument bias error and the variability of the distribution of averaged values for $h_{ij}$ resulting from each shake trial.

Additionally, as each set of impedances yields a frequency independent estimate of K, C, and M from extraction of the slope and/or zero excitation frequency intercept of a regression line calculated using the $H_{ij}$ vs. $\omega$ or $\omega^2$ results, the uncertainty in the determination of each of the $H_{ij}$'s contributes to the uncertainty of these fit parameters (slope and intercept). Recall that the "*Y*" or zero excitation frequency intercept of the line of best fit of the real part of the impedance vs. $\omega^2$ determines the stiffness coefficient. The slope of this line determines the virtual mass. Here the use of '$\omega^2$' instead of '$\omega$' facilitates the use of linear regression (instead of higher order) to estimate the values for *K* and *M*. The slope of the imaginary part of the impedance vs. $\omega$ determines the damping coefficient. Following from the equations for uncertainty in slope and intercept given in Taylor (1997) [30], let A and B be the slope and intercept of an arbitrary best fit line.

$$y = Ax + B \qquad \text{B.7}$$

The uncertainties in the slope, A, and intercept, B, are given by

$$\delta_A = \sqrt{\frac{\sum \frac{1}{\delta_{H_{ij}}{}^2}(\omega \text{ or } \omega^2)^2}{\sum \frac{1}{\delta_{H_{ij}}{}^2}\sum \frac{1}{\delta_{H_{ij}}{}^2}(\omega \text{ or } \omega^2)^2 - \left(\sum \frac{1}{\delta_{H_{ij}}{}^2}(\omega \text{ or } \omega^2)\right)^2}} \quad \text{B.8}$$

$$\delta_B = \sqrt{\frac{\sum \frac{1}{\delta_{H_{ij}}{}^2}}{\sum \frac{1}{\delta_{H_{ij}}{}^2}\sum \frac{1}{\delta_{H_{ij}}{}^2}(\omega \text{ or } \omega^2)^2 - \left(\sum \frac{1}{\delta_{H_{ij}}{}^2}(\omega \text{ or } \omega^2)\right)^2}} \quad \text{B.9}$$

With the values for slope and intercept resulting from the fits found using the set of $H_{ij}$'s with individual uncertainties described in equation B.6.

Table 9 gives the uncertainty in the estimate of the direct dynamic force coefficients. Table 10 gives the uncertainty in the cross-coupled dynamic force coefficients.

**Table 9: Direct dynamic force coefficients and uncertainty.**

| Operating Condition | | | Direct Dynamic Force Coefficient and Uncertainty | | | | | | | | | | | |
|---|---|---|---|---|---|---|---|---|---|---|---|---|---|---|
| Rotor Speed (RPM) | App. Load (kPa) | Flowrate (% Nominal) | $K_{xx}$ (MN/m) | $\pm\delta_{Kxx}$ (MN/m) | $K_{yy}$ (MN/m) | $\pm\delta_{Kyy}$ (MN/m) | $C_{xx}$ (kN-s/m) | $\pm\delta_{Cxx}$ (kN-s/m) | $C_{yy}$ (kN-s/m) | $\pm\delta_{Cyy}$ (kN-s/m) | $M_{xx}$ (kg) | $\pm\delta_{Mxx}$ (kg) | $M_{yy}$ (kg) | $\pm\delta_{Myy}$ (kg) |
| 6000 | 345 | 5 | 50 | 2 | 52 | 6 | 81 | 7 | 81 | 13 | 2 | 2 | 6 | 8 |
| 6000 | 345 | 10 | 48 | 2 | 49 | 5 | 80 | 8 | 70 | 13 | 1 | 3 | 7 | 7 |
| 6000 | 345 | 25 | 56 | 2 | 53 | 6 | 92 | 8 | 81 | 18 | 3 | 3 | 10 | 9 |
| 6000 | 345 | 50 | 61 | 3 | 64 | 7 | 102 | 10 | 92 | 28 | 5 | 4 | 17 | 10 |
| 6000 | 345 | 100 | 63 | 4 | 62 | 5 | 105 | 14 | 104 | 13 | 9 | 6 | 15 | 7 |
| 6000 | 345 | 150 | 61 | 3 | 62 | 7 | 106 | 12 | 98 | 19 | 6 | 5 | 13 | 10 |
| 6000 | 1034 | 10 | 141 | 2 | 167 | 8 | 107 | 10 | 120 | 17 | -7 | 2 | 2 | 12 |
| 6000 | 1034 | 15 | 140 | 1 | 163 | 10 | 106 | 9 | 120 | 18 | -7 | 2 | 3 | 13 |
| 6000 | 1034 | 25 | 142 | 2 | 157 | 8 | 114 | 10 | 125 | 17 | -7 | 2 | -1 | 11 |
| 6000 | 1034 | 50 | 144 | 2 | 162 | 9 | 117 | 10 | 130 | 19 | -3 | 3 | 7 | 12 |
| 6000 | 1034 | 100 | 146 | 3 | 168 | 8 | 121 | 14 | 140 | 17 | -11 | 4 | 1 | 12 |
| 6000 | 1034 | 150 | 144 | 2 | 159 | 8 | 126 | 10 | 141 | 17 | -4 | 2 | 1 | 11 |
| 6000 | 2068 | 5 | 252 | 2 | 320 | 8 | 85 | 8 | 120 | 14 | 5 | 2 | 7 | 12 |
| 6000 | 2068 | 25 | 240 | 2 | 296 | 9 | 92 | 9 | 129 | 14 | 1 | 3 | 3 | 13 |
| 6000 | 2068 | 50 | 234 | 2 | 292 | 10 | 101 | 8 | 135 | 14 | 2 | 3 | 8 | 14 |
| 6000 | 2068 | 100 | 233 | 2 | 290 | 8 | 100 | 11 | 138 | 13 | 6 | 3 | 10 | 11 |
| 6000 | 2068 | 150 | 234 | 2 | 290 | 9 | 105 | 11 | 144 | 13 | 4 | 3 | 9 | 13 |
| 12000 | 345 | 25 | 62 | 3 | 54 | 4 | 45 | 11 | 55 | 12 | 9 | 4 | 13 | 5 |
| 12000 | 345 | 50 | 82 | 4 | 74 | 8 | 71 | 9 | 74 | 15 | 19 | 6 | 19 | 11 |
| 12000 | 345 | 100 | 89 | 3 | 83 | 5 | 73 | 13 | 78 | 15 | 13 | 4 | 17 | 7 |
| 12000 | 345 | 150 | 92 | 3 | 89 | 7 | 75 | 12 | 78 | 20 | 21 | 4 | 24 | 10 |
| 12000 | 1034 | 25 | 126 | 1 | 131 | 6 | 56 | 5 | 71 | 12 | 12 | 2 | 11 | 9 |
| 12000 | 1034 | 50 | 133 | 3 | 132 | 8 | 82 | 9 | 97 | 15 | 22 | 4 | 16 | 11 |
| 12000 | 1034 | 100 | 144 | 3 | 139 | 8 | 70 | 10 | 91 | 15 | 16 | 4 | 14 | 11 |
| 12000 | 1034 | 150 | 139 | 2 | 134 | 7 | 73 | 9 | 93 | 14 | 17 | 3 | 20 | 9 |
| 12000 | 2068 | 25 | 220 | 1 | 255 | 7 | 59 | 4 | 76 | 17 | 18 | 2 | 17 | 10 |
| 12000 | 2068 | 50 | 210 | 2 | 246 | 9 | 69 | 5 | 85 | 15 | 15 | 2 | 21 | 13 |
| 12000 | 2068 | 100 | 222 | 4 | 260 | 11 | 78 | 7 | 89 | 21 | 25 | 6 | 31 | 16 |
| 12000 | 2068 | 150 | 212 | 3 | 248 | 9 | 77 | 8 | 96 | 11 | 15 | 4 | 23 | 12 |

**Table 10: Cross-coupled dynamic force coefficients and uncertainty.**

| Operating Condition | | | Cross-Coupled Dynamic Force Coefficient and Uncertainty | | | | | | | |
|---|---|---|---|---|---|---|---|---|---|---|
| Rotor Speed (RPM) | App. Load (kPa) | Flowrate (% Nominal) | $K_{xy}$ (MN/m) | $\pm\delta_{Kxy}$ (MN/m) | $K_{yx}$ (MN/m) | $\pm\delta_{Kyx}$ (MN/m) | $C_{xy}$ (kN-s/m) | $\pm\delta_{Cxy}$ (kN-s/m) | $C_{yx}$ (kN-s/m) | $\pm\delta_{Cyx}$ (kN-s/m) |
| 6000 | 345 | 5 | 10 | 1 | -19 | 6 | -17 | 4 | 0 | 10 |
| 6000 | 345 | 10 | 11 | 1 | -20 | 8 | -17 | 4 | 7 | 9 |
| 6000 | 345 | 25 | 13 | 1 | -26 | 8 | -15 | 4 | 13 | 11 |
| 6000 | 345 | 50 | 15 | 2 | -24 | 10 | -13 | 5 | 17 | 9 |
| 6000 | 345 | 100 | 20 | 1 | -27 | 9 | -9 | 7 | 14 | 10 |
| 6000 | 345 | 150 | 18 | 2 | -26 | 9 | -15 | 6 | 19 | 9 |
| 6000 | 1034 | 10 | 10 | 2 | -29 | 9 | -23 | 5 | 13 | 13 |
| 6000 | 1034 | 15 | 6 | 1 | -33 | 8 | -26 | 5 | 10 | 12 |
| 6000 | 1034 | 25 | 8 | 2 | -31 | 7 | -25 | 5 | 9 | 11 |
| 6000 | 1034 | 50 | 6 | 2 | -31 | 7 | -20 | 4 | 4 | 13 |
| 6000 | 1034 | 100 | 14 | 2 | -31 | 8 | -26 | 5 | 7 | 12 |
| 6000 | 1034 | 150 | 7 | 2 | -34 | 7 | -18 | 5 | 7 | 11 |
| 6000 | 2068 | 5 | -24 | 2 | -52 | 6 | -25 | 5 | -1 | 13 |
| 6000 | 2068 | 25 | -17 | 2 | -44 | 6 | -32 | 5 | -3 | 13 |
| 6000 | 2068 | 50 | -15 | 2 | -45 | 6 | -31 | 3 | -5 | 13 |
| 6000 | 2068 | 100 | -18 | 2 | -49 | 5 | -30 | 3 | -3 | 13 |
| 6000 | 2068 | 150 | -16 | 2 | -47 | 6 | -33 | 3 | -4 | 12 |
| 12000 | 345 | 25 | 18 | 2 | -31 | 7 | -18 | 7 | 6 | 9 |
| 12000 | 345 | 50 | 31 | 4 | -45 | 8 | -11 | 5 | 26 | 14 |
| 12000 | 345 | 100 | 32 | 2 | -46 | 7 | -10 | 6 | 21 | 11 |
| 12000 | 345 | 150 | 35 | 3 | -49 | 7 | -12 | 5 | 21 | 12 |
| 12000 | 1034 | 25 | 17 | 1 | -28 | 6 | -12 | 4 | 15 | 11 |
| 12000 | 1034 | 50 | 3 | 5 | -47 | 6 | -32 | 12 | -1 | 11 |
| 12000 | 1034 | 100 | 10 | 3 | -50 | 5 | -16 | 9 | 2 | 11 |
| 12000 | 1034 | 150 | 18 | 3 | -46 | 5 | -24 | 9 | 1 | 9 |
| 12000 | 2068 | 25 | -7 | 2 | -44 | 6 | -13 | 5 | 8 | 12 |
| 12000 | 2068 | 50 | -13 | 2 | -48 | 6 | -15 | 4 | 7 | 13 |
| 12000 | 2068 | 100 | -23 | 4 | -61 | 12 | -21 | 7 | -11 | 16 |
| 12000 | 2068 | 150 | -17 | 2 | -54 | 6 | -21 | 6 | -13 | 15 |

# APPENDIX C

# OIL ANNULUS TEMPERATURE AND PRESSURE EXAMINATION[9]

The following is an expanded discussion examining the behavior of the bearing housing annulus oil temperature and pressure and its effect on the behavior of the bearing under very low flowrates (<25% of the nominal flow):

The annulus temperature "range" is the difference in temperature between the highest and lowest oil temperatures recorded at a particular operating condition. Figure 53 shows the annulus temperature range, or maximum difference, vs. flow rate for operation at both 6 krpm and 12 krpm. The annulus temperature range increases sharply from <1°C to as much as 26°C as the flow decreases below 25% of the nominal flow for operation at 6 krpm and from <1°C to 5.5°C for operation at 12 krpm. Together with Figures 23 and 24 presenting the behavior of the annulus oil temperatures over selected time spans, the results reveal the oil temperature distribution to become increasingly asymmetrical about the circumference and, with the exception of the D annulus temperature, the annulus temperatures increase in magnitude above the target inlet oil temperature ($T_{in}$ = ~60°C) as the flow decreases below 25% of the nominal flow.

[9] Parts of this section reprinted/adapted with permission from Ref [27]

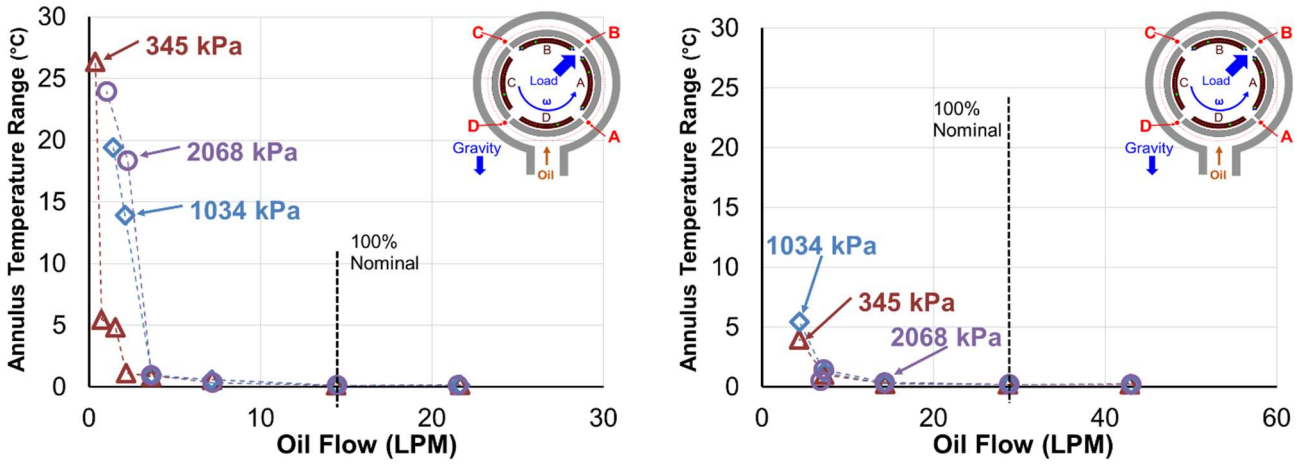


**Figure 53: Annulus temperatures' range or maximum difference vs. supplied flow rate for operation at two shaft surface speeds = 32 and 64 m/s (6 and 12 krpm) and under three specific loads, *W*/(*LD*)= 345 kPa, 1,034 kPa, and 2,068 kPa. Temperature range is the difference between the highest and the lowest measured annulus temperatures. Reprinted/adapted from Ref [27].**

The invariant behavior of the D annulus temperature with decreasing flow rate below ~25% of the nominal flow clearly contrasts to the A, B, and C annulus temperatures whose magnitudes increase above the target inlet oil temperature and also rapidly fluctuate in time over the same flow conditions (<25% of nominal). A plausible explanation of the annulus temperature behavior for flow rates less than 25% of the nominal flow stems from the change in annulus supply *pressure* with flow rate and the relative "groove demand" of the four respective pads' supply grooves on the oil flow patterns within the annulus.

The annulus pressure, measured by a transducer located at the 12 o'clock position in the annulus, decreases monotonically with decreasing flow rate as shown in Figure 54, annulus pressure vs. flow rate for operation at 6 krpm and 12 krpm. The figure also displays "exit chamber pressure", the pressure measured in the annular space containing the oil drains outboard of the bearing housing end seals, on the annulus pressure plot for the same flow rates. The annulus pressure equalizes (or nearly equalizes) with the exit chamber pressure for flows less than 25% of the nominal flow. The large decrease in annulus pressure and the equalization of annulus and exit chamber pressures with decreasing flow rate translates to a lack of a positive pressure gradient

available to force oil from the annulus into the bearing cavity, or more specifically, into the supply grooves between the pads (refer to Figure 6 presenting a photograph of the feed groove).

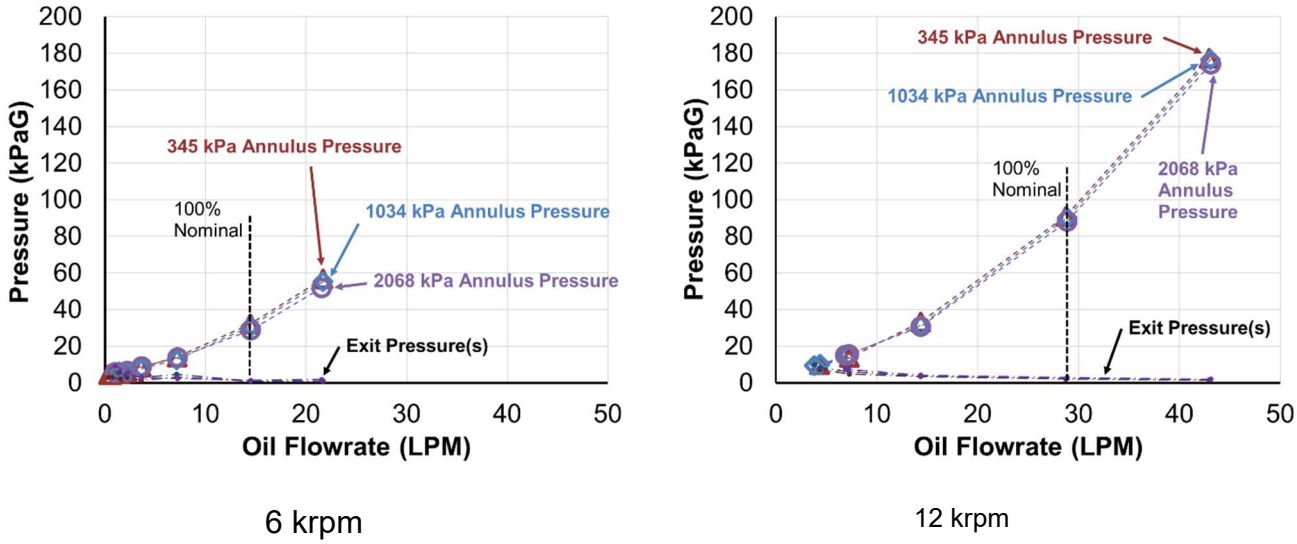


**Figure 54: Annulus pressure vs. supplied flow rate for operation at two shaft surface speeds = 32 and 64 m/s (6 and 12 krpm) and under three specific loads, $W_Y/(LD)$= 345 kPa, 1,034 kPa, and 2,068 kPa. Exit pressure temperature range is the difference between the highest and lowest measured annulus temperatures.**

The groove demand model described by Abdollahi in ref. [18] provides a context to understand the expected relative flow distribution within the supply grooves and in the regions of the annulus local to the grooves. Recall that the "groove demand" is proportional to the quantity of oil drawn from the supply groove as the "make up" flow needed to fill the leading edge of the downstream pad. The grooves, in turn, draw oil from the annulus local to the groove metering orifice. As described in ref. [18], the groove demand model applied to the identical four-pad bearing as used in the present experiment reveals that Pad C should have the highest groove demand, requiring the largest oil flow from the annulus relative to the other pads. Pads B and D follow with the next highest relative demands and are roughly equal to each other. Pad A should have the lowest relative groove demand. For fully flooded operation and a pressurized annulus, oil flows steadily from the annulus into the pad groove where it either combines with the oil carried over from the upstream pad to fill the leading edge of the downstream pad or it exits the groove axially across the bearing end seals. For this flow condition, the annulus thermocouples provide

stable (i.e. non-fluctuating) temperature measurements for steady oil flow over the fully submerged thermocouple junctions suspended in the annulus.

However, the analysis presented in ref. [18] considers the behavior of the bearing with 38 LPM total supply flow. As can be surmised from Figure 54 , for 38 LPM the annulus enjoys a healthy positive gauge pressure in excess of 140 kPa relative to the exit chamber.[10] The positive differential pressure assumption in the model is in stark contrast to the present experiment's measured annulus to exit chamber differential pressure equal to 0 kPa to 3 kPa when operating with flows <25% of the nominal flow. The low annulus differential pressures observed during the present experiment for operation at low flows neutralize the driving pressure forcing oil from the annulus into the pad supply grooves. Without a positive pressure in the annulus to motivate flow, a given pad groove may *demand* a quantity of oil to feed its downstream pad but it may not be able to *draw* the demanded oil from the annulus, resulting in disruption—stagnation, reversal, or lack of submergence—to the oil flow local to the annulus thermocouple.

Consideration of the disrupted (unsteady) flow near the annulus thermocouples under low annulus/exit chamber differential pressure conditions and the difference in groove demand between the A, B, C, and D pads allows evaluation of the asymmetrical and fluctuating annulus temperature results presented in Figures 23 and 24. As oil flow decreases, the residence time of the oil within the annulus increases, allowing the oil more time to absorb heat from the stator and to increase in temperature relative to the more swiftly moving oil encountered for supply flowrates above 2.6 LPM. Fluctuating annulus temperature measurements mark flow slowing to a complete standstill, flow reversing from the orifice block or the complete absence of oil resulting in lack of submergence of the thermocouple and "lapping" of the oil over the thermocouple junction in the areas local to the annulus thermocouples.

With these manifestations of slow or disrupted annular oil flow in mind, consider first the A and D pad pair. Notice both pads reside in the lower quadrants of the test bearing stator and both pads are immediately adjacent to the stator's oil inlet port located at the 6 o'clock position (refer to Figure 7 showing relative placement of pads, annulus thermocouples, and inlet supply port).

[10] The bearing arrangement described in Abdollahi (2017) [18] and in the referenced work by Coghlan (2014) [24] also utilizes ISO VG 46 lubricant, but supplied at a cooler oil supply temperature, 49°C vs. 60°C in the present experiment. As a result of the cooler temperature, the annulus pressure exceeds that shown in Figure 54 for 60°C supply temperature.

Figure 23 reveals an increase in the A annulus temperature compared to the D annulus temperature developing as the flow decreases below 2.6 LPM for the selected operating condition of 6 krpm and 2068 kPa static load. The A annulus temperature also begins to fluctuate while the D annulus temperature remains steady and equal to the inlet oil temperature as the flow decreases below 2.6 LPM.[11] Continuity of mass flow within the system requires the oil delivered to the test stator inlet port to flow into at least one of the pad grooves before flowing through the bearing and returning to the oil system sump via the oil drains in the test bearing apparatus. Recall that the groove demand model states Pad D has a relatively higher groove demand and therefore presents a lower relative resistance to flow entering the groove than Pad A. As evidenced by the stable (i.e. non-fluctuating) temperature equal to the inlet oil temperature as well as the elevated and fluctuating temperature in the A annulus, the oil flow entering the D annulus appears to remain stable and continuous while the oil flow near the A annulus thermocouple slows and becomes disrupted, likely owing to the lower flow resistance presented by the D pad groove as compared to the A pad groove, the low differential pressure between the annulus and the bearing cavity, and the low total supply flow under this condition.

Similar to the A/D pad pair, the B (loaded) and C (unloaded) pad pair also have differing groove demands, with the C pad's demand exceeding the B pad. However, unlike the A/D pads, the B and C pair are located in the upper quadrants of the test bearing stator and are not adjacent to the inlet oil port. The relative location of the B/C pair to the inlet oil port likely affects the annulus temperature behavior relative to the supplied flow rate, at least for flows below ~25% of the nominal flow. Figure 23 shows both the B and C annulus temperatures increase and begin to fluctuate relative to the D annulus temperature (equal to the inlet oil temperature from the oil system). As might be expected based on evaluation of the A/D annulus temperature behavior, the B annulus temperature is higher relative to the C temperature owing to the relatively smaller groove demand and higher flow resistance of the B pad. The higher resistance leads to a slower local flow and a higher temperature compared to the C annulus thermocouple. However, notice that in contrast to the D annulus temperature measurement, the C annulus temperature fluctuates similar to the B (or A) annulus temperature suggesting flow near this thermocouple is also disrupted. The flow removed from the annulus by the D pad groove combined with the elevation

[11] The temperature of the oil in the supply piping immediately before entering the test bearing stator was verified by spot measurement to equal the D annulus temperature throughout the course of testing.

and distance of the C annulus from the inlet port at this very low total supply flow rate likely partially starve the C pad groove of the full quantity of its demanded oil supply resulting in a local flow disruption.

The pad supply groove flow resistances defined by the groove demand model Abdollahi [18] combined with consideration of the low (nil) differential pressure in the annulus provide a likely explanation for the asymmetrical and fluctuating annulus oil temperatures observed for operation with supply flows less than 25% of the nominal flow. However, the explanation must remain speculative as annulus pressure and annulus temperature are the only quantities actually *measured* during the experiment. Experimentally measured local flow into (or out of) the pad groove, measurements of the differential pressure in the individual pad groove vs. the annulus, and/or a direct observation of the fluid fill condition within the annulus (as by a transparent bearing stator) could serve to confirm the flow disruption near the thermocouples under low flow conditions. Experiments performing such quantified measurements are candidates for future study as they could potentially offer data useful for the increasing the fidelity of predictive tools estimating oil film temperature and its effect on the prediction of bearing performance under low oil flow conditions.

Although the results presented in Figures 23, 24, and 53 clearly show the development of asymmetrical and fluctuating oil temperatures in the supply anulus for operation with flow rates less than 25% of the nominal flow, the non-uniform annulus conditions evidently do not affect pad surface temperatures under the same operating conditions. Figures 55 and 56 present the temperature range, or maximum temperature difference, between each of the loaded pads (A and B) and each of the unloaded pads (C and D) for operation at both 6 krpm and 12 krpm. The figures also present the range of the A/B pair and the C/D pair of annulus temperatures for comparison to the maximum pad temperature ranges. Note that the annulus thermocouple measures the oil local to the pad supply groove of the same label. For example, the “A” annulus thermocouple measures the oil local to the orifice that is available to flow into the “A” pad groove inside of the bearing cavity.

For operation at 6 krpm (Figure 55), the difference in maximum pad temperatures between either the loaded pad pair or the unloaded pair is less than 2°C for operation with flow rates less than 25% of the nominal flow. In contrast, the ranges of the annulus temperature measurements

for the A and B locations increase dramatically to as much as 26°C as flow rate decreases for the same operating conditions. Similarly, the C and D annulus temperature range increases to nearly 20°C as flow rate decreases. The lack of a clear correlation between loaded or unloaded pad temperature variations and the annulus temperature ranges shows that the temperature of the oil in the annulus is not driving a variation in pad surface temperature. This result is not unexpected as the suspected flow disruption in the annulus near the groove feed orifices suggest that little flow enters the groove from the annulus, regardless of the local temperature. Note that a similar comparison for operation at 12 krpm shaft speed cannot be made as few testing points are available for flow rates less than 25% of the nominal flow.

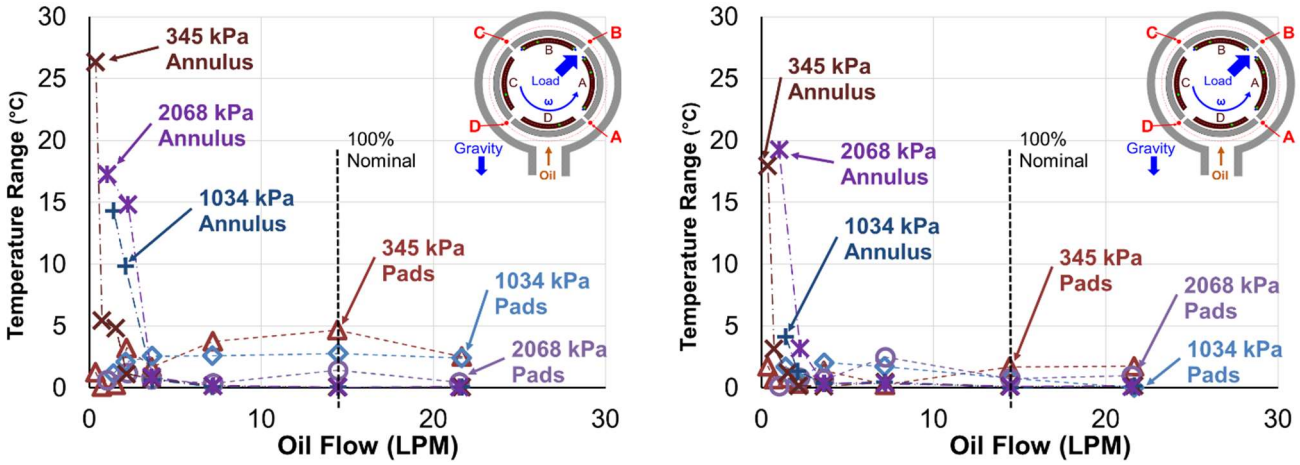


(a) A and B pad and annulus

(b) C and D pad and annulus

**Figure 55: Loaded pad A and B (left) and unloaded pad C and D (right) temperatures' range or maximum difference vs. supplied flow rate for operation at shaft surface speed = 32 m/s (6 krpm) and under three specific loads, $W_Y/(LD)$= 345 kPa, 1,034 kPa, and 2,068 kPa, compared with the pads' inlet annulus temperatures, respectively. Temperature range is the difference between the highest and the lowest measured temperatures on pad A and B or C and D or their local annulus temperatures, respectively.**

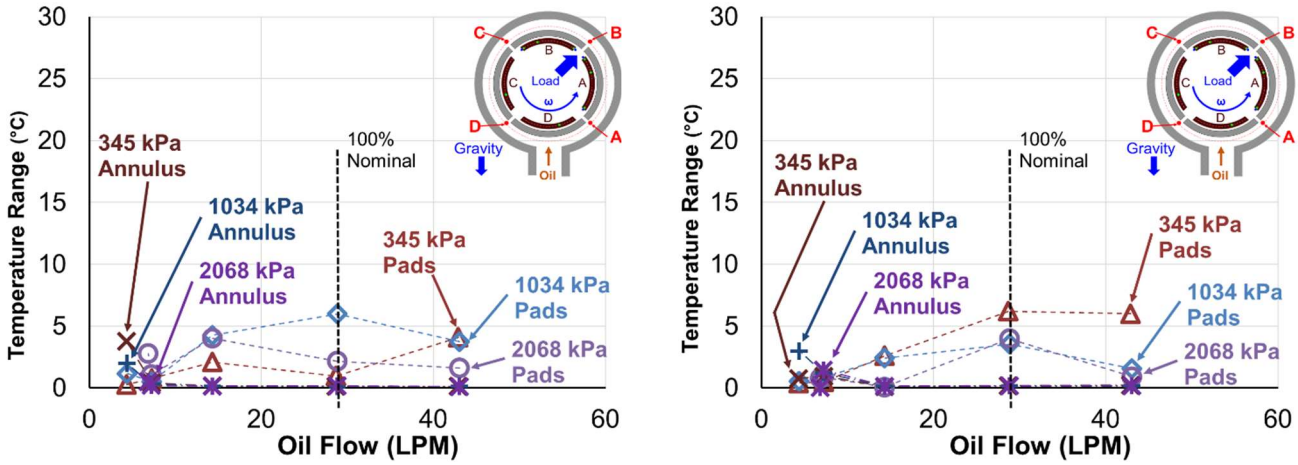


**Figure 56: Loaded pad A and B (left) and unloaded pad C and D (right) temperatures' range or maximum difference vs. supplied flow rate for operation at shaft surface speed = 64 m/s (12 krpm) and under three specific loads, $W_Y/(LD)$= 345 kPa, 1,034 kPa, and 2,068 kPa, compared with the pads' inlet annulus temperatures, respectively. Temperature range is the difference between the highest and the lowest measured temperatures on pad A and B or C and D or their local annulus temperatures, respectively.**

Thermocouples mounted to the upstream face of each of the loaded pads permit measurement of the oil temperature entering the leading edge of the pad surfaces (see Figure 8) showing the "unwrapped" pad and thermocouple layout). Figure 57 displays the ranges of these leading-edge temperatures for operation at 6 krpm and 12 krpm overlaid with the annulus temperature ranges recorded at the same supply flow rates. For operation at 6 krpm, the leading edge temperature range results bear a similar lack of correlation to the annulus temperature ranges as the maximum pad temperature range/annulus temperature range comparison presented in Figures 55 and 56.

Together with the pad surface and annulus temperature difference results, the lack of clear correlation between the leading-edge temperature ranges and the annulus temperature ranges show the temperature of the oil in the supply annulus has little effect on the pad surface temperatures and oil temperatures inside the bearing cavity for operation with flowrates less than 25% of the nominal flow. Recalling the decrease in annulus pressure shown in Figure 54, the pressure in the annulus is clearly insufficient to drive a significant "make up" oil flow into the cavity. The pad and leading-edge oil temperatures are instead dominated by the operating condition (shaft speed and applied load) and the temperature of the oil recirculating within the bearing cavity.

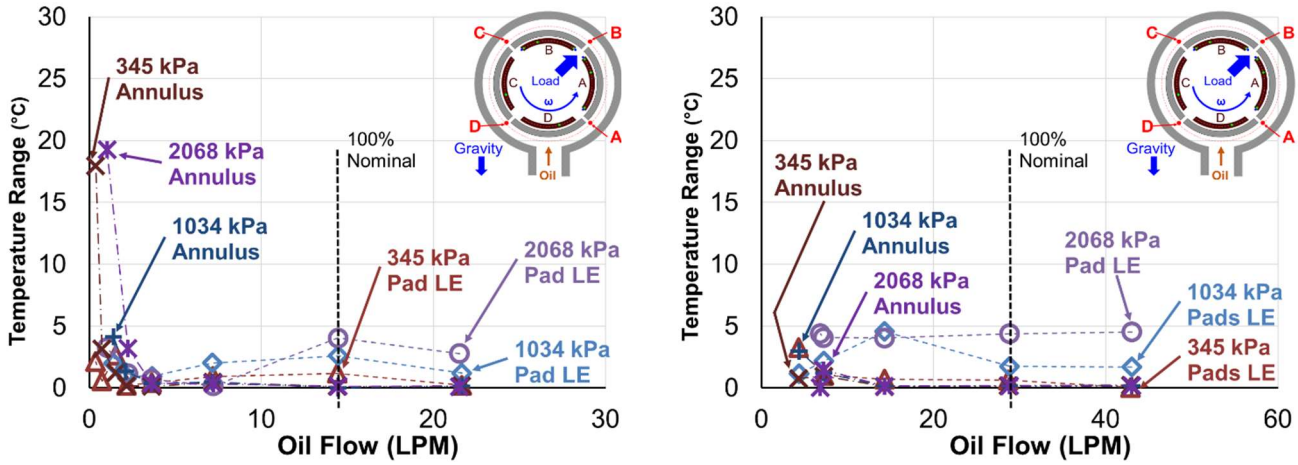


**(a) 6 krpm** **(b) 12 krpm**

**Figure 57: Leading edge temperatures' range or maximum difference vs. supplied flow rate for operation at shaft surface speed = 32 m/s (6 krpm) left, and 64 m/s (12 krpm) right and under three specific loads, $W_Y/(LD)$= 345 kPa, 1,034 kPa, and 2,068 kPa, compared with the pads' inlet annulus temperatures, respectively. Temperature range is the difference between the highest and the lowest measured temperatures on leading edge of pad A and B or their local annulus temperatures, respectively.**